SURFACE AND MICROSTRUCTURAL PROPERTIES OF PHOTOCATALYTIC CEMENTS FOR PAVEMENT APPLICATIONS

by

Daniel King
Jeffery Roesler

University of Illinois at Urbana-Champaign

for

Center for Highway Pavement Preservation
(CHPP)

In cooperation with US Department of Transportation-Research and Innovative Technology Administration (RITA)

October, 2016

Disclaimer

The contents of this report reflect the views of the authors, who are responsible for the facts and the accuracy of the information presented herein. This document is disseminated under the sponsorship of the U.S. Department of Transportation's University Transportation Centers Program, in the interest of information exchange. The Center for Highway Pavement Preservation (CHPP), the U.S. Government and matching sponsor assume no liability for the contents or use thereof.

Technical Report Documentation Page			
1. Report No. ICT-16-024	2. Government Accession No.	3. Recipient's Catalog No.	
4. Title and Subtitle SURFACE AND MICROSTRUCTURAL PROPERTIES OF PHOTOCATALYTIC CEMENTS FOR PAVEMENT APPLICATIONS		5. Report Date 6. Performing Organization Code	
7. Author(s) Daniel King, Jeffrey Roesler		8. Performing Organization Report No. UILU-ENG-2016-2024	
9. Performing Organization Name and Address CHPP Center for Highway Pavement Preservation, Tier 1 University Transportation Center Michigan State University, 2857 Jolly Road, Okemos, MI 48864		10. Work Unit No. (TRAIS) 11. Contract or Grant No.	
12. Sponsoring Organization Name and Address United States of America Department of Transportation Research and Innovative Technology Administration		13. Type of Report and Period Covered 14. Sponsoring Agency Code	
15. Supplementary Notes Report uploaded at http://www.chpp.egr.msu.edu/			
16. Abstract Thin concrete inlays incorporating flowable fibrous concrete (FFC) mix designs as well as titanium dioxide (TiO_2)-containing photocatalytic cements are a promising pavement preservation solution. These multi-functional inlays offer enhanced constructability and structural properties while also benefiting the environment by reacting with harmful nitrogen oxides (NO_x) and removing them from the near-road environment. Photocatalytic FFC mixes were prepared in the laboratory to verify feasibility of field application and to characterize how mixture and microstructural properties and environmental factors affect photocatalytic performance. Testing of fresh and hardened concrete confirmed the ease of application of photocatalytic FFC and its benefits to the pavement's structural properties, particularly to residual strength ratio and fracture toughness. Laboratory photoreactor testing of mortar samples established that photocatalytic FFC is an effective tool to mitigate NO_x pollution in the urban environment. Carbonation of the sample surface was shown to have the potential to significantly reduce NO_x removal ability, but this effect could be curtailed by replacing some of the cement with fly ash or increasing TiO_2 content by mass of cement. Spectrophotometer testing showed that reflectance of the mortar samples also factored into photocatalytic performance. More reflective specimens demonstrated greater NO_x removal ability, which was most apparent when comparing the performance of white cement specimens to gray cement specimens. Finally, analysis of cement paste specimens using scanning electron microscopy (SEM) and related techniques suggested the importance of porosity to photocatalytic ability. These findings will be useful in helping design and optimize photocatalytic concrete mix designs for applications in pavements and other structures. Based on the results of the mixes and materials tested, a white cement photocatalytic concrete with 15% fly ash replacement would offer the most optimal balance between high photocatalytic efficiency and resilience to carbonation.			
17. Key Words Photocatalytic Concrete, Titanium Dioxide, Albedo, Concrete Overlays		18. Distribution Statement No restrictions.	
19. Security Classification (of this report) Unclassified.	20. Security Classification (of this page) Unclassified.	21. No. of Pages 86 +Appendices	22. Price NA

Table of Contents

List of Figures

List of Tables

List of Abbreviations

AEA	Air entraining admixture
ASCE	American Society of Civil Engineers
BEI	Backscatter electron imaging
CH	Calcium hydroxide
CHPP	Center for Highway Pavement Preservation
COV	Coefficient of variation
DOT	Department of Transportation
EDS	Energy-dispersive x-ray spectroscopy
US EPA	United States Environmental Protection Agency
FFC	Flowable fibrous concrete
FRC	Fiber reinforced concrete
FTIR	Fourier Transform Infrared Spectroscopy
HPC	High performance concrete
HRWR	High range water reducer
LCA	Life Cycle Analysis
MIP	Mercury intrusion porosimetry
PCC	Portland cement concrete
PEF	Photocatalytic Efficiency Factor
RILEM Structures)	The International Union of Testing and Research Laboratories for Materials and
RH	Relative humidity
SCC	Self-compacting concrete
SCM	Supplementary cementitious materials
SEI	Secondary electron imaging
SEM	Scanning electron microscopy
SiC	Silicon carbide
XRF	X-ray fluorescence
UV	Ultraviolet
VOC	Volatile Organic Compound

Acknowledgments

Thanks to the University Transportation Center for Highway Pavement Preservation for funding of this project. Special thanks to Essroc Cement and Cristal for donating materials used in this study. This research was carried out in part at the Frederick Seitz Materials Research Lab Central Facilities, University of Illinois.

Executive Summary

Thin concrete inlays incorporating flowable fibrous concrete (FFC) mix designs as well as titanium dioxide (TiO_2)-containing photocatalytic cements are a promising pavement preservation solution. These multi-functional inlays offer enhanced constructability and structural properties while also benefiting the environment by reacting with harmful nitrogen oxides (NOx) and removing them from the near-road environment. Photocatalytic FFC mixes were prepared in the laboratory to verify feasibility of field application and to characterize how mixture and microstructural properties and environmental factors affect photocatalytic performance. Testing of fresh and hardened concrete confirmed the ease of application of photocatalytic FFC and its benefits to the pavement's structural properties, particularly to residual strength ratio and fracture toughness. Laboratory photoreactor testing of mortar samples established that photocatalytic FFC is an effective tool to mitigate NOx pollution in the urban environment. Carbonation of the sample surface was shown to have the potential to significantly reduce NOx removal ability, but this effect could be curtailed by replacing some of the cement with fly ash or increasing TiO_2 content by mass of cement. Spectrophotometer testing showed that reflectance of the mortar samples also factored into photocatalytic performance. More reflective specimens demonstrated greater NOx removal ability, which was most apparent when comparing the performance of white cement specimens to gray cement specimens. Finally, analysis of cement paste specimens using scanning electron microscopy (SEM) and related techniques suggested the importance of porosity to photocatalytic ability. These findings will be useful in helping design and optimize photocatalytic concrete mix designs for applications in pavements and other structures. Based on the results of the mixes and materials tested, a white cement photocatalytic concrete with 15% fly ash replacement would offer the most optimal balance between high photocatalytic efficiency and resilience to carbonation.

CHAPTER 1-INTRODUCTION

1.1. BACKGROUND

Environmental concerns and sustainability goals have received increasing recognition and attention from the construction industry in recent years. Topics such as life cycle assessment and global warming potential are more regularly discussed and possibly considered for new construction projects. The transportation infrastructure, including pavements, is no exception to this trend in civil engineering construction. Researchers and practitioners have begun to explore a number of sustainability-based initiatives related to pavement design and construction, including incorporating recycled materials, adopting less energy-intensive construction practices, and considering the effects of paved surfaces on their surrounding environments.

At the same time, transportation agencies are increasingly stressed by funding cuts and mandates to do more with fewer resources to maintain the condition of their pavement networks. Under these pressures, pavement preservation has emerged as a strategy to enhance pavement surface life while reducing long-term costs. A pavement preservation system attempts to address deterioration at an early stage with preventative measures and small repairs to delay larger-scale maintenance and rehabilitation and reduce the life-cycle costs.

With these growing concerns, there is great interest in pavement solutions incorporating both sustainability and pavement preservation. To date, these concepts have predominantly been incorporated into asphalt cement products (Peshkin *et al.* 2011). However, recent advancements in concrete technology have led to the development of newer concrete preservation and sustainability options. In particular, the development of flowable fibrous concrete (FFC) mixes and photocatalytic concrete technologies offer the possibility of constructing thin, multi-functional concrete inlays with FFC as a viable option that can meet both preservation and sustainability needs.

FFC mixes combine the rapid constructability of self-compacting concrete (SCC) with a high volume of synthetic macro-fiber reinforcement. Bordelon and Roesler (2011) constructed a full-scale concrete overlay test section using an FFC mix, verifying its constructability for thin overlay and inlay applications and evaluating factors such as bonding to the underlying asphalt, panel size, and joint cracking. The FFC mix also demonstrated improved fracture toughness and residual strength relative to a typical Portland cement concrete (PCC) pavement mixture. Thin, quickly- and easily-constructed, and possessing superior strength and fracture properties, FFC inlays are a very capable pavement preservation option.

Meanwhile, thin FFC inlays can also produce significant environmental benefits by incorporating photocatalytic concrete technologies and urban heat island mitigation if applied correctly. By itself, Sen *et al.* (2015) showed that the increased surface albedo of FFC inlays is capable of lowering surface temperatures to reduce heat island effects and global warming potential in urban areas. Further benefits can be achieved by incorporating titanium dioxide (TiO_2) nanoparticles into the cementitious matrix to make photocatalytic concrete. Activated by UV-A radiation from sunlight, TiO_2 nanoparticles can react with airborne pollutants, most notably nitrogen oxides (NOx), and remove them from the air (Devahasdin *et al.* 2003, Ballari *et al.* 2010).

NOx, which consists of NO and NO_2, is one of the most prevalent air pollutants in urban areas and in particular the near-road environment, where it is primarily a result of vehicular emissions. Area-wide background NOx concentrations have long been regulated by agencies because of contribution to environmental hazards such as smog. More recently, the US EPA has mandated monitoring peak NO_2 emissions near roadways because of its harmful impacts on human health in populations concentrated in the near-road environment (Environmental Protection Agency 2010). One method through which these NOx emissions can be tackled is through constructing photocatalytic concrete pavements. By incorporating TiO_2 nanoparticles into the pavement structure, it may be possible to improve air quality by attacking the problem directly at the main source of NOx emissions. By combining the concept of photocatalytic pavements with FFC mixes, there exists a concrete pavement solution for both sustainability and preservation purposes.

1.2. OBJECTIVES

The primary objectives of this study were to verify the feasibility of incorporating photocatalytic cements into thin FFC inlays for pavement preservation and to investigate the surface and microstructural properties that affect photocatalytic performance. By characterizing the properties of photocatalytic cements and environmental factors that had the greatest impact on NOx removal ability, optimal mix designs and application methods could be identified to determine where thin, photocatalytic FFC inlays could be implemented with the most success.

In Chapter 2, FFC mix designs incorporating photocatalytic cement were designed and cast in the laboratory. Testing was performed to determine fresh properties as well as hardened strength and fracture properties of photocatalytic FFC. Tests on fresh concrete included slump flow, air content, and unit weight. Tests on cast specimens included compressive and split tensile strength, ASTM C1609 for flexural and post-crack residual strength, and finally an adaptation from a RILEM draft standard (Shah 1990) to measure fracture properties. The results of these tests were compared to those of a typical FFC mix design to verify that, when adding TiO_2 nanoparticles, FFC mixes maintained enhanced constructability and structural properties needed for application in thin inlays.

In Chapter 3, photocatalytic mortar specimens based on FFC mix designs were prepared for laboratory photoreactor testing to characterize their NOx removal ability. Parameters including the cement type (white vs. gray, commercially-blended TiO_2 cement vs. anatase TiO_2 added directly to the mix), TiO_2 addition rate, reflectance, and addition of supplementary cementitious materials were varied from mix-to-mix to study how they affected photocatalytic performance. Additionally, specimens were artificially carbonated and tested by a spectrophotometer to measure changes caused by carbonation and reflectance, respectively, on overall NOx removal ability as well as the impact of individual variables. The results of this laboratory testing were used to optimize an FFC mix design for NOx removal while taking the impact of environmental carbonation into consideration.

Finally, in Chapter 4, the microstructural properties of photocatalytic cementitious materials were analyzed to investigate the ways in which the microstructure impacts photocatalytic performance. Polished cement paste specimens were analyzed using scanning electron microscopy (SEM) to characterize microstructural morphology, TiO_2 content and dispersion, and porosity. The results were studied to try to achieve a better understanding of the mechanisms and properties of photocatalytic cement paste and the factors that affect photocatalytic performance.

CHAPTER 2-FRESH AND MECHANICAL PROPERTIES OF PHOTOCATALYTIC CONCRETE

2.1. INTRODUCTION

With increasing interest in the use of photocatalytic cementitious materials, focus and attention has been directed on finding useful applications. While there is a global desire to improve air quality in urban areas and the near-road environment, there are many possibilities for addressing this goal with TiO_2-containing cement. In the near-road environment alone, options include façade and surface coatings for roadside structures or to incorporate TiO_2 into the concrete mixture itself for use in medians, barrier walls, or pavements.

One potential pavement application for photocatalytic concrete would be for concrete inlays for preservation purposes. The concepts of these thin inlays are to construct them with a flowable fibrous concrete (FFC) mix that combines the workability and constructability of self-consolidating concrete (SCC) with fiber reinforcement for enhanced structural performance and cracking resistance. The ease of construction of the inlays makes them particularly fitting for more urban settings, where photocatalytic pavements may prove most useful in combating air pollution. In addition, the required thickness of the thin inlays would provide a cost-effective means to incorporate the TiO_2 nanoparticles in the full thickness instead as a coating, which requires a very durable photocatalytic surface treatment.

To ensure its suitability for thin inlay applications, it is necessary to characterize the effect of TiO_2 nanoparticles on the fresh and mechanical properties of concrete. In this experiment, a FFC mix design incorporating photocatalytic cement was design, mixed, and cast in the laboratory. Testing was performed on the fresh and hardened concrete, and the performance of the photocatalytic mix was compared to that of a standard FFC mix to verify that the TiO_2-containing mixture retained its ease of construction and structural properties, which are crucial to its potential use in concrete inlays.

2.2. LITERATURE REVIEW

2.2.1. Fresh and Mechanical Properties of Concrete Containing TiO_2 Nanoparticles

There is a substantial amount of literature available regarding photocatalytic and self-cleaning properties of TiO_2-containing cementitious mixtures, primarily mortar and paste, which will be explored in later chapters. Perhaps because of the high cost and availability of the cement, TiO_2-containing concrete mixtures have not been thoroughly investigated. In particular, the fresh and mechanical properties of photocatalytic concrete are not always well-defined in the literature, which are very important for thin inlay applications.

2.2.1.1. Fresh Properties

Three of the major fresh properties of photocatalytic concrete that have been studied are workability, setting time, and air entrainment. In most cases, there has been good agreement among researchers on the impact of TiO_2 nanoparticles on concrete properties, but in some instances, available data is limited.

With respect to workability, TiO_2 nanoparticles have been demonstrated to result in a decrease in the workability of fresh concrete. Nazari and Riahi (2011) observed roughly a linear decrease in

slump for a mix at a constant w/c from around 8 cm (3.25 inches) with no TiO_2 down to about 2.25 cm (just under 1 inch) at 2% TiO_2 by weight. Diamanti *et al.* (2013) also measured a decrease in slump upon adding TiO_2 nanoparticles, finding a linear decrease of about 10 cm (4 inches) when going from a mix with no TiO_2 to 5% TiO_2 by weight. Using a commercial photocatalytic cement with unknown TiO_2 content, Panesar and Dolatabadi (2014) showed an approximate 25% decrease in slump compared to a control mixture.

Decreased workability could be a concern when determining the constructability of a flowable inlay mixture. However, Cassar *et al.* (2003) was able to develop a photocatalytic high performance concrete (HPC) mix design featuring TiO_2-containing cement. Using HPC mixture principles, including the use of a superplasticizer, the mix achieved good flowability for fabrication of high-arching, sail-shaped structural elements in a church. The findings suggest that, despite possible losses in workability, photocatalytic cements can be compatible with self-consolidating mixes.

The addition of TiO_2 nanoparticles has been shown to increase the rate of cement hydration, leading to faster set times. A study by Lee and Kurtis (2010) showed using isothermal calorimetry that the presence of TiO_2 nanoparticles (at an addition rate of 5-15%) led to an increase in the rate of C_3S hydration, with the rate of reaction increasing with greater TiO_2 content. The likely mechanism of the increase in C_3S hydration was that the surface of the nanoparticles affords additional nucleation sites for cement grains, a behavior that has also been proposed by Chen *et al.* (2011) for photocatalytic cementitious mixtures.

An increase in the C_3S reaction rate can lead to a higher degree of early-age hydration of Portland cement, allowing for faster set times. Lackhoff *et al.* (2003) and Nazari and Riahi (2011) have observed faster set times in paste and fresh concrete mixtures with TiO_2, respectively. Relative to a control mixture, Nazari and Riahi (2011) determined that adding 2% TiO_2 by weight decreased time of initial set for concrete from around 200 minutes to under 100 minutes and the time of final set from roughly 300 to 175 minutes using a Vicat needle. Thus, even at lower TiO_2 contents, the nanoparticles can significantly affect setting time.

The effect of TiO_2 nanoparticles on air entrainment, if any, has not been thoroughly studied. Research by Panesar and Dolatabadi (2014) showed that, using the same amount of air entraining admixture (AEA) for mixes containing a general-use cement and a commercial photocatalytic cement, the measured air content was about 2.5% lower (4% vs. 1.5%) for the photocatalytic mixture.

2.2.1.2. Mechanical Properties

Compressive strength is the mechanical property of photocatalytic cementitious materials that has been most thoroughly analyzed, but no there is no clear consensus on the effect of adding TiO_2 nanoparticles to a paste, mortar, or concrete mixture. Comparing strength testing results in the literature is complicated by the fact that, in some cases, mixtures are created where the TiO_2 nanoparticles replace the cement at a certain weight percentage and are considered part of the cementitious materials (w/cm), while in other studies the nanoparticles are added in addition to the cement and not considered in w/cm. Concrete specimens and structures are more likely to use a commercially-blended cement product in which nanoparticles effectively replace cement particles, so it is most appropriate to consider the TiO_2 as part of the cementitious material content when considering the use of photocatalytic concrete for pavement applications.

Lee (2012) found when testing cement paste with up to 10% TiO_2 replacement that compressive strength increased at lower w/c ratios (0.4), while at higher w/c ratios (0.5-0.6) compressive strength was effectively the same. Lackhoff *et al.* (2003) also found an increase in the compressive strength of cement paste with the addition of up to 10% TiO_2 without replacement of cement.

For concrete samples, results have been mixed. Nazari *et al.* (2010) found that TiO_2 replacements up to 2% led to slight increases in compressive strength. Diamanti *et al.* (2013), however, observed a slight decrease in the compressive strength of concrete with the addition of up to 10% TiO_2 without replacement of cement. Panesar and Dolatabadi (2014) also demonstrated a decrease in compressive strength in concrete mixed with a commercial photocatalytic cement, attributing the decrease primarily to the replacement of Portland cement with TiO_2 in the cementitious matrix.

Beyond compressive strength, Cassar *et al.* (2003) determined indirect tensile and flexural strengths for the photocatalytic HPC mixture and found them adequate for the application, though they were not compared to a control mix. With respect to durability, Panesar and Dolatabadi (2014) found that, at 5-7% hardened air content, photocatalytic concrete offers comparable freeze-thaw resistance to a typical general use concrete mix (keeping in mind that they did encounter some trouble entraining air in a photocatalytic mixture). Finally, changes in fracture properties (e.g. fracture toughness, fracture energy) have not been quantified for TiO_2-containing concrete.

2.2.2. Flowable Fibrous Concrete

Flowable fibrous concrete (FFC) technologies have been developed for use in preservation and minor rehabilitation of pavements. Preservation is a strategy to enhance pavement service life by addressing deterioration at an early stage to avoid more extensive and expensive maintenance and rehabilitation. To date, asphalt cement products have been the predominant material used for pavement preservation (Peshkin *et al.* 2011). Flowable fibrous concrete offers a Portland cement concrete solution for preservation through the construction of thin concrete inlays at thicknesses between 50 to 100 mm (2-4 inches).

FFC mixes combine principles of self-consolidating concrete (SCC) and fiber reinforced concrete (FRC). Through the use of smaller aggregates and admixtures such as superplasticizers, SCC mixes flow easily into place and minimize the amount of work required for compaction and consolidation. A workable SCC mix can allow for rapid, easy construction of a concrete inlay where site access and the thinness of the section might pose constructability issues. Meanwhile, FRC mixes provide enhanced cracking resistance and post-crack residual strength, particularly beneficial for thin concrete sections (Zhang and Li 2002).

An FFC mix design for thin concrete inlays was developed by Bordelon and Roesler (2011). A full-scale test section with a thickness of 50 mm (2 inches) was successfully constructed on an existing asphalt pavement to verify the constructability of FFC inlays. Factors such as bonding to the underlying asphalt, panel size, and joint cracking were studied to determine optimal design features. Laboratory testing was performed on beam and cylindrical specimens to characterize mechanical strengths and confirm the enhanced fracture properties and residual strength offered by the FFC mix.

2.3. EXPERIMENTAL PROCEDURES

To evaluate the suitability of photocatalytic concrete for thin inlay applications, a FFC mix containing photocatalytic cement was developed based on a previously-established FFC inlay mix design. The mixture was cast in the laboratory and tested for fresh properties, including workability and air entrainment, which were of particular concern for the potential inlay application. Specimens were cast and tested at 7 and 28 days to measure mechanical properties, including compressive and splitting tensile strengths, flexural properties, and fracture properties. The results were analyzed to quantify any differences resulting from the use of cement containing TiO_2 nanoparticles and to verify suitable constructability and performance of the mix for use with thin concrete inlays. The procedures used for this testing are outlined in the subsections below.

2.3.1. Mix Designs

FFC mixes featuring a high range water reducer (HRWR) and synthetic macro-fiber reinforcement were prepared based on the mix design developed by Bordelon and Roesler (2011). A mix containing conventional gray Type I Portland cement (Plain FFC) served as a control, and photocatalytic FFC mixes were prepared by substituting a commercial photocatalytic cement, in which TiO_2 (at an unknown addition rate) was pre-blended with Type I Portland cement. Mixtures were prepared with both white and gray versions of the photocatalytic cement (labeled White TiO_2 and Gray TiO_2). Except for cement type, the mixtures were identical, and the conventional and photocatalytic cements were both manufactured at the same facility.

The mix designs are listed in Table 2.1. The mix proportions are roughly the same as those used by Bordelon and Roesler (2011), with some adjustments to the HRWR dosage, which was increased from 1100 ml/m^3 to between 1700 and 2000 ml/m^3 to achieve the desired workability. The sources of the materials and admixtures were the same as those previously, except for Type C fly ash, which came from a different supplier. Synthetic macro-fibers were used for the fiber reinforcement. Overall the proportions correspond to a 30% fly ash replacement rate and a 0.40 w/cm. The synthetic macro-fiber dosage corresponds to 0.5% by volume.

Table 2-1 Plain and photocatalytic FFC mix designs

Mix Component	Unit	Proportion
Sand	kg/m^3	857
Limestone Chip, 9.5 mm Nominal Max Aggregate Size	kg/m^3	1052
Conventional Type I/TiO_2-containing Type I Cement	kg/m^3	328
Type C Fly Ash	kg/m^3	140
Water	kg/m^3	187
High Range Water Reducer	ml/m^3	1700-2000
Air-Entraining Admixture	ml/m^3	107
Synthetic Macro-fibers	kg/m^3	4.6

2.3.2. Mixing and Casting

Mixing of the photocatalytic FFC was performed in the laboratory using a paddle mixer. As previously mentioned, HRWR dosage was varied somewhat from mix to mix to obtain sufficient workability and flowability. Beam and cylindrical specimens were cast following ASTM C192 (2015) for strength and fracture testing. The fracture beam specimens were not rodded for consolidation, only hit with the mallet as each of the three lifts were placed. All specimens were moist cured until they reached testing age.

2.3.3. Fresh Property Tests

Before specimen casting, a slump flow test to characterize workability, an air content test, and a unit weight measurement were completed. The slump flow test was performed by placing a standard slump cone upside-down on a flat surface, filling the cone to the top without any consolidation, and slowly raising the slump cone, allowing the concrete to flow out. After fully removing the slump cone, the diameter of the concrete that flowed onto the flat surface was measured. The air content test was performed with a Type B air meter according to ASTM C231 (2014) along with the unit weight.

2.3.4. Mechanical Property Tests

Mechanical testing on each mix was performed at 7 and 28 days (only enough White TiO_2 specimens were cast for 7 day testing because of material availability). Cylindrical specimens measuring 100 mm x 200 mm were tested for compressive and split tensile strength according to ASTM C39 (2005) and ASTM C496 (2011), respectively. Flexure beam specimens measuring 450 mm x 150 mm x 150 mm were tested following ASTM C1609 (2013). The flexural test setup is pictured in Figure 2.1. A continuous load-deflection plot was recorded with the test concluded when the net axial deflection (δ) reached 1/150 of the span length (L). The peak load (P_1) was used to calculate flexural strength, also known as modulus of rupture (MOR), and the load at L/150 was recorded to characterize the residual strength (f_{150}) and residual strength ratio (R_{150}) according to ASTM C1609.

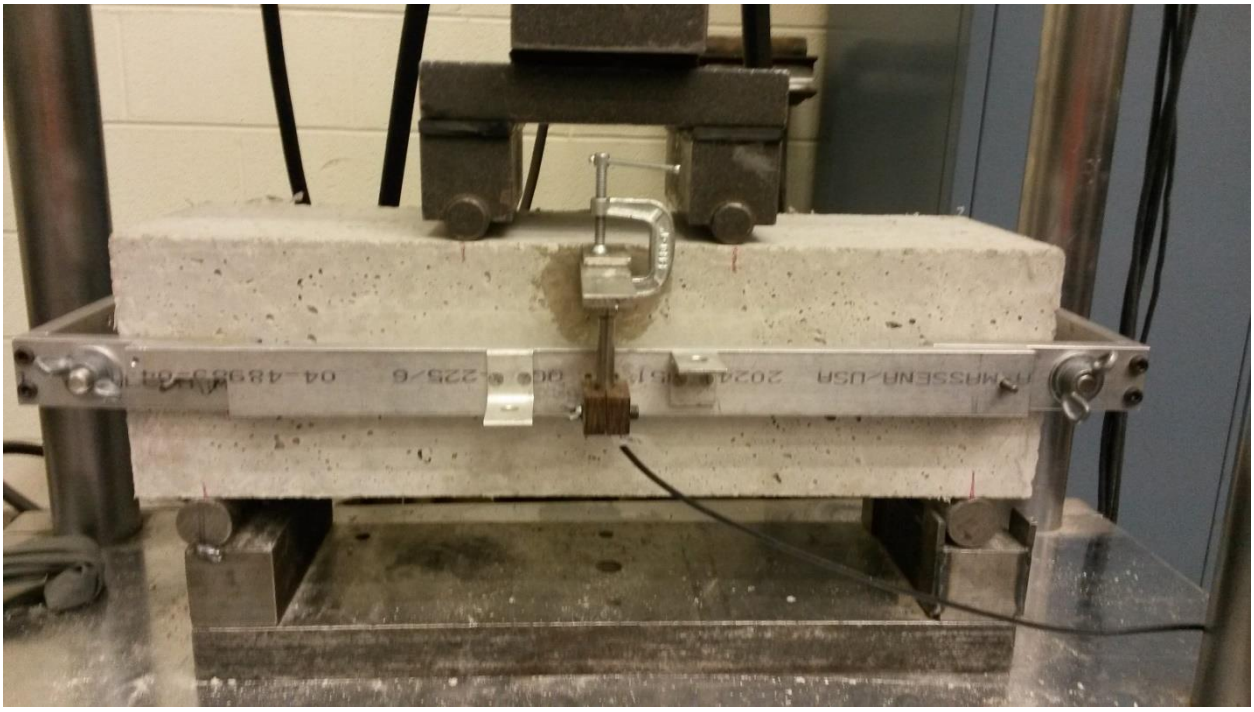

Figure 2-1 ASTM C1609 testing for flexural properties of fiber reinforced concrete

Finally, 700 mm x 150 mm x 80 mm single edge notched beams were tested to determine fracture properties. The fracture beams were tested in three-point bending based on a RILEM draft standard (Shah 1990). The fracture test setup is pictured in Figure 2.2. After loading to peak load and then unloading, the beams were re-loaded and allowed to proceed to failure. The properties that were used to characterize the fracture properties of the specimens included critical stress intensity factor (K_{Ic}), critical crack tip opening displacement ($CTOD_c$), initial fracture energy (G_{Ic}) and total fracture energy (G_F), which were each calculated from the load-deflection data according to the draft standard.

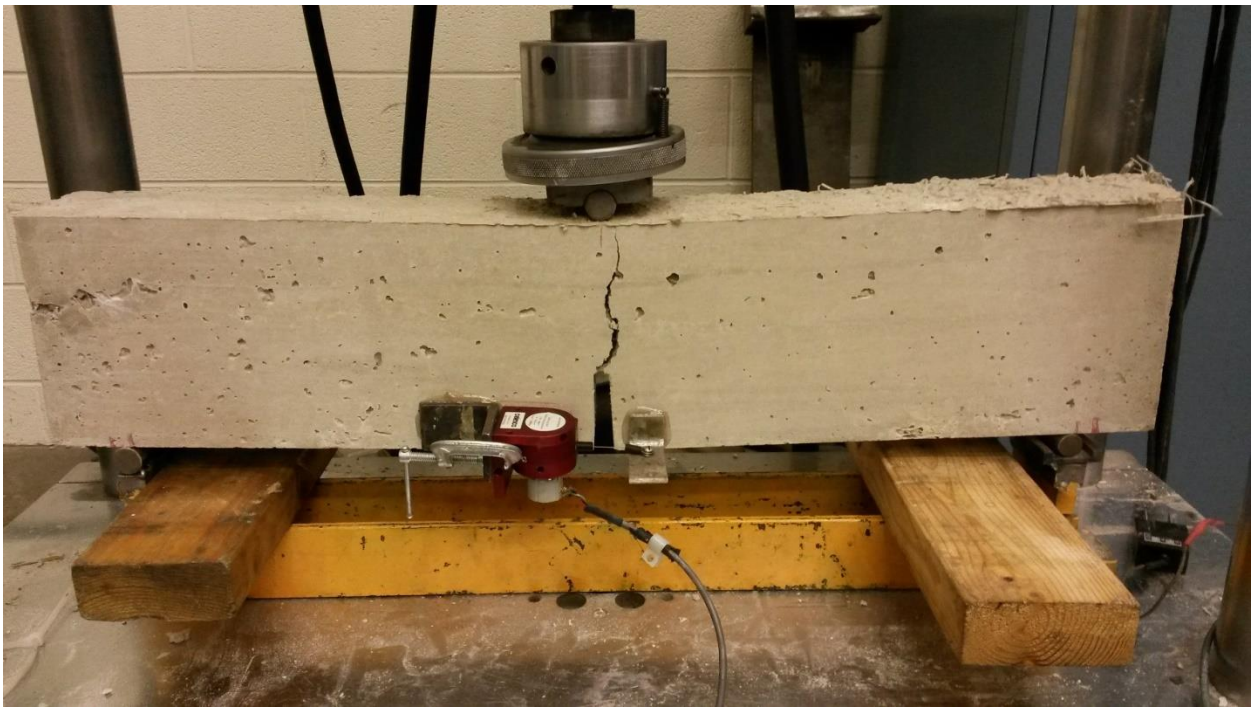

Figure 2-2 Fracture testing of a single edge notched beam specimen

2.4. RESULTS

2.4.1. Fresh Properties

Results from testing of fresh properties are listed in Table 2.2. All data are averages taken from each laboratory mix. An additional column is added to Table 2.2 to compare the results to those found by Bordelon and Roesler (2011).

Table 2-2 Fresh properties of FFC mixes

Fresh Properties				
	Plain FFC	White TiO_2	Gray TiO_2	Plain FFC (Bordelon 2011)
Slump Flow Diameter (mm)	580	415	400	394
Air Content (%)	6.7	8.8	7.5	6.8
Unit Weight (kg/m^3)	2311	2263	2218	2236

2.4.2. Mechanical Properties

Results of all mechanical testing are summarized in Table 2.3. Columns are also included in Table 2.3 to compare results to those found by Bordelon (2011). All results are averages of between three to five specimens, and the coefficient of variation is indicated in parentheses below each value. A total fracture energy value was not obtained for TiO_2 Gray specimens at 28 days because of an equipment failure. Sample results for flexural and fracture testing are detailed in the following subsections.

2.4.2.1. Flexural Properties

A force versus vertical displacement curve showing flexural testing of a plain FFC flexure beam at 28 days is plotted in Figure 2.3. The peak load (P_1), as well as the load and displacement at 1/150 of the span length are indicated in the figure since they are used for calculation of the flexural properties. In the sample plot in Figure 2.3 after reaching the peak load (31.8 kN) and monotonically decreasing to roughly 10 kN, most specimens tested maintained their load with increasing deformation because of the higher fiber dosage.

Table 2-3 Summary of mechanical testing results

	7 Days				28 Days		
	Plain FFC	White TiO_2	Gray TiO_2	Plain FFC (Bordelon 2011)	Plain FFC	Gray TiO_2	Plain FFC (Bordelon 2011)
Flexural Properties							
MOR (MPa)	4.22 (3%)	3.83 (5%)	3.41 (2%)	3.78 (8%)	3.76 (2%)	3.58 (5%)	5.02 (10%)
f_{150} (MPa)	1.60	1.24	1.23	1.80	1.42	1.47	1.41

	(10%)	(13%)	(6%)	(17%)	(6%)	(6%)	(7%)
R_{150} (%)	39.9 (6%)	35.5 (16%)	39.9 (8%)	47.6 (12%)	40.1 (6%)	43.4 (3%)	28.0 (9%)
Fracture Properties							
P_c (kN)	3.21 (5%)	3.00 (4%)	2.98 (4%)	4.24 (8%)	3.64 (3%)	3.61 (3%)	4.21 (11%)
K_{Ic} (MPa·m$^{1/2}$)	0.977 (4%)	0.939 (6%)	0.980 (8%)	1.24 (6%)	1.05 (6%)	1.07 (11%)	1.26 (17%)
$CMOD_c$ (mm)	0.0213 (14%)	0.0219 (13%)	0.0263 (10%)	0.026 (3%)	0.0203 (15%)	0.0216 (24%)	0.0190 (16%)
G_{Ic} (N/m)	44.0 (5%)	43.1 (11%)	48.6 (11%)	63.2 (14%)	45.7 (11%)	49.0 (19%)	52.8 (27%)
G_{total} (N/m)	6428.9 (4%)	5956.9 (6%)	5260.2 (14%)	3691 (55%)	5595.0 (21%)		3175 (14%)
Strength Properties							
f'_c (MPa)	30.0 (7%)	26.9 (14%)	32.8 (5%)	35.8 (1%)	44.5 (1%)	43.8 (2%)	41.5 (9%)
f'_{sp} (MPa)	3.24 (11%)	3.05 (8%)	3.81 (5%)	3.49 (40%)	4.01 (3%)	4.05 (4%)	4.25 (5%)

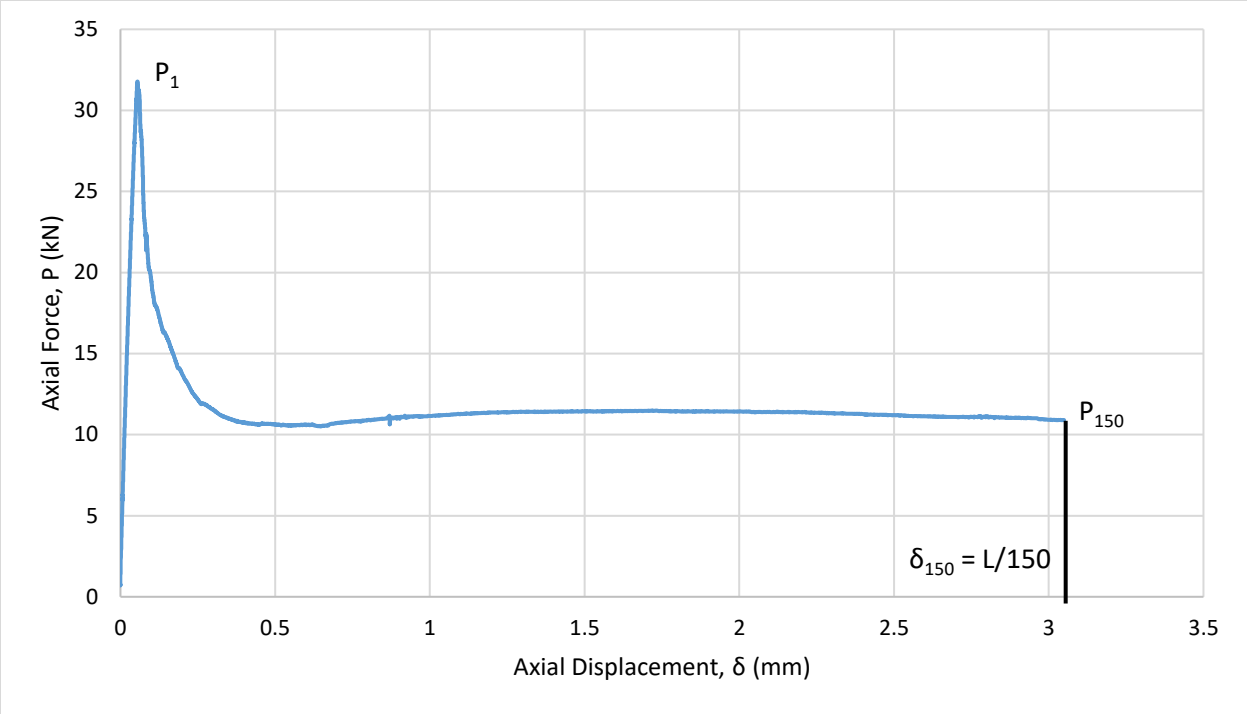

Figure 2-3 Sample flexural test result for Plain FFC specimen at 28 days

2.4.2.2. Fracture Properties

A sample force versus opening displacement curve showing the initial loading and re-loading of a Plain FFC fracture beam specimen at 28 days is shown in Figure 2.4. The plot ends upon reaching the re-loading peak. The points on the curve that were used to determine the slope for initial loading (c_i) and unloading (c_u) compliance, which were used in the calculation of the fracture properties based on Shah (1990), are indicated in Figure 2.4.

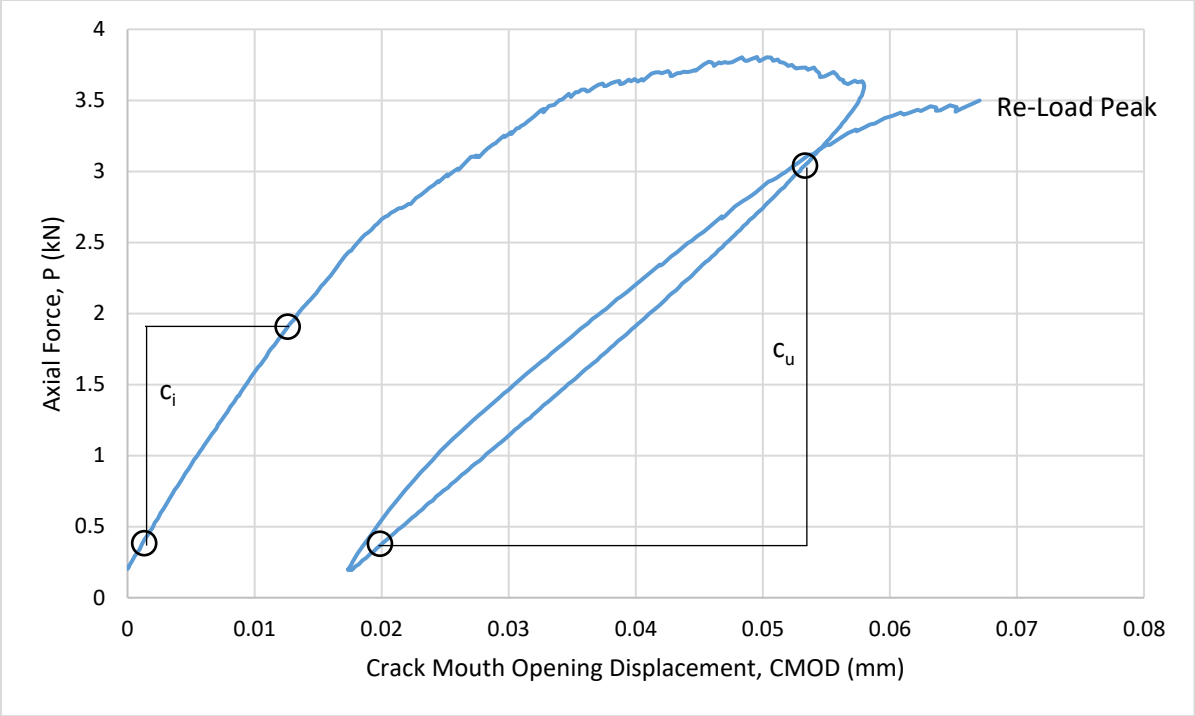

Figure 2-4 Initial loading and re-loading of Plain FFC single edge notched beam specimen at 28 days

A full force versus displacement curve used for calculation of total fracture energy is plotted in Figure 2.5. There were two jumps in axial force corresponding to increases in loading rate during the test, which are indicated in Figure 2.5. These jumps were typical for loading rate increases during all tests. Note that the test did not proceed to complete failure (P = 0 kN), but was stopped at P = 0.02 kN because of equipment limitations. The CTOD at P = 0 kN was determined by extrapolating from the last 1,000 data points.

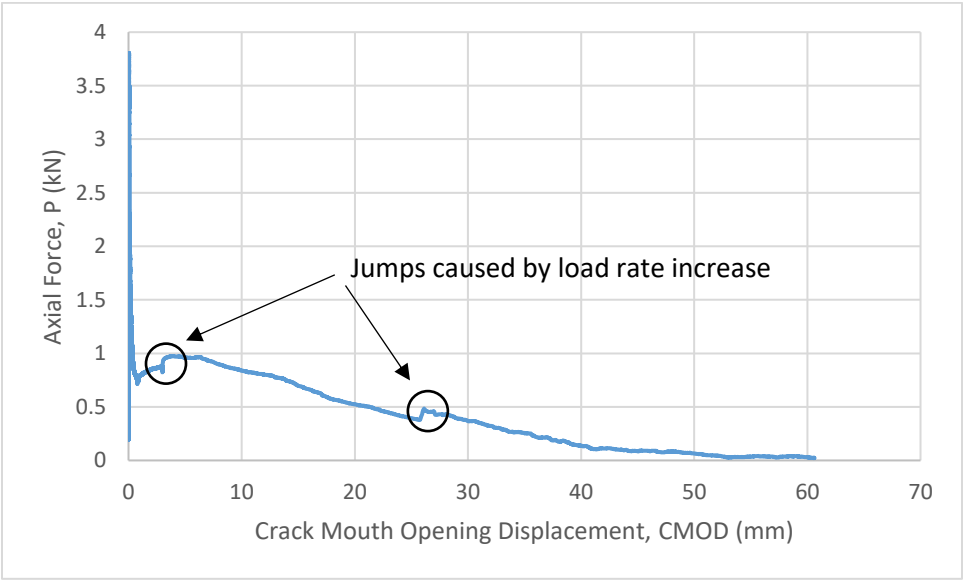

Figure 2-5 Full force vs. displacement plot for fracture testing of Plain FFC single edge notched beam at 28 days

2.5. DISCUSSION OF RESULTS

2.5.1. Fresh Properties

As expected from the literature, the workability was decreased in the White and Gray TiO_2 mixes compared to the Plain FFC mix. The nanoparticles in the photocatalytic cement blend appear to have reduced the slump flow. However, as seen in Table 2.2, the average slump flow diameter of all mixes in this study exceeded the slump flow measured by Bordelon and Roesler (2011), which is more than sufficient for achieving the workability necessary to construct thin inlays in the field.

It is likely that the increased slump flow for the mixes in this study resulted from the increased amount of HRWR. However, these increased dosages (1700-2000 ml/m^3) did not appear to have any deleterious effects on any other concrete properties and were still well within a feasible range for flowable fibrous concrete. In fact, Bordelon and Roesler (2011) had to substantially increase the amount of HRWR from 1100 to 2700 ml/m^3 when constructing the field FFC test section. Therefore, while some adjustment and optimization to the plasticizers are needed when developing a photocatalytic FFC mix, the workability appears to be more than sufficient for field application.

As opposed to workability, air content results were inconsistent with those previously found by researchers. Panesar and Dolatabadi (2014) found that, using the same amount of AEA, it was significantly more difficult to entrain air in photocatalytic concrete. In this study, air content was higher for the Gray TiO_2 mix than the Plain FFC mix, although values were within 1%. The White TiO_2 mix, however, had an air content of 8.8%, which was significantly higher than any other values found in this study or previously.

One possible explanation for the air content of the White TiO_2 is the chemical difference between white and gray cements. Differences in carbon content, for example, are known to effect air entrainment ability, although this effect is typically associated with activated carbon in fly ash. While it was not the objective to determine why differences were observed in the air content of the photocatalytic FFC mixes, it was verified that sufficient air entrainment can be achieved. As with the water reducing admixtures, testing and optimization of the air entraining admixture dosage is necessary when developing a photocatalytic FFC mixture.

2.5.2. Mechanical Properties

2.5.2.1. Compressive and Splitting Tensile Strengths

Based on the results shown in Table 2.3, there was no statistically significant (95% confidence interval) difference in compressive and splitting tensile strengths between the Plain FFC mix and the White and Gray TiO_2 mixes at either 7 or 28 days. Ultimately, even with the replacement of some cement with TiO_2, the nanoparticles did not appear to have a significant effect on strength values. These results appear reasonable given that certain studies in the literature found increases in compressive strength while others observed decreases.

The 7 day compressive strengths of all three mixes were somewhat lower than the 7 day compressive strength obtained by Bordelon (2011) for Plain FFC, but otherwise all values were similar. Also, with the exception of 7 day splitting tensile strength, values were virtually the same between White and Gray TiO_2. The higher tensile strength result for Gray TiO_2 may have simply been a function of variance in the samples or the test method.

2.5.2.2. Flexural Properties

With respect to flexural properties, there were some statistically significant (95% C.I.) differences between the Plain FFC and photocatalytic FFC mixes. As seen in Table 2.3, at 7 days, the Plain FFC mix had both a higher modulus of rupture (flexural strength) and residual strength ratio (f_{150}) than either of the photocatalytic FFC mixes. Residual strength ratios were similar, although that result would be expected since it is a ratio of residual to flexural strength. Despite this difference, the modulus of rupture for TiO_2-containing mixtures was on par with the FFC mix tested by Bordelon (2011), though the residual strengths of the photocatalytic mixture were much lower.

In spite of the differences observed at 7 days, at 28 days the flexural properties of the Plain FFC and photocatalytic FFC mixes were once again statistically the same. TiO_2-containing cement is expected to have a faster early setting time, so it would not necessarily be expected for the photocatalytic mix to catch up in strength at 28 days. Instead, the convergence (or disparity at 7 days) may have been caused by sample or test variance.

As noted in Table 2.3, the flexural strength values do not change much from 7 to 28 days for either the plain or photocatalytic FFC mixes. In fact, both the modulus of rupture and residual strength values of the Plain FFC decrease at 28 days. Bordelon (2011) also found that residual strength decreased at 28 days. These findings make sense when considering that the fibers will likely have a higher bond strength with the concrete at 28 days, making them more likely to fail by breaking as opposed to pull-out. Similar discrepancies at 7 and 28 days were observed with respect to certain fracture properties as well, which will be detailed in the next subsection. Overall, flexural and residual strength ratios for the photocatalytic FFC mix appears to be sufficient for use in thin inlays.

2.5.2.3. Fracture Properties

As with compressive and splitting tensile strengths, there was no statistically significant (95% C.I.) difference in any of the fracture properties between the Plain FFC and photocatalytic FFC mixtures. The peak loads and initial fracture energies were somewhat lower in this experiment than found by Bordelon (2011). Otherwise, the majority of fracture properties agreed reasonably well, as seen in Table 2.3.

For the most part, fracture values for the plain and TiO_2-containing mix designs demonstrated modest increases from 7 to 28 days. Looking at Table 2.3, however, there are also a few more examples of values decreasing at 28 days compared to 7 days, particularly in the properties measured by Bordelon (2011). The coefficient of variation for many of the fracture properties was quite high, so the test method may have been the primary source of this discrepancy.

Finally, a large increase in total fracture energy was observed in all specimens compared to the FFC specimens tested by Bordelon (2011). This increase was likely a result of not rodding the beams during casting. By not rodding the fresh concrete in a downward vertical direction, the fibers may have set into place in a preferential alignment along the width of the beam, allowing a greater number of fibers to bridge the crack that developed at the notch. An image of a single

edge notched beam during testing is shown in Figure 2.6, with the fibers visible across the fracture plane. These results are consistent with those of Bordelon (2011), who showed that improved fiber alignment in the interior of the single edge notched beams improves fracture performance. (This finding by Bordelon was independent of the results listed in Table 2.3. No special treatment was given to those specimens to promote fiber alignment.)

Figure 2-6 Fibers bridging the crack in a single edge notched beam specimen

2.6. CONCLUSIONS

Thin inlays for pavement preservation have the potential to be a very useful application for photocatalytic concrete since it offers multi-functional benefits. By incorporating TiO_2 nanoparticles into flowable fibrous concrete for inlays, the enhanced constructability and field performance of FFC mixes can be combined with the emission reduction benefits of photocatalytic concrete. To ensure that a photocatalytic FFC mix may be successfully used for thin inlays, fresh and mechanical properties were measured and compared to a control FFC mix.

For fresh concrete, adding photocatalytic cement led to a slight decrease in workability, which agreed with findings in the literature. Overall, the mix was still sufficiently flowable for inlay applications. There were some inconsistencies with respect to the effect of the TiO_2 on the ability to entrain air, with the White TiO_2 mix featuring an unusually high air content. However, since high air contents were able to be achieved in the photocatalytic mixes, it was not especially concerning. To ensure best mix performance, care should be taken when developing a photocatalytic mix design to ensure that optimal doses of water-reducing and air-entraining admixtures are applied.

Strength and fracture properties of the photocatalytic concrete mixes were, for the most part, statistically the same as the control mix and previous findings on FFC mixtures. The finding of little to no change in compressive strength is reasonable based on the literature. Measured at 7

days, the flexural strengths of the photocatalytic mixes were lower than the Plain FFC mix, which would support the idea that replacing some Portland cement with TiO_2 may lead to slight decreases in strength (Panesar and Dolatabadi 2014). However, this disparity disappeared at 28 days. The similarities in the remainder of the mechanical properties analyzed in the experiment suggest that TiO_2-containing concrete should be expected to perform about as well as plain concrete mixtures without any special adjustments to the mix. In general, mechanical strengths obtained in this experiment appear suitable for thin inlay applications.

Fracture testing of the single edge notched beams provided evidence that promoting preferential fiber alignment can greatly enhance the total amount of energy required to open up a full-depth crack in a concrete inlay. Although it may not be possible to obtain enough control to dictate fiber alignment when placing a thin inlay in the field, Bordelon (2011) noted that this type of beneficial fiber alignment may naturally occur if the length of the macro-fibers was close to that of the thickness of the overlay. Therefore, for certain design thicknesses and fiber lengths, it may be possible to optimize a photocatalytic FFC inlay to achieve very high fracture resistance, which could be very beneficial to long-term pavement performance.

Overall, photocatalytic FFC inlays appear to provide the same benefits to constructability and cracking resistance offered by conventional FFC mixes, and mechanical strengths should be more than sufficient for thin inlay applications. Defining the mechanical properties may also useful in predicting the long-term performance of photocatalytic concrete, which is important in developing new and useful applications and for analyses such as life cycle assessment.

CHAPTER 3- PHOTOCATALYTIC PERFORMANCE OF MORTAR SPECIMENS

3.1. INTRODUCTION

There are several potential applications of photocatalytic concrete containing titanium dioxide (TiO_2) to combat pollution and benefit the environment, varying from treating runoff water, improving indoor air quality, more self-cleaning surface, and reducing heat island effects by increasing surface albedo in urban areas. However, the most extensively studied application for photocatalytic cements has been reducing nitrogen oxide (NOx) levels in the urban outdoor environment.

The near-road environment, because of vehicular NOx emissions and their harmful effects to human health and contributions to smog, acid rain, and tropospheric ozone (Environmental Protection Agency 2010), has been a major area of study. The US EPA, like many other regulatory agencies worldwide, has traditionally performed annual area-wide monitoring and regulation of concentrations of nitrogen dioxide (NO_2), with NO_2 considered an indicator for all nitrogen oxides (as NO will oxidize into NO_2 in the air). In 2010, the EPA extended its regulations to cover near-road emissions in response to studies showing heightened rates of respiratory illness in populations living near roadways. The EPA now mandates monitoring of NO_2 levels within 50m of roadways, and has set a one-hour peak NO_2 maximum of 100 ppb (Environmental Protection Agency 2010). Multiple studies of air pollution near highways and urban roadways in Texas (Clements *et al.* 2009), North Carolina (Thoma *et al.* 2008), Germany, and Denmark (Berkowicz 2000) have shown NOx and NO_2 levels approaching the US EPA standard limit.

With new understanding of the harmful effects of NOx and a mandate to improve air quality near roadways, there is a need to find ways to mitigate NOx pollution in the near-road environment. Concrete pavements are one promising method of application for photocatalytic cementitious materials, offering the ability to improve air quality right underneath the primary source of near-road NOx emissions as well as provide a long-term, high mobility riding surface. While the potential for photocatalytic concrete to remove NOx from the air has been studied in both the laboratory and the field, the ability of photocatalytic concrete pavements to continuously and reliably remove NOx as well as future applications, optimal concrete mix designs, and the effect of environmental conditions on performance are all questions requiring answers.

To help further characterize the environmental benefits of photocatalytic concrete pavements, and photocatalytic flowable fibrous concrete (FFC) specifically, mortar mixes were prepared for laboratory photoreactor testing. Samples were evaluated for NOx removal ability as well as to determine the impact of factors such as carbonation, addition of supplementary cementitious materials, and surface reflectance on photocatalytic activity, all of which are crucial to the performance of a photocatalytic pavement.

3.2. LITERATURE REVIEW

3.2.1. Photocatalytic Cementitious Materials

3.2.1.1. TiO_2 Photocatalysis

Semiconducting TiO_2 nanoparticles are activated by UV-A radiation from sunlight, rendering them capable of reacting with a host of pollutants in air or water (Devahasdin *et al.* 2003, Ballari *et al.* 2010). TiO_2 photocatalysis has been studied for treatment and mitigation of carbon monoxide (Hwang *et al.* 2003), sulfur dioxide (Zhao *et al.* 2009), hydrocarbons (Crittenden 1996, Cackler *et al.* 2012), and VOCs (Chen *et al.* 2011, Husken *et al.* 2009), among other pollutants, all in a range of different environments. For pavements in the near-road environment, TiO_2 photocatalysis for oxidation of nitrogen oxides (NOx) is of greatest interest.

Multiple types of crystalline TiO_2 nanoparticles exist, but in terms of photocatalytic ability, anatase TiO_2 is the most photocatalytically active (Terepulik 2012, Hanson and Tikalsky 2013). Some commercial TiO_2 products are speculated to be blends of different types of TiO_2, including rutile, and some researchers have shown that adding small amounts of other TiO_2 phases may help improve performance (Poon and Cheung 2007). However, even with these blends, anatase is the primary constituent and most photocatalytically active form of TiO_2.

3.2.1.2. NOx Reaction Mechanism

The photocatalytic reaction with NOx at the surface of a photocatalytic pavement (or at any photocatalytic surface) proceeds according to Equations 3.1 through 3.5, which are adapted here from Ballari *et al.* (2010). First, TiO_2 (within the cementitious matrix or applied to the surface) is activated by UV-A radiation, creating an electron-hole pair. This results in the production of hydroxide free radicals (·OH), which spur oxidation-reduction reactions with NO and NO_2 in the air. Ultimately, NOx will be converted into nitrate byproducts, which accumulate on the pavement surface. This process as it occurs at a pavement surface in the near-road environment is illustrated by the schematic in Figure 3.1.

$$TiO_2 + h\nu \rightarrow h^+ + e^- \quad (3.1)$$

$$H_2O_{ads} + h^+ \rightarrow \cdot OH + H^+ \quad (3.2)$$

$$NO_{ads} + \cdot OH \rightarrow HNO_2 \quad (3.3)$$

$$HNO_2 + \cdot OH \rightarrow NO_{2\,ads} + H_2O \quad (3.4)$$

$$NO_{2\,ads} + \cdot OH \rightarrow HNO_3 \quad (3.5)$$

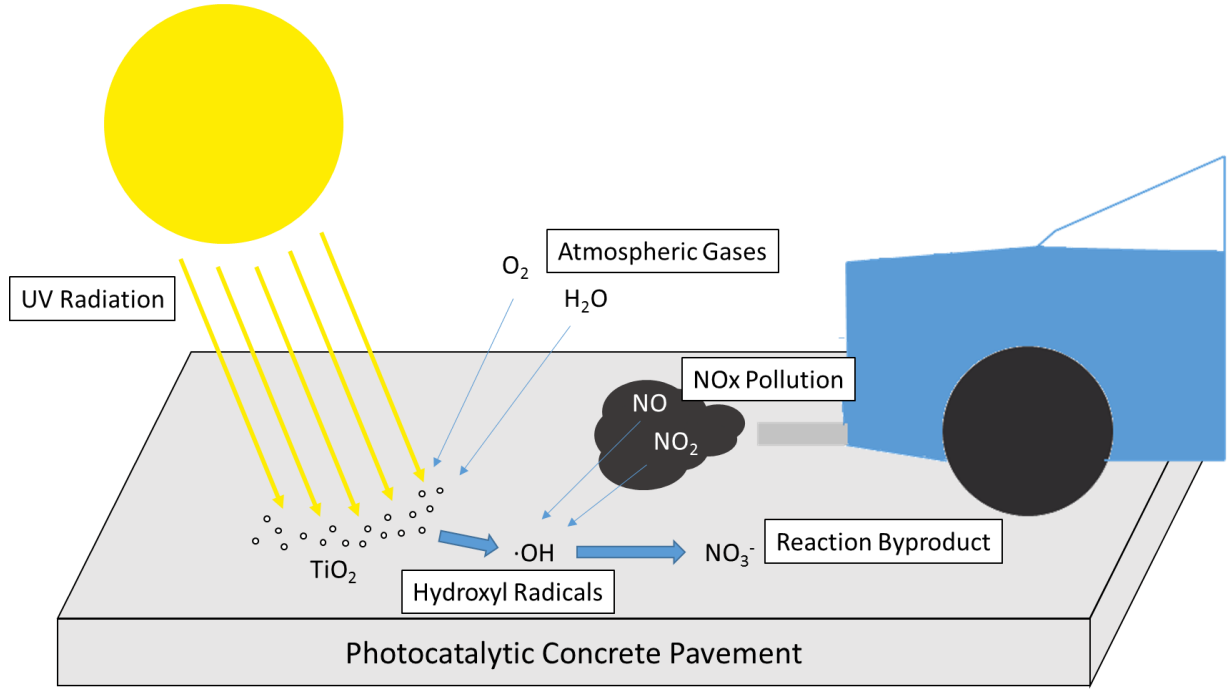

Figure 3-1 Overview of photocatalytic reaction at pavement surface

Researchers have confirmed through laboratory and field testing that the NO_3^- byproducts accumulate on the sample surface after photocatalytic reaction with NOx (Nakamura *et al.* 2000, Dalton *et al.* 2002, Cackler *et al.* 2012). These nitrates may also become bound either by alkalines dissolved in the concrete pore solution (Husken *et al.* 2009) or within the cementitious matrix as $CaNO_3$ (Cackler *et al.* 2012). Further studies have shown that nitrates that have accumulated on the surface will wash off the surface when exposed to water or rain (Bygott *et al.* 2007, Osborn *et al.* 2012, Cackler *et al.* 2012). Although nitrates can be harmful in water, measured concentrations in runoff water from photocatalytic pavements have been shown to be well below the US EPA drinking water standard (Cackler *et al.* 2012).

3.2.1.3. Incorporation of TiO_2 into Cementitious Materials

There are two primary methods in which TiO_2 nanoparticles are incorporated into cementitious materials. The first method is to mix TiO_2 directly into the cementitious matrix to produce photocatalytic paste, mortar, and concrete samples. This method has been used by many researchers (Chen and Poon 2009, Husken *et al.* 2009, Ballari *et al.* 2010, Guo and Poon 2012, Sikkema 2012, Boonen and Beeldens 2013, Diamanti *et al.* 2013, Sikkema *et al.* 2013, Hanson 2014, Lee *et al.* 2014, Jayapalan *et al.* 2015, Poon and Guo 2015), as well as in this study for FFC mixes. For full-depth samples, some studies have used photocatalytic cement blends that contain a certain amount of TiO_2, whereas other researchers have mixed a certain amount of nanoparticles directly into the mixture. Studies requiring larger samples or test sections typically require commercial products, as it would otherwise be difficult to obtain the necessary quantities of TiO_2 nanoparticles.

Adding TiO_2 to a full-depth concrete structure is expensive. Several researchers have explored the concept of applying cementitious TiO_2 materials using stucco (cement-based) products (Terepulik 2012), within concrete paving blocks (Guerrini and Peccati 2007), as thin cement-based weathering layers on top of concrete paving blocks (Poon and Cheung 2007, Boonen and

Beeldens 2013), or exploring strategies such as two-lift paving (Beeldens and Boonen 2012, Cackler *et al.* 2012), in which a relatively thin photocatalytic concrete layer is paved on top of a conventional concrete layer (wet-on-wet) to create a full-depth concrete structure. A thin flowable fibrous concrete (FFC) inlay for preservation overlays or inlays, as explored in Chapter 2, also addresses the cost issue by only incorporating into overlays.

Researchers have also successfully incorporated TiO_2 into pervious concrete mixtures. Shen *et al.* (2012) and Asadi *et al.* (2012) found in laboratory testing that pervious concrete with TiO_2 offered better photocatalytic performance than conventional TiO_2-containing concrete. In particular, Asadi *et al.* (2012) created two-lift laboratory photocatalytic pervious concrete samples in the laboratory in which a top layer containing TiO_2 was cast directly over a conventional pervious concrete layer, and noted that NOx removal efficiency increased with increasing depth of the photocatalytically active layer. Sikkema (2013), on the other hand, performed a similar study with two-lift pervious concrete specimens and did not find a significant increase in NOx removal efficiency or any correlation with photocatalytic layer depth.

The second common method for incorporating TiO_2 nanoparticles into cementitious materials is through dispersed surface applications, primarily including water- or paint- based sprays and coatings (Diamanti *et al.* 2008, Dylla *et al.* 2012, Guo and Poon 2012, Osborn *et al.* 2012, Terepulik 2012, Boonen and Beeldens 2013, Hanson 2014). One benefit to using this type of surface coating is that it can be practically applied to a wider range of structures and geometries, such as roadside structures (Terpeluk 2012) or tunnel walls (Boonen and Beeldens 2013). Additionally, several studies have shown that surface coatings may exhibit enhanced photocatalytic performance, discussed in Section 3.2.3.4, but perhaps at the cost of durability.

3.2.1.4. Self-Cleaning Ability

Adding TiO_2 nanoparticles to a concrete surface or into the cementitious matrix also imparts superhydrophilic properties onto the concrete (Diamanti *et al.* 2008). The primary benefit that this property imparts onto concrete is that it allows water to constantly flush and clean the surface, with multiple studies confirming this "self-cleaning" ability of photocatalytic cementitious materials (Diamanti *et al.* 2008, Folli *et al.* 2009, Chen *et al.* 2011). Diamanti *et al.* (2008) reported a direct correlation between photocatalytic mortar specimens with a higher TiO_2 content (and thus higher NOx removal efficiency) and a lower contact angle with water (greater degree of hydrophilicity), directly linking the nanoparticles to the superhydrophilic behavior.

As with any type of infrastructure, photocatalytic concrete stands to become contaminated when exposed to the outdoor environment. As discussed in section 3.2.3.6, this contamination is accompanied by a decline in photocatalytic performance. Although there have been some contradictory findings in the literature with respect to effectiveness of the concrete to clean itself or if it needs more proactive maintenance, the self-cleaning properties of the material should allow for rejuvenation of its photocatalytic ability assuming water is periodically present on the surface.

3.2.2. Testing of Photocatalytic Cementitious Materials

The most extensive testing of photocatalytic cementitious materials has been performed in bench-scale laboratory experiments. Tests performed in a controlled environment have allowed for intensive study of the mechanisms and kinetics of the photocatalytic reaction and the numerous variables that affect the NOx removal ability. Field testing is less common and much

more complicated than laboratory testing because of the logistics, extra costs, additional variables to consider or control, and limitations of the testing devices.

3.2.2.1. Laboratory Test Methods

Laboratory testing of photocatalytic cementitious materials is standardized under ISO 22197-1 (2007). In the standard test method, a ceramic specimen (in this case, paste, mortar, or concrete containing or coated with TiO_2) is placed in a sealed photoreactor chamber with a translucent lid (made from borosilicate glass) and illuminated by an overhead UV lamp. A test gas is prepared by mixing zero air with NO. Regulated by mass flow controllers, the test gas is humidified to the desired relative humidity and directed to the photoreactor, where it passes over the test specimen. The photoreactor configuration outlined in the standard allows for the test gas to achieve laminar flow (Ballari *et al.* 2010). Downstream from the photoreactor chamber is a chemiluminescence NOx analyzer, which measures NO, NO_2, and NOx concentrations in the test gas stream in real-time (typically one minute averages). A diagram of the ISO standard test setup is shown in Figure 3.2.

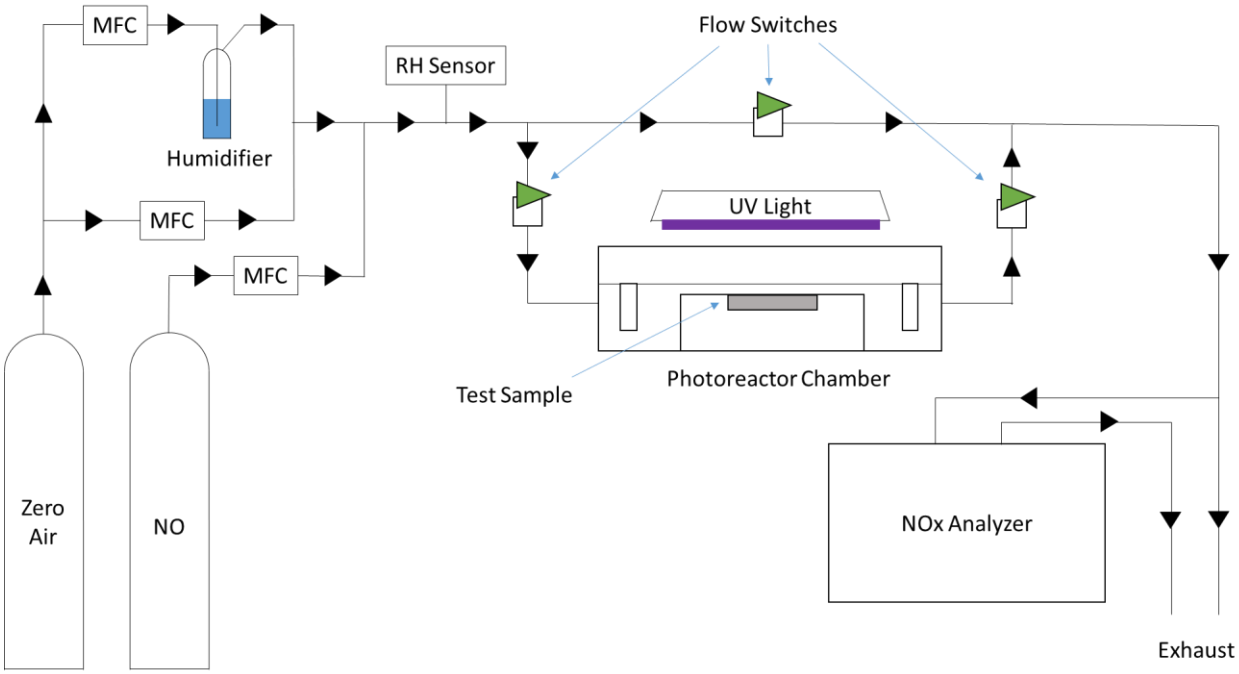

Figure 3-2 Test setup according to ISO 22197-1

Before the test begins, specimens are washed in order to remove contaminants and/or reactant products from previous photocatalysis. Specimens are then placed in the photoreactor chamber. Before the test can begin, the test gas containing NO is allowed to flow over the surface for 30 minutes while the UV-A source is covered or moved/directed elsewhere. This period before the test allows for stability in the flow over the sample as well as in the illumination from the lamp. After 30 minutes, the UV source is allowed to shine over the sample and testing proceeds for five hours.

ISO 22197-1 also allows for indirect characterization of NOx removal by measuring the amount of reaction byproducts that have deposited on the sample surface, a test known as the elution test (ISO 2007). In elution testing, after the five-hour exposure to the NO test gas, the sample is

submerged in purified water. The water is then analyzed using ion chromatography to measure the amount of nitrates that washed off the specimen, an indirect method of measuring the photocatalytic activity of the specimen.

Elution testing may not provide a complete picture of photocatalytic performance. While Nakamura *et al.* (2000) reported that measured nitrate levels measured from ion chromatography were in line with the NOx removal amount measured by chemiluminescence, other researchers have reported that nitrate concentrations measured from elution testing were either very low (Terepulik 2012) or lower than expected compared to photoreactor testing (Cackler *et al.* 2012). For testing of cementitious materials, this disparity indicates that elution testing may not be able to account for nitrates that end up bound in the sample surface as $CaNO_3$.

3.2.2.2. Field Test Methods

While a standard test method has been successfully developed for laboratory evaluation of photocatalytic cementitious materials, full-scale field testing to determine real-time performance of an in-place photocatalytic pavement is rare. A number of factors make such testing very costly and complex, particularly when it comes to deciding where, when, and how to measure NOx concentrations. Another complicating factor is the unpredictability of certain environmental variables, such as sunlight, weather, relative humidity, and wind speed, and determining how to account for them.

A few attempts at field tests have only indirectly measured photocatalytic performance. Though not pavement-related, Bygott *et al.* (2007) measured background NOx concentrations near a building façade treated with a photocatalytic coating over several months using chemiluminescence analyzers and diffusion tubes. The effectiveness of the photocatalytic surface was inferred by measuring the impact on nearby air quality. For pavements, Beeldens and Boonen (2012) developed a mobile photoreactor frame that could be brought into the field and fastened to the surface. While this test does not truly evaluate NOx removal in the near-road environment (only directly over the pavement at one given point while out-of-service), it does measure photocatalytic performance on a pavement that has been exposed to field conditions under actual sunlight.

Osborn *et al.* (2012) developed a device using plumber's putty that allowed small exposed pavement areas to be soaked in water. Similar to the laboratory elution test, the sampled water was brought back into the laboratory to measure the nitrate concentration. The concentration of nitrates that had been deposited on the surface could then be related to an amount of NOx in the air that reacted with the pavement surface. Like with the laboratory testing, the amount of NOx removal measured through nitrate analysis was lower than measured in the air.

Despite the challenges involved, a few researchers have attempted to conduct live, full-scale field testing to characterize NOx levels in the near-road environment. One such test was conducted in Bergamo, Italy, where NOx levels at a road section constructed with photocatalytic block pavers were compared with those at a control asphalt section in the same corridor (Guerrini and Peccati 2007). Testing was performed in real-time using chemiluminescence NOx analyzers placed in portable street cabinets at heights between 0.3 m and 1.8 m above the pavement surface. The experiment was done two weeks at a time, and 8-hour mean average NOx concentrations were calculated for each day. The study reported reductions in NOx concentrations as high as 49% in the photocatalytic pavement section compared to the control section, where peak NO_2 levels measured around 60 ppb. This disparity was highest during times

of day when traffic levels were highest. When traffic levels were low (such as at nighttime), no real difference was observed between the two sections.

Dylla *et al.* (2012) connected a chemiluminescence NOx analyzer to an air sampling line placed on a photocatalytic pavement surface in Louisiana to measure NOx concentration. This setup was capable of running while the pavement was in-service under live traffic and weather conditions, providing insight into trends caused by environmental factors in the field. However, pollutant concentrations and NOx removal rates reported in this study seemed unusually high. Because the pollutant concentrations were measured at the pavement surface, they may not be appropriate for comparing to the US EPA standards or the Bergamo study to characterize the overall effectiveness of photocatalytic pavements. The EPA recommends measuring NOx/NO_2 at heights of 2.5m to 3.5m (Environmental Protection Agency 2010), which is different from even the Bergamo test. The discrepancies in testing height between studies and the difficulty in comparing results highlights the challenges of conducting accurate field testing.

Cackler *et al.* (2012) implemented an experiment for a newly-opened roadway in Missouri featuring a photocatalytic concrete pavement where NOx measurements were made with passive diffusion monitors to measure pollutant levels over extended periods of time. The passive monitoring was designed to allow long-term measurements of NOx abatement that could account for seasonal or other types of fluctuations and uncertainty without the large cost associated with continuous real-time monitoring (e.g. chemiluminescence testing). These long-term measurements were accompanied by occasional real-time measurements, parallel chemiluminescence testing in the laboratory, water quality and solar reflectance tests. As of the summer of 2016, the full results of this study had not been published.

3.2.3. Factors Affecting Photocatalytic Efficiency

Laboratory and field testing of photocatalytic cementitious materials have identified many different factors that affect photocatalytic performance and quantified their impacts. An overview of some of the most relevant findings are included in the following section.

3.2.3.1. Relative Humidity

One of the most basic but also most important factors affecting photocatalytic efficiency is relative humidity (RH). The impact of relative humidity has been extensively tested in laboratory settings, where researchers have shown that as relative humidity increases, NOx removal ability decreases (Pinna *et al.* 2007, Dylla *et al.* 2011, Boonen and Beeldens 2013, Sikkema 2013, Hanson 2014). Dylla *et al.* (2012) measured a decreasing photocatalytic performance with increasing relative humidity in a field test section.

The accepted explanation for this phenomenon is that water molecules compete with NO and NO_2 for adsorption onto photocatalytic concrete surfaces (Pinna *et al.* 2007, Boonen and Beeldens 2013). Therefore, in high humidity environments where a greater number of water molecules are available, fewer NOx molecules are adsorbed and there are fewer reactions with TiO_2.

3.2.3.2. Flow Rate and NOx Concentration

Flow rate and NOx concentration are two variables that have been shown to affect the reaction kinetics of TiO_2 photocatalysis. Devahasdin *et al.* (2003) determined that the photocatalytic activity of TiO_2 during laboratory testing was inversely related to the residence time of the test gas over the sample. At a lower flow rate, a greater amount of NOx was removed from the test gas stream. Additionally, for a given flow rate, a greater percentage of NOx would be converted to byproducts when a lower concentration of NOx was present in the test gas. The researchers successfully described this behavior using the Langmuir-Hinshelwood model, which helped determine the reaction mechanism.

Following up on the work by Devahasdin *et al.*, other studies have verified these relationships in laboratory testing (Husken *et al.* 2009, Sikkema 2013, Hanson 2014). Additionally, some field tests have measured wind speed and direction and related those factors to results. It would be reasonable to believe that wind speed would affect the residence time, and therefore impact photocatalytic activity. Dylla *et al.* (2012) found that NOx removal rate decreased in windier conditions, although relative wind direction to the photocatalytic surface may also have played a role in the results. The comprehensive field study in Bergamo, Italy (Guerrini and Peccati 2007) was performed in conditions with negligible wind speeds.

3.2.3.3. Light Intensity

A number of researchers have studied the effect of UV light intensity on NOx removal ability of photocatalytic cementitious materials, consistently finding that higher light intensity leads to better photocatalytic performance (Devahasdin *et al.* 2003, Dillert *et al.* 2011, Hanson and Tikalasky 2013, Sikkema 2013). Given that the amount of UV light incident on a photocatalytic surface will vary in an outdoor setting depending on time of day weather conditions and geographic position, Hanson and Tikalsky (2013) varied UV light intensity in a laboratory photoreactor system to simulate sunny (UV irradiance of 13 W/m^2) and cloudy or shady conditions/shadows (1.5 W/m^2), reporting a photocatalytic efficiency that was 2.4 times higher at the greater UV intensity. Attempts by Dylla *et al.* (2012) to relate solar radiation to NOx removal in a field test section were inconclusive, likely because other factors influenced the test results.

3.2.3.4. Application Method and Rate

As previously discussed, the two primary applications of TiO_2 into cementitious materials are by mixing into the matrix or by applying a surface coating. Because test parameters between experiments can differ widely, the relative effectiveness of application methods can only be judged by experiments where their performance is compared directly. To date, studies that have measured performance side-by-side have tended to conclude that photocatalytic surface coatings of cementitious materials exhibit greater NOx removal ability than those where TiO_2 is mixed into the mass of the sample (Diamanti *et al.* 2008, Guo and Poon 2012, Boonen and Beeldens 2013).

One potential downside to photocatalytic surface coatings is that they may not be able to maintain high photocatalytic efficiency because of potential surface coating durability as compared to TiO_2 incorporated into the mass of concrete. Diamanti *et al.* (2008) noted that it may not always be possible for surface coatings to achieve optimum adhesion in all cases, leading to variation in performance and longevity of the coating. Boonen and Beeldens (2013) found that brushing and washing a TiO_2-coated surface can cause deterioration of its photocatalytic ability. These results are of particular importance when considering pavements, which are constantly traversed and abraded by traffic. In theory, concrete with TiO_2 nanoparticles mixed into the mass would not face this problem to the same extent since any wearing of the surface would expose subsurface nanoparticles to the environment. However, this particular experiment has not been investigated thoroughly.

In general, researchers have found a positive trend between the addition rate of TiO_2 and photocatalytic ability, with a higher TiO_2 content leading to more a higher level of NOx removal (Diamanti *et al.* 2008, Lucas *et al.* 2013, Hanson 2014). Several studies have suggested that there is an upper limit to TiO_2 content after which it no longer benefits the reaction. Lucas *et al.* (2013) found no further benefit to NOx removal after increasing TiO_2 content beyond 2.5% by mass of cement and suggested that excess TiO_2 may inhibit the reaction kinetics. Diamanti *et al.* (2013) found that the NOx removal performance of specimens at TiO_2 contents of 2.5% and 5% by mass of cement were basically the same.

3.2.3.5. Water/Cementitious Ratio

Several experiments with concrete or mortar samples containing TiO_2 nanoparticles in the mass have also analyzed the impact of the water/cementitious ratio (w/cm) ratio on photocatalytic performance. Results of these studies have consistently found that samples with a higher w/cm exhibit greater NOx removal ability (Diamanti *et al.* 2013, Lee *et al.* 2014). Much of the discussion on why w/cm ratio impacts photocatalytic performance centers around the porosity of the micrsotructure, which is explored in-depth in Chapter 4 of this report.

3.2.3.6. Contamination and Wearing of Photocatalytic Surfaces

Although photocatalytic concrete is self-cleaning, contamination is still a major concern for any infrastructure material, particularly for pavements. Several researchers have investigated the impacts of common environmental contaminants. Dylla *et al.* (2011) simulated contamination of photocatalytic concrete slabs by common roadway contaminants such as dirt and oil, finding that they had the potential to harm photocatalytic efficiency. Hanson (2014) found that blasting, sanding, and acid etching of mortar slabs also reduced photocatalytic efficiency.

In addition to environmental contamination, researchers have investigated whether the nitrate byproducts of the photocatalytic reaction themselves may harm the NOx removal ability of

photocatalytic concrete. In laboratory studies where photocatalytic concrete is left continuously exposed to NOx, a number of researchers have found that photocatalytic efficiency steadily declines over the course of days or weeks, eventually stabilizing at a lower efficiency than initial testing (Bygott *et al.* 2007, Sikkema *et al.* 2012, Boonen and Beeldens 2013). Sikkema *et al.* (2012) also found evidence using scanning electron microscopy that large deposits of a nitrogen-based substance were left deposited on sample surfaces.

While negative effects caused by contaminants call into question the resiliency of the material, the self-cleaning ability of photocatalytic concrete should help its longevity to be efficient. Many researchers have reported the ability to restore NOx removal efficiency to previous levels (or near previous levels) by washing and/or scrubbing photocatalytic specimens with water (Bygott *et al.* 2007, Boonen and Beeldens 2013) or other methods such as treatment with acid (Hanson 2014). If full photocatalytic ability can be restored to concrete simply by washing with water, photocatalytic infrastructure should prove resilient over time with normal maintenance or possibly just with rain. Some researchers were unable to restore photocatalytic activity by washing specimens with water (Sikkema *et al.* 2012, Hanson 2014), indicating that further research may be needed to determine how effective photocatalytic materials are over time, especially in the field.

A related concern to contamination is wearing of a photocatalytic surface. Researchers have simulated weathering and/or abrasion of photocatalytic concrete in the laboratory through methods such as rotary abrasion (Hassan *et al.* 2010) or treatment with abrasive paper (Guo and Poon 2012). In virtually all cases that were studied, wearing of the photocatalytic surface harmed NOx removal ability. Interestingly, Hassan *et al.* (2010) found that, when using a Hamburg wheel test on a concrete slab with a TiO_2 surface coating, in some cases the simulated abrasion sometimes increased photocatalytic efficiency, although it was not a statistically significant difference.

Some researchers have also left samples outdoors for extended periods of time before performing laboratory testing (Terpeluk 2012, Hanson 2014) to investigate the effects of weathering on a concrete sample. These studies generally found that increased exposure to the outdoor environment without corresponding attempts to clean or rejuvenate the surface led to a decrease in photocatalytic efficiency.

3.2.3.7. Carbonation

Although it is rarely considered in laboratory or short-term field testing, carbonation is an extremely important factor when considering the NOx removal ability of photocatalytic concrete. Carbonation occurs when calcium hydroxide (CH), typically the second most prevalent hydration product in the cementitious matrix, reacts with atmospheric carbon dioxide (CO_2) to precipitate calcium hydroxide ($CaCO_3$) (Mindess *et al.* 2003). With respect to photocatalytic concrete, laboratory testing employing artificial carbonation has shown that carbonation can significantly decrease NOx removal ability (Chen and Poon 2009, Diamanti *et al.* 2013, Hanson 2014). Carbonation is mostly unavoidable in concrete exposed to the atmosphere because of the prevalence of CO_2.

There are two main theories as to why carbonation causes a decline in photocatalytic efficiency. The first, proposed by Diamanti *et al.* (2013) and Hanson (2014), suggests that the precipitation of $CaCO_3$ shields the TiO_2 nanoparticles at the surface. Hanson supported this assertion by using energy-dispersive x-ray spectroscopy (EDS) measured a significant decrease in Ti on a

carbonated concrete surface, although there may be some problems with that analysis (explained in Chapter 4). The second, proposed by Chen and Poon (2009) and additionally by Hanson (2014), was that the $CaCO_3$ byproduct densified and reduced the porosity of the microstructure, allowing less UV-A radiation to reach the TiO2 and less adsorption of NOx. Chen and Poon also reported that porosity itself had a significant impact on NOx removal ability (higher porosity, higher photocatalytic ability), which is explored further in Chapter 4.

3.2.3.8. Concrete Reflectivity

Solar reflectance, or albedo, is a measure of how much incident light or radiation is reflected by a surface. Levinson and Akbari (2002) showed that concrete albedo is a function of the albedo of its constituent properties, with some constituents having a larger influence depending on their proportions in the mixture.

The albedo of photocatalytic concrete was initially investigated by researchers interested in reducing heat island effects, as well as to characterize the self-cleaning ability (Cackler *et al.* 2012). Sen *et al. (*2015) demonstrated that reflective photocatalytic concrete surfaces created with white cement can reduce heat island effects and global warming potential in an LCA analysis. Further research has indicated a possible link between reflectance and photocatalytic ability. Chen and Poon (2009), Terepulik (2012), and Poon and Guo (2015) reported that photocatalytic cement paste specimens created with white cement removed more NOx in laboratory testing than those made with gray cement. Poon and Guo (2015) suggested that the increased reflectivity of the white cement specimens is the primary factor driving this behavior. In a somewhat related finding, Poon and Cheung (2007) found that incorporating recycled glass aggregates into photocatalytic concrete pavers increased NOx removal efficiency. Because UV-A radiation initiates TiO_2 photocatalysis, reflectance in the UV-A spectrum is of particular interest for photocatalytic concrete.

3.3. EXPERIMENTAL PROCEDURES

3.3.1. Specimen Preparation and Test Matrix

Photocatalytic mortar specimens for NOx removal and reflectance testing were prepared based on the FFC mix design developed by Bordelon and Roesler (2012), later used by Sen *et al.* (2015) as well as described and presented in Chapter 2 of this report. Specimens were made with both commercial photocatalytic cements in which TiO_2 was pre-blended with Type I Portland cement (at an unknown addition rate), as well as by adding anatase TiO_2 powder directly into the mix at varying addition rates based on total cementitious content. The mortar specimens were mixed according to ASTM C305 (2014) with a w/cm of 0.40. The anatase TiO_2 powder was added photocatalytic specimens following the procedure described by Jayapalan *et al.* (2015). The specimen dimensions were 100 mm x 50 mm in surface area, complying with ISO 22197-1 (2007) for laboratory photoreactor testing.

Mix designs were varied based on cement type, and TiO_2 addition rate, and the addition of supplementary cementitious materials. Both white and gray commercial TiO_2 cement blends (referred to here as "White TiO_2" and "Gray TiO_2," respectively) were tested to measure the impact of the surface reflectance on photocatalytic efficiency. The samples where anatase TiO_2 was added directly ("Anatase") were prepared with gray Type I cement from the same manufacturer of the photocatalytic cement blends. Unlike the commercial cement blends, the

Anatase samples allowed studying the impact of varying the TiO_2 addition rate on NOx removal efficiency.

With respect to supplementary cementitious materials, the specimens containing each of the three cement types were mixed with either no SCMs, 15% fly ash, 30% fly ash, or 5% silica fume replacement. The variation in SCM content allowed for a study of the effects of carbonation on photocatalytic efficiency with and without SCMs. Fly ash and silica fume were expected to react with and reduce the amount of CH available in the cementitious matrix, reducing the potential for surface carbonation and its deleterious impact on photocatalytic efficiency.

With each combination of cement type, SCM, and TiO_2 addition rate, a total of 15 mix designs were evaluated (including a control sample containing gray Type I cement without TiO_2). All samples were moist cured for three days. After moist curing, samples marked for artificial carbonation were transferred to an incubator with a CO_2 content of 5% for 28 days, allowing for accelerated carbonation. (Atmospheric CO_2 content is around 0.04%.) During artificial carbonation, temperature was maintained at 22°C, and RH was held between 55-80%. Carbonation of the sample surfaces was confirmed by treatment with phenolphthalein.

3.3.2. Photoreactor Testing

Photoreactor testing was carried out according to ISO 22197-1 with a setup designed according to that shown in Figure 3.2. Standard test conditions and equipment included a test gas supplied by NO and zero air humidified to a relative humidity of 50%, use of a black light blue UV light source in the UV-A range at an irradiance of 10 W/m^2, total test time of five hours (with a 30 minute pre-test period where NOx flowed over the sample without UV illumination), a chemiluminescence analyzer to measure concentrations of NO, NO_2, and NOx, and the use of standard 50mm x 100 mm specimens as mentioned above. The specimen was oriented so that molded surface of the sample (not the finished/cast surface) was exposed to the test gas stream, i.e., face up.

Some modifications to the standard test conditions were adapted from recommendations outlined by Jayapalan *et al.* (2015) for optimum measurement of photocatalytic performance. These modifications from the ISO standard included lowering inlet NO concentration from 1000 ppb to 500 ppb and lowering the test gas flow rate from 3 Lpm to 1 Lpm. These changes were designed to make the test more representative of atmospheric conditions to which photocatalytic concrete pavements might be exposed and for ease of assessment of the relative performance of different mixes.

The quantity of NOx removed by the test sample during the experiment was characterized by the photocatalytic efficiency factor, PEF ($\mu mol/m^2 \cdot hr$), a term introduced by Jayapalan *et al.* (2015). Other researchers have also reported their results using similar units (Chen and Poon 2009, Sikkema 2013, Lee *et al.* 2014, Poon and Guo 2015). PEF is defined according to Equation 3.6 below, where f is flow rate (Lpm), A is sample's projected surface area (m^2), t is test time (hr), $[NOx]_{in}$ is the inlet NOx concentration (ppm) measured in the first 30 minutes of the test before the UV light is turned on, and $[NOx]_{out}$ is the NOx concentration (ppm) measured after the gas stream reacts with the sample illuminated by UV light. $[NOx]_{out}$ concentrations were measured continuously with a 30 second averaging time and integrated over the total test time to calculate PEF.

$$PEF = \frac{f}{22.4 \times A \times t} \int_0^t ([NOx]_{in} - [NOx]_{out}) dt \quad (3.6)$$

NOx removal efficiency of the reaction was also calculated according to Equation 3.7. The average $[NOx]_{out}$ across the entire test was subtracted from $[NOx]_{in}$ and expressed as a percentage of the inlet concentration.

$$NOx\ Removal\ Efficiency\ (\%) = 100 \frac{[NOx]_{in} - [NOx]_{out}}{[NOx]_{in}} \quad (3.7)$$

3.3.3. Spectrophotometer Testing

Laboratory spectrophotometer testing was performed to characterize the average solar reflectance, or albedo, of the photocatalytic specimens. As previously discussed, the albedo of concrete depends on the albedo of its constituent materials (Levinson and Akbari 2002). The constituents used to cast all the specimens tested in this study came from the concrete lab at the University of Illinois with the individual albedo values for these materials have been previously calculated by Sen (2015), as shown in Table 3.1.

Table 3-1 Albedo calculated for concrete constituents at the University of Illinois (Sen 2015)

Material	Albedo
Type I Cement	0.25
White TiO_2 Cement	0.80
Gray TiO_2 Cement	0.29
Sand	0.45
Class C Fly Ash	0.33
Silica Fume	0.18
Limestone Chip	0.57
Anatase TiO_2	0.98

Despite having an albedo of 0.98 across the entire UV-vis-IR spectrum, indicating near-total solar reflectance, the anatase TiO_2 nanoparticles were much less reflective in the UV-A spectrum alone. As shown in Figure 3.3, anatase TiO_2 nanoparticles were very absorptive in the UV-A spectrum overall and demonstrated nearly 100% absorption (i.e. 0% reflectance) in the range of approximately 335 to 360 nm. This finding is consistent with the TiO_2 photocatalytic reaction mechanism, where the nanoparticles absorb UV-A radiation. Additionally, Poon and Guo (2015) measured near 100% absorbance across the UV-A spectrum for a different TiO_2 nanoparticle powder produced by a different manufacturer.

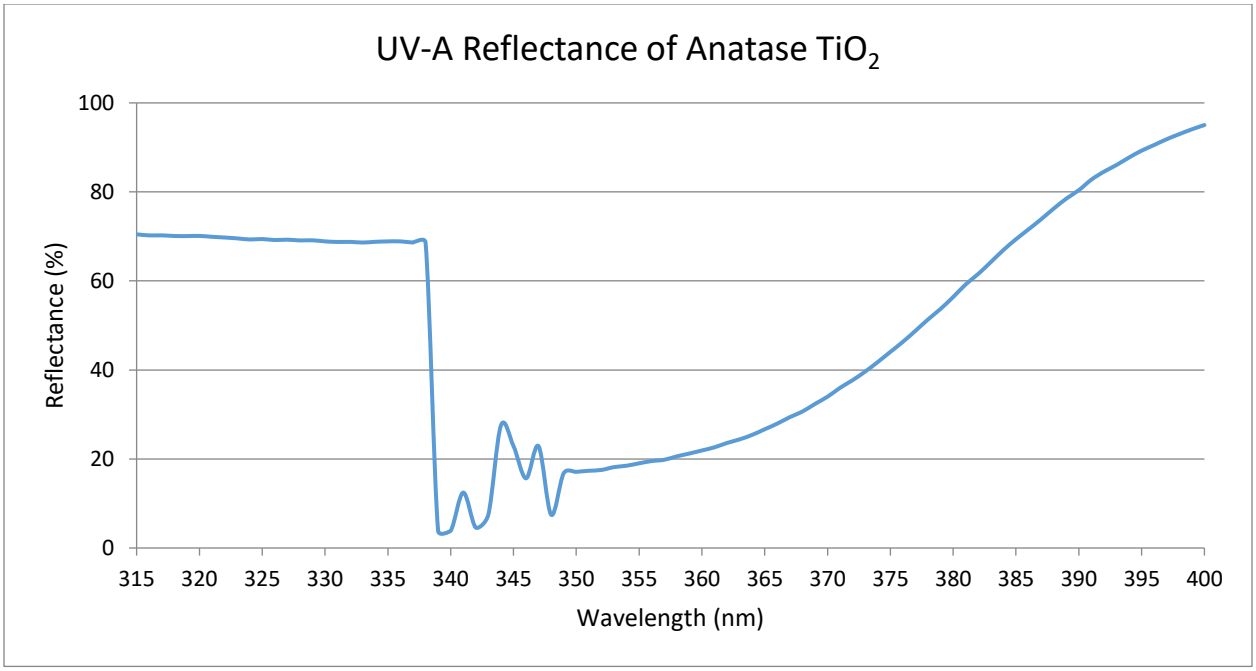

Figure 3-3 UV-A reflectance spectrum obtained for anatase TiO_2 (Sen 2015)

For this experiment, albedo was measured for the photocatalytic mortar specimens using a Cary 5000 UV-Vis-NIR spectrophotometer according to ASTM E903 (2012). The range of wavelengths, λ, analyzed by the instrument was 280 nm to 2600 nm, covering UV, visible, and near-infrared radiation spectra. Calculation of albedo was carried out using the standard reference solar spectrum contained in ASTM G173 (2003). The spectrophotometer used in this research is shown in Figure 3.4 with a White TiO_2 specimen in the device.

Figure 3-4 Spectrophotometer testing of a photocatalytic mortar sample

3.4. RESULTS

3.4.1. Laboratory Photoreactor Test

3.4.1.1. Typical Test Results

Typical photoreactor test results from individual samples are shown in Figures 3.5 through 3.7, which plot the concentrations (in ppb) of NO, NOx, and NO_2 over the course of the test. As seen in the figures, the inlet concentration was steady for the first 30 minutes of the test, i.e., inlet NO_x concentration matched the NO concentration, as there was no NO_2 in the test gas. At t = 30 minutes, the UV lamp was turned on, illuminating the test sample. Photocatalytic activity started immediately, marked by a large drop in NO concentration and the production of NO_2. A small concentration of NO_2 remained in the outlet stream, increasing slowly over the test time, but the majority of NO_2 generated during the test was also removed and converted to NO_3^- by the photocatalytic sample. After five hours of illumination, the UV light was turned off and NOx concentrations returned to inlet levels.

The three results shown in Figures 3.5 through 3.7 were chosen to highlight variation seen in the results. The specimens tested in Figures 3.5 and 3.6 demonstrated a high degree of photoactivity, while the specimen in Figure 3.7 was not as effective at removing NOx. In the test shown in Figure 3.5, the NOx concentration remained steady throughout the five hours of UV illumination, which was typical of most individual specimens. However, occasionally the NOx concentration would decrease or increase over time during illumination, as shown in Figures 3.6 and 3.7, respectively.

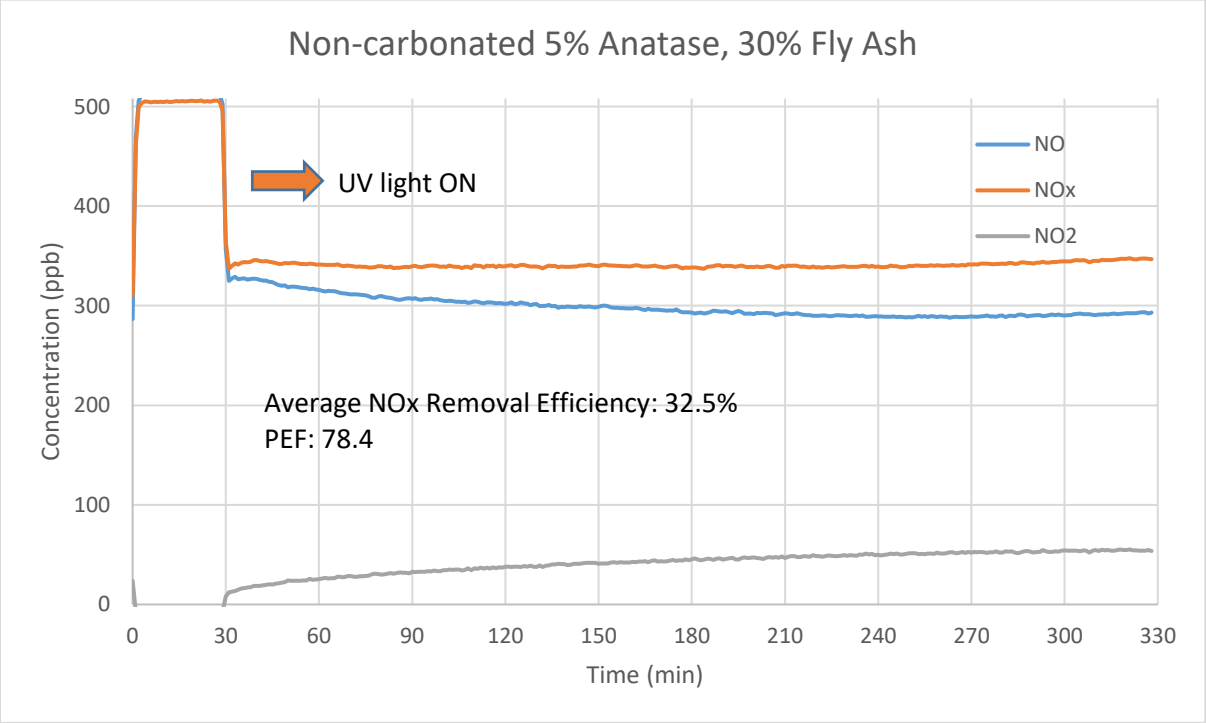

Figure 3-5 Non-carbonated 5% Anatase, 30% Fly Ash test result

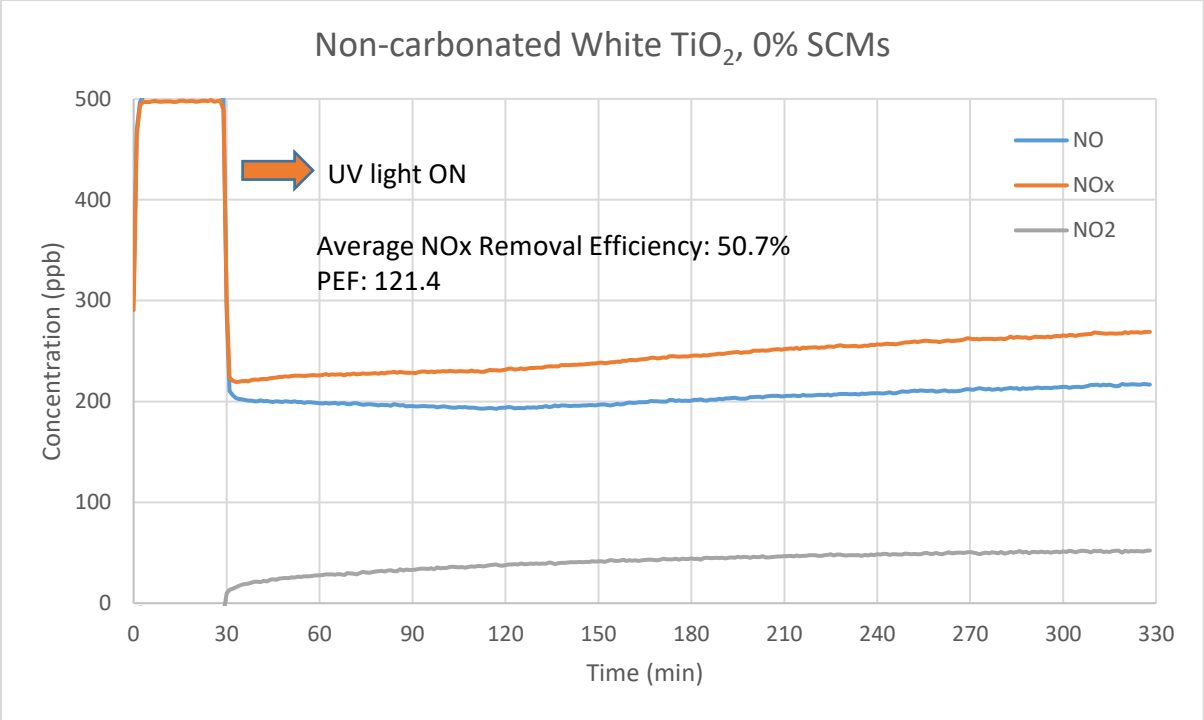

Figure 3-6 Non-carbonated White TiO_2, 0% SCMs test result

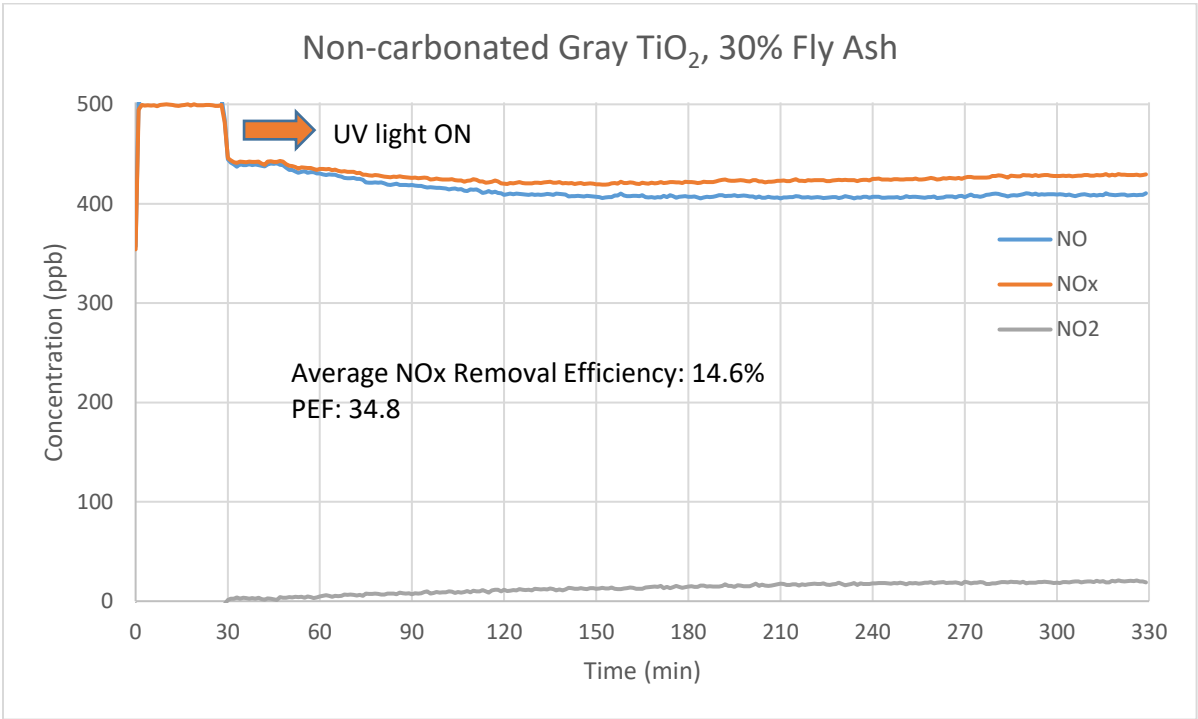

Figure 3-7 Non-carbonated Gray TiO_2, 30% Fly Ash test result

3.4.1.2. NOx Removal Results

Results of all photoreactor tests for NOx removal are shown in Table 3.2, which lists the PEF and NOx removal efficiency calculated for each specimen in the test matrix. The final column in Table 3.2 lists the decline in PEF found for each mix design because of carbonation. PEF and NO_x removal efficiency values for each case were averaged from two specimens except for a few cases where three specimens were tested. Sample variability is discussed further in in Section 3.4.1.3. Both carbonated and non-carbonated control mixes with Plain Type I cement (no TiO_2) effectively showed no NOx removal, validating that the observed NOx removal was caused by the introduction of TiO_2 into the cementitious matrix.

Table 3-2 NOx removal results

Mix Design	Carbonation	PEF ($\mu mol/m^2 \cdot hr$)	NOx Removal (%)	Decline in PEF Due to Carbonation (%)
White TiO_2, 0% SCMs	Non-carbonated	112.3	48.1	74.6
	Carbonated	28.6	12.3	
White TiO_2, 15% Fly Ash	Non-carbonated	111.7	49.2	31.5
	Carbonated	76.5	33.0	
White TiO_2, 30% Fly Ash	Non-carbonated	54.4	23.7	13.2
	Carbonated	47.2	19.8	
White TiO_2, 5% Silica Fume	Non-carbonated	117.6	51.2	84.4
	Carbonated	18.4	7.9	
Gray TiO_2, 0% SCMs	Non-carbonated	45.1	19.4	64.9
	Carbonated	15.9	6.8	
Gray TiO_2, 15% Fly Ash	Non-carbonated	37.1	15.6	46.2
	Carbonated	20.0	8.3	
Gray TiO_2, 30% Fly Ash	Non-carbonated	39.7	16.7	62.2
	Carbonated	15.0	6.0	
Gray TiO_2, 5% Silica Fume	Non-carbonated	41.8	17.3	78.1
	Carbonated	9.2	3.8	
2.5% Anatase, 0% SCMs	Non-carbonated	63.5	26.7	70.3
	Carbonated	18.9	7.8	
5% Anatase, 0% SCMs	Non-carbonated	50.4	21.5	23.9
	Carbonated	38.4	16.3	
10% Anatase, 0 % SCMs	Non-carbonated	55.9	23.4	—
	Carbonated	77.1	31.6	
5% Anatase, 15% Fly Ash	Non-carbonated	78.4	31.3	44.9
	Carbonated	43.2	18.6	
5% Anatase, 30% Fly Ash	Non-carbonated	84.8	36.3	60.6
	Carbonated	33.5	14.8	
5% Anatase, 5% Silica Fume	Non-carbonated	54.9	23.8	63.3
	Carbonated	20.2	8.9	

Plain Type I	Non-carbonated	2.8	1.1	—
	Carbonated	-0.5	-0.2	

3.4.1.3. Specimen Variability

As mentioned in Section 3.3.1.1, all NOx removal results were calculated from an average of two specimens, except for three cases where three specimens were tested (Carbonated White TiO_2, 30% Fly Ash; Non-carbonated Gray TiO_2, 0% SCMs; Non-carbonated 5% Anatase, 30% Fly Ash). To demonstrate variability between samples, results from each individual specimen that was tested in the photoreactor are shown in Table 3.3. For cases where three specimens were tested, the coefficient of variation (%) was also calculated.

Table 3-3 Specimen variation in NOx removal test

Mix Design	Carbonation	PEF ($\mu mol/m^2 \cdot hr$)				
		Specimen 1	Specimen 2	Specimen 3	Average	COV (%)
White TiO_2, 0% SCMs	Non-carbonated	103.1	121.4		112.3	
	Carbonated	29.2	27.9		28.6	
White TiO_2, 15% Fly Ash	Non-carbonated	112.4	110.9		111.7	
	Carbonated	71.9	81.1		76.5	
White TiO_2, 30% Fly Ash	Non-carbonated	53.1	55.6		54.4	
	Carbonated	36.8	44.4	60.3	47.2	20.8
White TiO_2, 5% Silica Fume	Non-carbonated	115.9	119.3		117.6	
	Carbonated	21.3	15.4		18.4	
Gray TiO_2, 0% SCMs	Non-carbonated	56.9	48.0	30.5	45.1	24.3
	Carbonated	13.9	17.8		15.9	
Gray TiO_2, 15% Fly Ash	Non-carbonated	45.7	28.4		37.1	
	Carbonated	18.8	21.1		20.0	
Gray TiO_2, 30% Fly Ash	Non-carbonated	34.8	44.5		39.7	
	Carbonated	14.1	15.9		15.0	
Gray TiO_2, 5% Silica Fume	Non-carbonated	49.2	34.3		41.8	
	Carbonated	12.7	5.6		9.2	
2.5% Anatase, 0% SCMs	Non-carbonated	58.4	68.5		63.5	
	Carbonated	19.2	18.5		18.9	
	Non-carbonated	53.4	47.4		50.4	

5% Anatase, 0% SCMs	Carbonated	40.5	36.2		38.4	
10% Anatase, 0 % SCMs	Non-carbonated	56.3	55.4		55.9	
	Carbonated	81.5	72.7		77.1	
5% Anatase, 15% Fly Ash	Non-carbonated	78.9	77.8		78.4	
	Carbonated	37.1	49.2		43.2	
5% Anatase, 30% Fly Ash	Non-carbonated	82.3	78.4	93.8	84.8	7.7
	Carbonated	38.2	28.7		33.5	
5% Anatase, 5% Silica Fume	Non-carbonated	46.7	63.0		54.9	
	Carbonated	19.7	20.6		20.2	

As seen in Table 3.3, in some cases there was significant variability in PEF values between specimens with the same mix design and carbonation condition. Coefficient of variation (COV) values of 20.8% and 24.3% were calculated for the Carbonated White TiO_2, 30% Fly Ash and Non-carbonated Gray TiO_2, 0% SCM specimens, respectively. These COV seem high but are in similar ranges to other concrete properties such as flexural strength, free drying shrinkage and fracture parameters. Overall for this type of test and specimen preparation, in many of the cases PEF values were within a few $\mu mol/m^2 \cdot hr$, and the coefficient of variation for the three 5% Anatase, 30% Fly Ash specimens was just 7.7%.

3.4.2. Photospectrometer Testing

3.4.2.1. Typical Test Result

A typical reflectance spectrum obtained from spectrophotometer testing is demonstrated in Figure 3.8. The spectral reflectance (total amount of monochromatic radiation reflected back from test sample surface as a percentage of incident monochromatic radiation) is plotted as a function of wavelength. The UV-A spectrum ($315\ nm \leq \lambda \leq 400\ nm$) is highlighted by a red box. The irradiance of the solar spectrum is also plotted in Figure 3.8 to indicate the relative weights of various parts of the spectrum used to calculate albedo.

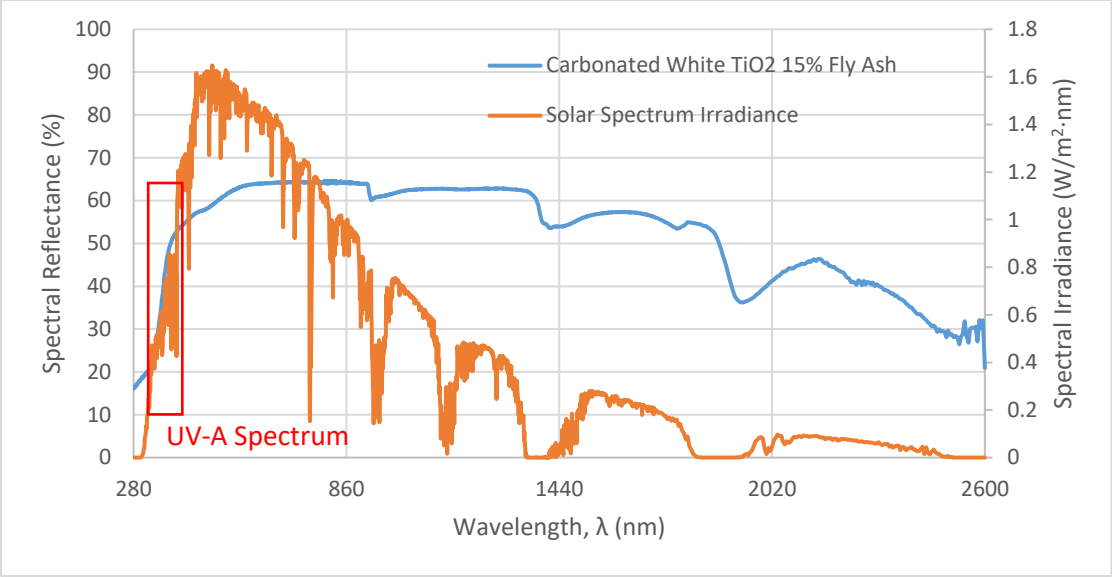

Figure 3-8 Typical reflectance spectrum for a photocatalytic mortar specimen. UV-A wavelengths are indicated by the red box

3.4.2.2. Albedo and UV-A Reflectance

Albedo and UV-A reflectance results calculated from photospectrometer testing are shown in Table 3.4. Values for each case are averages of measurements taken on two sides of single mortar specimens.

Table 3-4 Albedo and UV-A reflectance results

Mix Design	Carbonation	Albedo	UV-A Reflectance
White TiO_2, 0% SCMs	Non-carbonated	0.67	0.39
	Carbonated	0.62	0.37
White TiO_2, 15% Fly Ash	Non-carbonated	0.62	0.42
	Carbonated	0.56	0.34
White TiO_2, 30% Fly Ash	Non-carbonated	0.49	0.32
	Carbonated	0.53	0.34
White TiO_2, 5% Silica Fume	Non-carbonated	0.47	0.43
	Carbonated	0.43	0.31
Gray TiO_2, 0% SCMs	Non-carbonated	0.39	0.30
	Carbonated	0.30	0.19
Gray TiO_2, 15% Fly Ash	Non-carbonated	0.41	0.33
	Carbonated	0.36	0.25
Gray TiO_2, 30% Fly Ash	Non-carbonated	0.45	0.32
	Carbonated	0.31	0.19
Gray TiO_2, 5% Silica Fume	Non-carbonated	0.31	0.25
	Carbonated	0.24	0.20
2.5% Anatase, 0% SCMs	Non-carbonated	0.42	0.35
	Carbonated	0.32	0.23
5% Anatase, 0% SCMs	Non-carbonated	0.31	0.22
	Carbonated	0.33	0.23
10% Anatase, 0 % SCMs	Non-carbonated	0.35	0.22
	Carbonated	0.38	0.23
5% Anatase, 15% Fly Ash	Non-carbonated	0.42	0.30
	Carbonated	0.38	0.25
5% Anatase, 30% Fly Ash	Non-carbonated	0.40	0.29
	Carbonated	0.32	0.18
5% Anatase, 5% Silica Fume	Non-carbonated	0.38	0.31
	Carbonated	0.30	0.23

Plain Type I	Non-carbonated	0.37	0.32
	Carbonated	0.40	0.37

3.4.3. Artificial Carbonation

As seen in Table 3.2, nearly every mortar specimen exhibited a decline in photocatalytic efficiency after it was artificially carbonated. The results of the phenolphthalein treatment confirmed that carbonation had occurred on these specimens. Side-by-side images of the surface and interior of non-carbonated and carbonated White TiO_2 specimens are shown in Figures 3.9 and 3.10. The uniform purple color of the non-carbonated surface in Figure 3.9 demonstrates that carbonation has not occurred, while the absence of purple on the surface of the carbonated specimen demonstrates that the surface is carbonated. In Figure 3.10, the interior of the non-carbonated specimen is a uniform deep purple, again signifying a lack of carbonation. In the interior of the carbonated specimen, a carbonation front (located by a dashed line in Figure 3.10(b)) has progressed a few mm into the specimen. Near the edges, which were exposed to the environment, the mortar is white in color, while the center of the specimen remains purple as the interior is not yet fully-carbonated. Just inside the carbonation front indicated by the dashed line, the purple color is fading, showing the progression of carbonation deeper into the specimen.

Figure 3-9 Side-by-side image of surfaces of non-carbonated (left) and carbonated (right) White TiO_2, 0% SCM mortar specimens after treatment with phenolphthalein

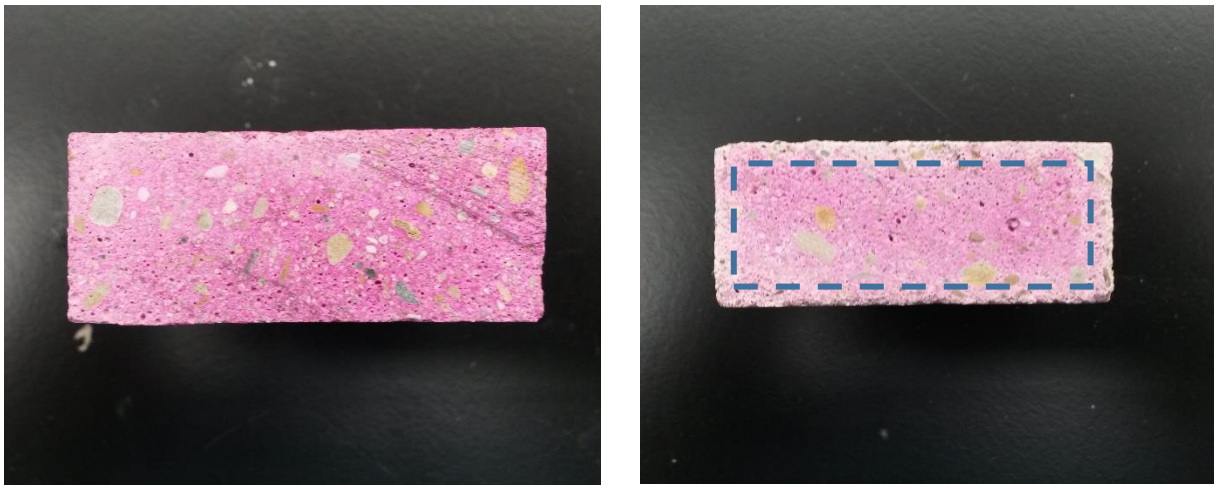

(a) (b)

Figure 3-10 Interior fracture surfaces of (a) non-carbonated and (b) carbonated White TiO_2, 0% SCM mortar specimens after treatment with phenolphthalein. The dashed line in Figure (b) indicates approximate location of carbonation front

For specimens containing fly ash, carbonation did not appear to occur to the same extent as in specimens without. In Figures 3.11 and 3.12, which show non-carbonated and carbonated White TiO_2 specimens with 30% fly ash, both specimens were very similar in appearance after treatment with phenolphthalein. The purple color on the surface of the carbonated specimen in Figure 3.11 may be a lighter shade than on the non-carbonated specimen, indicating partial carbonation of the surface, but the interiors of both specimens in Figure 3.12 are uniformly purple, indicating little to no carbonation depth.

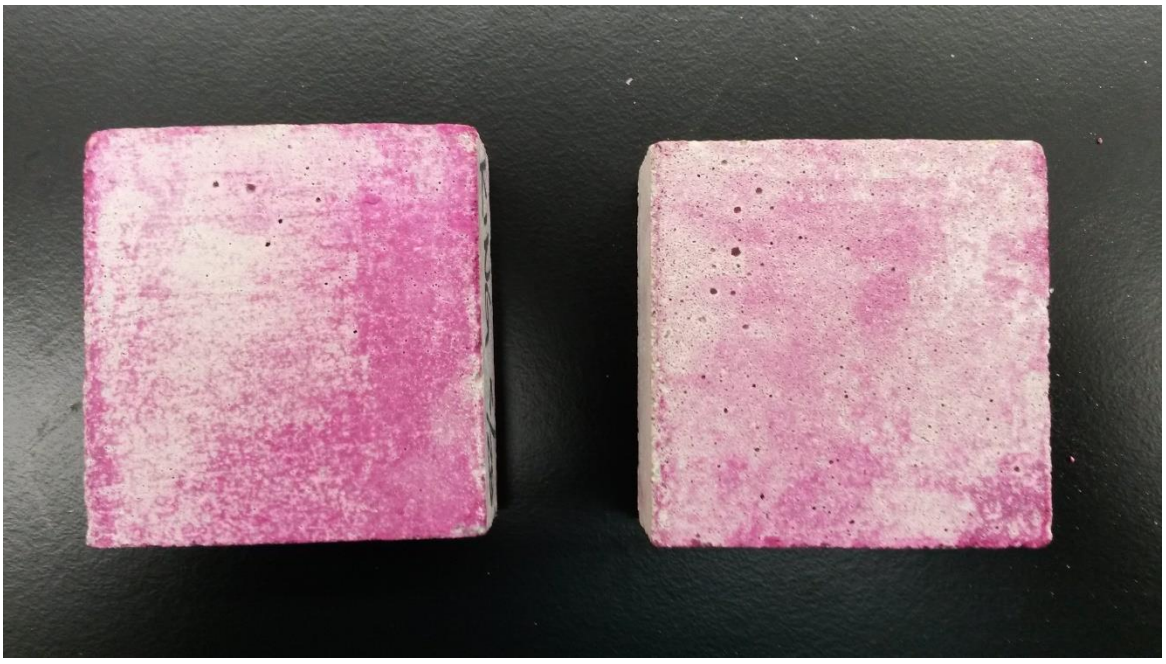

Figure 3-11 Side-by-side image of surfaces of non-carbonated (left) and carbonated (right) White TiO_2, 30% Fly Ash mortar specimens after treatment with phenolphthalein

Figure 3-12 Side-by-side image of interior of interior fracture surfaces of non-carbonated (left) and carbonated (right) White TiO_2, 30% Fly Ash mortar specimens after treatment with phenolphthalein

3.5. DISCUSSION OF RESULTS

3.5.1. Photocatalytic Performance

3.5.1.1. Comparison of Laboratory Results to Literature

The photocatalytic performance of the mortar specimens in this experiment fell within the broad range of values that have been reported in the literature. Table 3.5 compares results from laboratory experiments that tested similar specimens to those in this study (in this case, gray cement, 0% SCMs, non-carbonated). As demonstrated in the table, a very wide range of results have been reported, resulting primarily from the sensitivity of the laboratory experiment to changes in test conditions.

Table 3-5 Comparison to results in literature for samples with gray cement

Researcher	Photocatalytic Efficiency ($\mu mol/m^2 \cdot hr$)	Testing Conditions
Current study	45.1-63.5	$[NO]_{in}$ = 500ppb, 50% RH, 1 Lpm, 10 W/m^2, 0.40 w/c, 3 day curing
Chen and Poon (2009)	80-130	$[NO]_{in}$ = 1000 ppb, 30% RH, 3 Lpm, 0.6 W/m^2, 0.35 w/c, 3-28 day curing
Sikkema (2013)	100.8	$[NO]_{in}$ = 1000 ppb, 50% RH, 3 LPM, 10 W/m^2, 0.40 w/c, 14 day curing
Lee *et al.* (2014)	21.6-31.5	$[NO]_{in}$ = 1000 ppb, 50% RH, 0.5 Lpm, 10 W/m^2, 0.4-0.6 w/c, 28 day curing

Poon and Guo (2015)	125	$[NO]_{in}$ = 1000 ppb, 30% RH, 3 Lpm, 2 W/m^2, 0.4 w/c, 1 day curing
Jayapalan *et al.* (2015)	8-22	$[NO]_{in}$ = 500 ppb, 50% RH, 1 Lpm, 10 W/m^2, 0.5 w/c, 14 day curing

Examining and comparing the test conditions of this experiment to those in the literature, it is possible to understand why the photocatalytic efficiency measured in this experiment differs from other tests and verify that these results are reasonable. For example, it is well-demonstrated (Ballari et al. 2010, Boonen and Beeldens 2013, Sikkema 2013) that testing at a lower relative humidity significantly enhances photocatalytic efficiency. Therefore, it makes sense that a test performed at 50% RH (such as in this experiment) would produce a lower PEF value than the tests performed at 30% RH listed in Table 3.5.

Another major factor is inlet concentration. At a higher inlet concentration (e.g. 1000 ppb vs. 500 ppb), assuming the reaction proceeds at a similar efficiency, a greater amount of NOx will be removed simply because there is a greater amount of NOx present in the photoreactor system. Another factor is UV irradiance. When other factors are equal, greater levels of photocatalytic performance occur under higher UV irradiance. Finally, curing also has a significant impact on photocatalytic performance (Chen and Poon 2009). With a longer curing time, photocatalytic performance is diminished. Therefore, a test in which the samples were cured at 28 days would not be expected to produce a PEF value as high as a sample tested at 3 days, such as in this experiment. Overall, the PEF values obtained in this experiment appear to be reasonable relative to the literature and selected test parameters.

3.5.1.2. Mix Trends

Trends in photocatalytic performance related to the addition of SCMs, carbonation and albedo/UV-A reflectance, which factored most prominently into the results, will be discussed in detail in sections 3.5.2 and 3.5.3. The effects of microstructural properties on photocatalytic performance are also explored in Chapter 4.

Outside of those factors, one of the most interesting findings in the study was that increasing the TiO_2 content of the Anatase samples did not appear to correspond to an increase photocatalytic efficiency. Among the non-carbonated Anatase mixes without SCMs, the 2.5% TiO_2 by mass specimens achieved a higher PEF than samples containing 5% and 10% TiO_2, and the PEF values were all within a similar range (50.4-63.5 μmol/m^2·hr). These findings would suggest that increasing TiO_2 content of the mix beyond 2.5% may not have a significant effect on PEF, which is consistent with the findings of Diamanti *et al.* (2013) and Lucas *et al.* (2013). However, this finding does not mean that there is no correlation between TiO_2 content and photocatalytic efficiency. In fact, PEF consistently declined in non-carbonated White and Gray TiO_2 specimens where fly ash replaced the commercial TiO_2 cement blend (unknown TiO_2 content) by 15-30%. Instead, the results imply that there may be an upper limit to the amount of TiO_2 that contributes to NOx removal.

Ironically, a consistent increase in PEF as a function of increasing TiO_2 content was observed in the carbonated Anatase specimens. This finding may seem to contradict the results obtained for the non-carbonated Anatase specimens, however, it just suggests that increasing TiO_2 content

provides some resilience against the effects of carbonation, which is discussed later in Section 3.5.2.3.

3.5.1.3. Projection of Laboratory Results to Field Performance

Since photocatalytic efficiency is sensitive to changes in test conditions and results in the literature are variable, it can be difficult to assess the overall effectiveness of the photocatalytic mixes tested in this (or any) experiment and to project effectiveness in the field. The NOx removal capability measured by laboratory testing in the current study and in the literature is an order of magnitude lower than the total NOx emissions by motor vehicles in the United States (Sikkema 2013). However, much of these NOx emissions quickly dissipate into the atmosphere, leaving a lower but still-harmful concentration of NOx that lingers in urban areas and especially the near-road environment. In the context of near-road NOx concentrations, the values obtained in this experiment are promising.

Consider one study of a polluted near-road environment performed by Berkowicz (2000) in Berlin. Peak hourly NOx concentrations at that site measured as high 300 ppb, which, depending on the ratio of NO to NO_2, would approach the US EPA limit for NO_2 of 100 ppb. This NOx concentration corresponds to roughly 13 $\mu mol/m^3$ (depending on the assumed NO to NO_2 ratio). The most reactive, non-carbonated mix design tested in this experiment (TiO_2 White, 5% SF) demonstrated the ability to remove over 117 μmol of NOx per square meter of surface area per hour. Based on these results, a photocatalytic FFC pavement at the Berlin site would theoretically be able to react with all NOx present in a volume of air extending from the surface up to a height of 9 m over each square meter of pavement surface. Although NOx particles present 9 m over the surface of the pavement may not ultimately interact with the pavement surface, the point illustrates the significant NOx-removal capabilities of the photocatalytic concrete. Even the least reactive, carbonated mix design tested in this experiment (TiO_2 Gray, 5% SF) was able to remove just over 9 $\mu mol/m^2 \cdot hr$ of NOx in the laboratory, enough to theoretically remove all of the NOx present up to a height of nearly 1 m above the surface in one hour.

Field testing is required to fully understand the extent of the interaction between NOx and the pavement surface in the near-road environment as well as factors such as wind and turbulence. Likewise, laboratory testing showed that the reaction does not proceed at 100% efficiency, which would also be the case in the field. Nevertheless, the results of this experiment are particularly promising because they were obtained at a more realistic relative humidity and were even effective after accelerated carbonation, which significantly reduced the PEF. Overall the collected data supports the idea that there is potential impact of photocatalytic FFC inlays on the urban environment in terms of reducing harmful emissions to human health.

3.5.2. Effect of Surface Carbonation on Photocatalytic Performance

3.5.2.1. Overall Decline in Photocatalytic Efficiency

The results of the photoreactor testing showed that artificial carbonation led to a sharp decline in photocatalytic efficiency. The average decrease in PEF observed across all of the photocatalytic test samples was 55.2%. Further, when considering mixes that did not contain fly ash (which was intended to reduce carbonation), the average decrease in PEF grows to 65.6%. A plot of PEF values obtained for carbonated and non-carbonated samples is shown in Figure 3.13 to visualize the disparity. Each pair of bars corresponds to non-carbonated and carbonated PEF measured for one mix (i.e. White TiO_2, 0% SCMs).

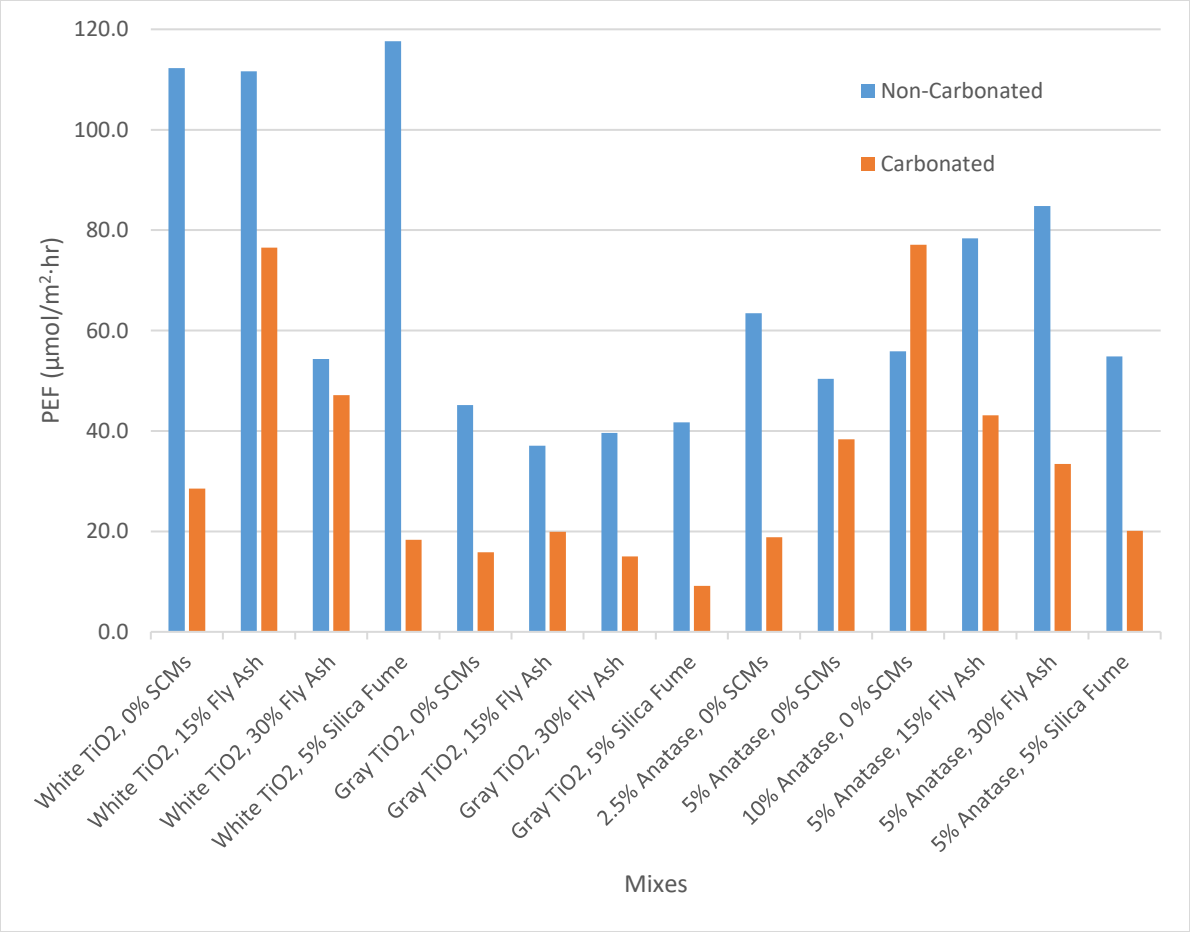

Figure 3-13 Decline in PEF because of carbonation

This carbonation-related decline was notably worse than those previously observed in the laboratory by Chen and Poon (2009) and Diamanti *et al.* (2013), who measured decreases of roughly 30% and 25% in photocatalytic efficiency, respectively. The larger impact from carbonation found in this study may result from testing the molded sample surface or differences in specimen curing times between this study and previous reseachers.

These findings may have large implications on the viability of photocatalytic mix designs in which TiO_2 is mixed into the concrete mass, as carbonation is inevitable in the presence of atmospheric CO_2. The possible causes of the decline in photocatalytic performance because of carbonation related to the microstructure are explored in Chapter 4. Additionally, in section

3.5.3.3, the possibility that carbonation reduces the reflectance of concrete, which in turn decreases the photocatalytic efficiency, is investigated.

3.5.2.2. Mitigation with Addition of Fly Ash

As previously discussed, fly ash and silica fume were added to the photocatalytic mixes to reduce the amount of carbonation. Through pozzolonic reactions with calcium hydroxide in the microstructure, the addition of fly ash and silica fume would hopefully consume a portion of the available of CH, resulting in less carbonation of the sample surface and thus less interference with photocatalytic activity. Treatment with phenolphthalein (Figures 3.11 and 3.12) confirmed that the addition of fly ash slowed carbonation of the mortar samples, and based on the results listed in Table 3.2, in most cases appeared to mitigate the carbonation-related decline in photocatalytic efficiency. On the other hand, silica fume did not appear to have any impact on carbonation or its effects on photocatalytic performance. There were several issues including usage of condensed (agglomerated) silica fume, dispersing during mixing, and/or not enough curing time was provided to allow full reaction of the silica fume particles with CH.

Before analyzing the data in greater detail it must be noted that several of the mix parameters studied in this experiment (SCM content, carbonation state, reflectance) vary from sample-to-sample, and in the case of reflectance could not be strictly controlled. Therefore, it can be hard to determine the exact impact of each individual property because they have competing effects on PEF. As previously mentioned, carbonation may reduce reflectance, which in turn may reduce photocatalytic efficiency. (The relationships between PEF, carbonation, and UV-A relflectance/albedo are discussed in more detail in section 3.5.3). By breaking the data into smaller subsets of mixes, the benefits of adding fly ash alone can be studied more clearly.

The benefit to adding fly ash was most clearly observed with the White TiO_2 specimens. PEF results are re-stated in Table 3.6 for convenience. As seen in the table, the mix containing 0% fly ash exhibited a nearly 75% decline in PEF because of carbonation. Meanwhile, PEF for the 15% and 30% fly ash mixes declined by just 31.5% and 13.2%, respectively, exhibiting a clear correlation between and increase in fly ash content and mitigation of the impact of carbonation on PEF.

Table 3-6 Carbonation and PEF for White TiO_2 mixes

Mix Design	Carbonation	PEF ($\mu mol/m^2 \cdot hr$)	NOx Removal (%)	Decline in PEF Due to Carbonation (%)
White TiO_2, 0% SCMs	Non-carbonated	112.3	48.1	74.6
	Carbonated	28.6	12.3	
White TiO_2, 15% Fly Ash	Non-carbonated	111.7	49.2	31.5
	Carbonated	76.5	33.0	
White TiO_2, 30% Fly Ash	Non-carbonated	54.4	23.7	13.2
	Carbonated	47.2	19.8	

This effect was also observed for the Gray TiO_2 specimens, as seen in Table 3.7. The decline caused by carbonation was reduced from 64.9% to 46.2% by adding 15% fly ash to the Gray TiO_2 specimens. There was some inconsistency, as the carbonation-related decline in PEF for the 30% fly ash mix jumped back up to 62.2%. However, considering that the 30% fly ash mix contains 30% less TiO_2 by mass than the 0% SCM mix (as the fly ash is replacing the commercial TiO_2 cement blend), the 30% fly ash specimen can still be considered to be relatively more effective in the face of carbonation.

Table 3-7 Carbonation and PEF for Gray TiO_2 mixes

Mix Design	Carbonation	PEF ($\mu mol/m^2 \cdot hr$)	NOx Removal (%)	Decline in PEF Due to Carbonation (%)
TX Gray, 0% SCMs	Non-carbonated	45.1	19.4	64.9
	Carbonated	15.9	6.8	
TX Gray, 15% Fly Ash	Non-carbonated	37.1	15.6	46.2
	Carbonated	20.0	8.3	
TX Gray, 30% Fly Ash	Non-carbonated	39.7	16.7	62.2
	Carbonated	15.0	6.0	

The carbonation-fly ash trend in PEF for the Anatase mixes differed from the trends with White and Gray TiO_2 mixes. As seen in Table 3.8, the percent decline because of carbonation actually increases as a function of increasing fly ash content. However, this disparity appears to be caused by a disproportionate impact of carbonation on the UV-A reflectance of the mixes containing fly ash, which has also been included in Table 3.8. Both the 15% and 30% fly ash mixes experienced steep declines in UV-A reflectance with carbonation. Therefore, in this case the reflectance may be the primary factor driving the percent decline in photocatalytic efficiency. Even given the larger percent decline, the carbonated 15% fly ash sample still had a higher raw PEF value than the carbonated 0% fly ash sample. (The PEF for the carbonated 30% fly ash mix was lowest, but still close to the 0% mix.)

Table 3-8 Carbonation and PEF for Anatase mixes

Mix Design	Carbonation	PEF ($\mu mol/m^2 \cdot hr$)	NOx Removal (%)	Decline in PEF Due to Carbonation (%)	UV-A Reflectance
5% Anatase, 0% SCMs	Non-carbonated	50.4	21.5	23.9	0.22
	Carbonated	38.4	16.3		0.23
5% Anatase, 15% Fly Ash	Non-carbonated	78.4	31.3	44.9	0.29
	Carbonated	43.2	18.6		0.18
5% Anatase, 30% Fly Ash	Non-carbonated	84.8	36.3	60.6	0.31
	Carbonated	33.5	14.8		0.23

3.5.2.3. Effect of TiO_2 Content

One mix (10% Anatase, 0% SCMs) surprisingly demonstrated an increase in PEF with carbonation (77.1 vs. 55.9 $\mu mol/m^2 \cdot hr$ for carbonated and non-carbonated, respectively). It is highly unlikely that carbonation is responsible for the increase in PEF in this case given how strongly carbonation correlates with a decline in photocatalytic efficiency for every other mix considered in this study. More likely, the increase may have been caused by an increase in variability associated with creating mixes at a higher TiO_2 content.

This result does fit the trend observed with the other Anatase specimens with varying TiO_2 content and no SCMs. The percent decline in PEF due to carbonation is typical for the 2.5% TiO_2 mix (70.3%), but drops significantly for the 5% TiO_2 mix (23.5%) before the aforementioned increase in the 10% mix. This finding would suggest that increasing TiO_2 content may also help mitigate the detrimental effects of surface carbonation. Given that increasing TiO_2 content from 2.5% to 10% did not increase photocatalytic efficiency in non-carbonated samples, one explanation for this phenomenon may be that TiO_2 nanoparticles that are otherwise not contributing in carbonation-free conditions are able to help preserve the photocatalytic ability of the mortar mixes when carbonation starts to inhibit their overall activity.

3.5.3. Effect of UV-A Reflectance/Albedo on Photocatalytic Performance

3.5.3.1. Correlation with Photocatalytic Efficiency

Based on the results of the photoreactor testing in Table 3.2, the non-carbonated White TiO_2 mixes tended to exhibit a significantly greater NOx removal ability than the Gray TiO_2 and Anatase mixes, and the primary differences measured between the mixes made with white and gray cements were their reflectance properties. As shown in Table 3.4, albedo and UV-A reflectance were found to be substantially higher for the White TiO_2 specimens compared to the others. On average, albedo and UV-A reflectance were roughly 35% higher and 24% higher, respectively, for non-carbonated white cement samples compared to corresponding gray cement samples with the same SCM content. Therefore, the disparity in reflectance and PEF for white and gray samples suggested a correlation between PEF and reflectance for all samples.

Figure 3.14 plots PEF vs. UV-A reflectance for all non-carbonated TiO_2-containing specimens in the test matrix. The data markers in Figure 3.14 distinguish between specimens made with white cement and gray cement (both conventional Type I and commercial), but the trendline and R^2 values displayed in the figure apply to the entire data set.

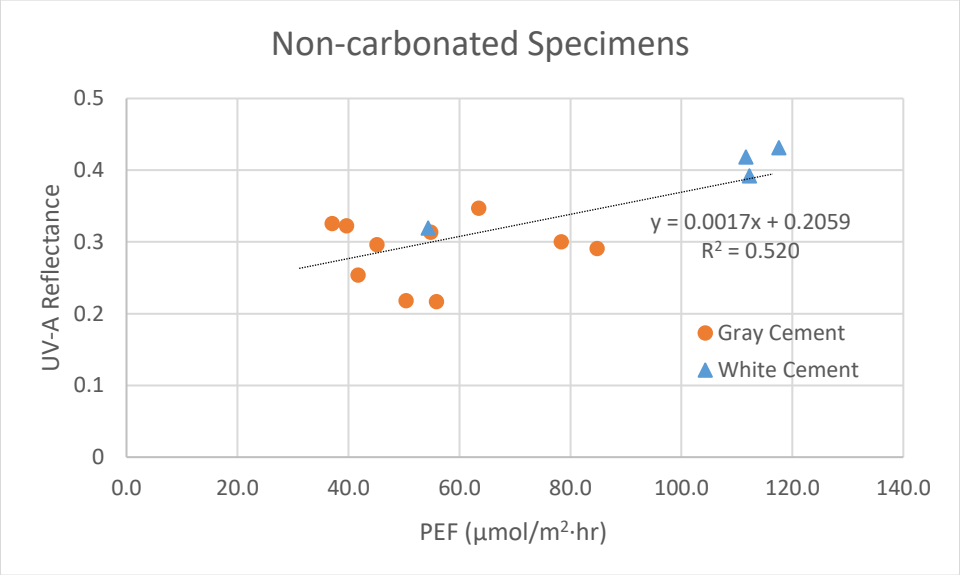

Figure 3-14 PEF vs. UV-A reflectance for all non-carbonated specimens

The relationship between reflectance and PEF is most obvious when considering white vs. gray cement. Compared to the Gray TiO_2 mixes with corresponding SCM contents PEF for the White TiO_2 specimens was on average 142% higher, and these differences are obvious looking at the plot in Figure 3.14. However, when considering the entire test matrix, the data is a little more scattered (R^2 = 0.520). Although not the strongest relationship overall, it still indicates a meaningful correlation, especially considering the other competing factors that may be affecting photocatalytic efficiency. For example, the White TiO_2 specimen containing 30% fly ash had a corresponding reduction of 30% in TiO_2 content, so it is important to remember that TiO_2 content is a possible competing factor affecting the plot.

Because TiO_2 content does not change in the Anatase specimens upon addition of SCMs, those mixes offer a good opportunity for further investigation of the impact of reflectance on photocatalytic efficiency. As seen from the results of the spectrophotometer testing in Table 3.4, adding fly ash to mixes containing gray cement increased albedo relative to mixes that did not contain SCMs. And, when analyzing the Anatase mixes, it can be seen that this increase in albedo leads to a significant increase in PEF as well. UV-A reflectance vs. PEF for the Anatase samples with 0% SCMs, 15% fly ash, and 30% fly ash is plotted in Figure 3.15, which demonstrates a correlation between reflectance and PEF.

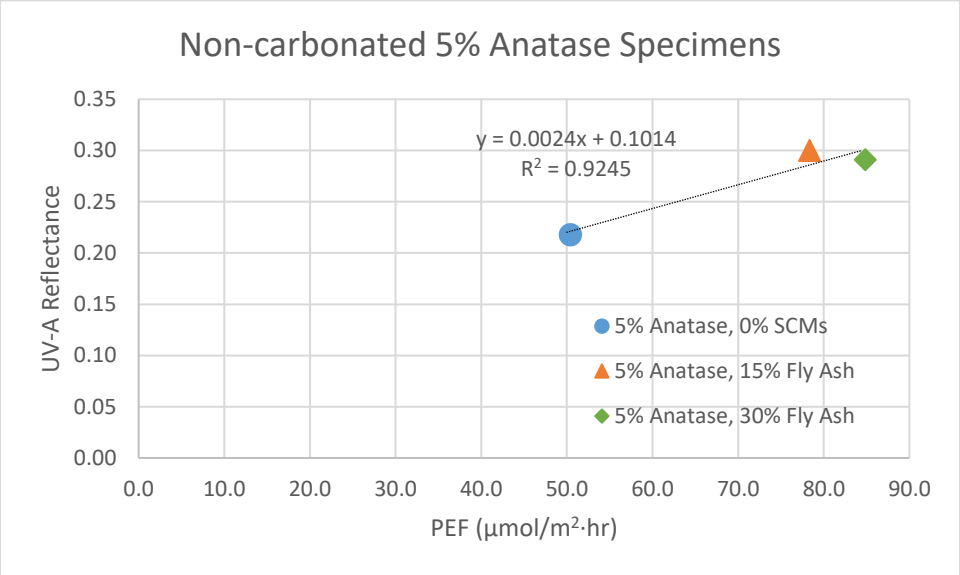

Figure 3-15 PEF vs. UV-A reflectance for Non-carbonated 5% Anatase specimens

There was no clear correlation observed between reflectance and photocatalytic efficiency for the carbonated specimens. The relationship between PEF and UV-A reflectance for carbonated specimens is plotted in Figure 3.16. Despite the reflectance of the White TiO_2 mixes remaining significantly higher than those of the Gray TiO_2 and Anatase mixes, the PEF values obtained from the White TiO_2 mixes are not consistently higher. No meaningful trends were observed across the entire carbonated data set ($R^2 = 0.142$) nor across any subsets of the data.

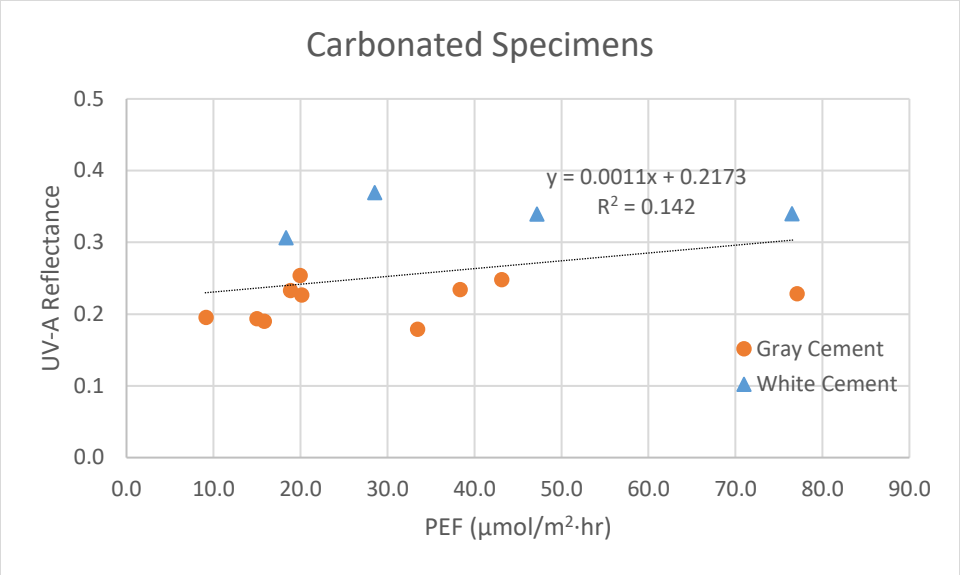

Figure 3-16 PEF vs. UV-A reflectance for all carbonated specimens

The lack of correlation between reflectance and PEF for carbonated specimens was primarily caused by the differences observed in the fly ash mixes. As discussed in Section 3.5.2.2, the introduction of fly ash altered the chemistry of the microstructure and altered the extent of surface carbonation in those specimens. TiO_2 content also appeared to play a role in photocatalytic performance post-carbonation. Therefore, the overall trend between reflectance and PEF broke down after carbonation, with the best-performing specimens demonstrating a balance between preferred SCM content, TiO_2 content, and reflectance characteristics.

Tables fully summarizing the correlation between PEF and UV-A reflectance as well as albedo, including the correlation coefficient, are included for non-carbonated specimens in Table 3.9 and for carbonated specimens in Table 3.10.

Table 3-9 Correlation between PEF and UV-A reflectance, albedo for non-carbonated specimens

Mix Design	Carbonation	PEF ($\mu mol/m^2 \cdot hr$)	Albedo	UV-A Reflectance
TX White, 0% SCMs	Non-carbonated	112.3	0.67	0.39
TX White, 15% Fly Ash	Non-carbonated	111.7	0.62	0.42
TX White, 30% Fly Ash	Non-carbonated	54.4	0.49	0.32
TX White, 5% Silica Fume	Non-carbonated	117.6	0.47	0.43
TX Gray, 0% SCMs	Non-carbonated	45.1	0.39	0.30
TX Gray, 15% Fly Ash	Non-carbonated	37.1	0.41	0.33
TX Gray, 30% Fly Ash	Non-carbonated	39.7	0.45	0.32
TX Gray, 5% Silica Fume	Non-carbonated	41.8	0.31	0.25
2.5% Anatase, 0% SCMs	Non-carbonated	63.5	0.42	0.35
5% Anatase, 0% SCMs	Non-carbonated	50.4	0.31	0.22
10% Anatase, 0 % SCMs	Non-carbonated	55.9	0.35	0.22
5% Anatase, 15% Fly Ash	Non-carbonated	78.4	0.42	0.30
5% Anatase, 30% Fly Ash	Non-carbonated	84.8	0.40	0.29
5% Anatase, 5% Silica Fume	Non-carbonated	54.9	0.38	0.31
Correlation with PEF (r-value)			0.72	0.72

Table 3-10 Correlation between PEF and UV-A reflectance, albedo for carbonated specimens

Mix Design	Carbonation	PEF ($\mu mol/m^2 \cdot hr$)	Albedo	UV-A Reflectance
TX White, 0% SCMs	Carbonated	28.6	0.62	0.37
TX White, 15% Fly Ash	Carbonated	76.5	0.56	0.34
TX White, 30% Fly Ash	Carbonated	47.2	0.53	0.34
TX White, 5% Silica Fume	Carbonated	18.4	0.43	0.31
TX Gray, 0% SCMs	Carbonated	15.9	0.30	0.19
TX Gray, 15% Fly Ash	Carbonated	20.0	0.36	0.25
TX Gray, 30% Fly Ash	Carbonated	15.0	0.31	0.19
TX Gray, 5% Silica Fume	Carbonated	9.2	0.24	0.20
2.5% Anatase, 0% SCMs	Carbonated	18.9	0.32	0.23

5% Anatase, 0% SCMs	Carbonated	38.4	0.33	0.23
10% Anatase, 0 % SCMs	Carbonated	77.1	0.38	0.23
5% Anatase, 15% Fly Ash	Carbonated	43.2	0.38	0.25
5% Anatase, 30% Fly Ash	Carbonated	33.5	0.32	0.18
5% Anatase, 5% Silica Fume	Carbonated	20.2	0.30	0.23
Correlation with PEF (r-value)			0.51	0.38

3.5.3.2. Proposed Mechanism

The reflectance of the mortar samples had an impact on photocatalytic efficiency because of the phenomenon of diffuse reflection. Concrete (as well as mortar and paste), with its porous microstructure and rough surface finish, is an example of a diffuse surface (van Ginneken *et al.* 1998). Instead of reflecting back at the incident angle, light incident on diffuse surfaces is reflected with equal intensity in all directions in the half space around the surface (Siegel and Howell 2002). Figure 3.17 demonstrates the effect of diffuse reflection on the photocatalytic surface. Since the UV-A radiation is scattered in all directions, instead of just reflecting back out into the atmosphere, more radiation remains within the near-surface region through primary and secondary scattering and is able to reach TiO_2 sites that may have otherwise needed direct incident light to be activated. Therefore, the cumulative impact of diffuse reflection is to enhance photocatalytic activity, and the more reflective a photocatalytic surface is in the UV-A spectrum, the better it will be able to react with and remove NOx from the environment.

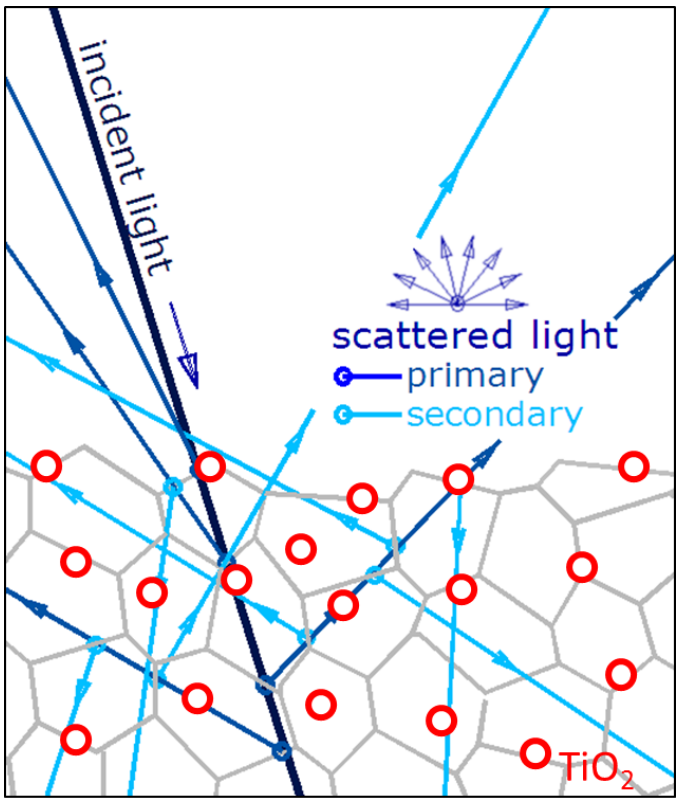

Figure 3-17 Demonstration of diffuse reflection at photocatalytic concrete surface (adapted from Wikipedia 2015)

UV-A radiation is the catalyst of the photocatalytic reaction between NOx and TiO_2, so it is appropriate to focus primarily on the relationship between UV-A reflectance and photocatalytic performance. It should also be noted, however, that UV-A reflectance and albedo correlate very closely for all specimens tested in this experiment (r-value of 0.99), and that, as seen in Table 3.9, the correlation between albedo and PEF for non-carbonated samples was identical to that between UV-A reflectance and PEF. While distinguishing albedo from UV-A reflectance may be trivial when analyzing data obtained from a spectrophotometer, albedo is easier to measure in the field and is a more common representation of reflectance in general. Therefore, it is valid and potentially more useful to point out that albedo correlates strongly with photocatalytic efficiency as well.

3.5.3.3. Relationship with Carbonation

A topic that had gone relatively unexplored in the literature is the effect of carbonation on reflectance of the mortar specimens. Figures 3.18 and 3.19 plot albedo and UV-A reflectance, respectively, for carbonated vs. non-carbonated specimens for each mix. A line of unity is drawn in both figures to help illustrate if any effect was observed.

From the plots in Figures 3.18 and 3.19, it appears that carbonation influenced the albedo and UV-A reflectance. On average, albedo declined by 0.05 (11.9%) when mixes were carbonated, while UV-A reflectance declined by 0.06 (19.4%). As seen in the figures, a few mixes did not demonstrate declines in either property (White TiO_2, 30% Fly Ash; 5% Anatase, 0% SCMs; 10% Anatase, 0% SCMs). However, these absolute differences were small (0.01-0.02), and given the

consistency and magnitude of the decreases in other samples, they were likely outlying cases caused by sample variation.

The evidence that carbonation decreased the reflectance of the photocatalytic specimens may help explain why carbonation also decreased photocatalytic efficiency as well as its impact on decreasing surface porosity. Given the strength of the correlation between albedo/UV-A reflectance and PEF, any decline in the reflectance caused by carbonation would in turn lead to a decline in PEF. Further, this behavior may be related to the two primary theories in the literature behind why carbonation affects photocatalytic performance. Whether the $CaCO_3$ byproduct filled in the capillary pores and decreased the surface area of the microstructure or blinded the TiO_2 nanoparticles as it precipitated on the surface, it is possible that either of these mechanisms may also cause a drop in the diffuse reflectance of the near-surface region. Thus, each of these proposed mechanisms may combine to play a role in reducing photocatalytic performance. The effects of carbonation on the microstructure are investigated more thoroughly in Chapter 4.

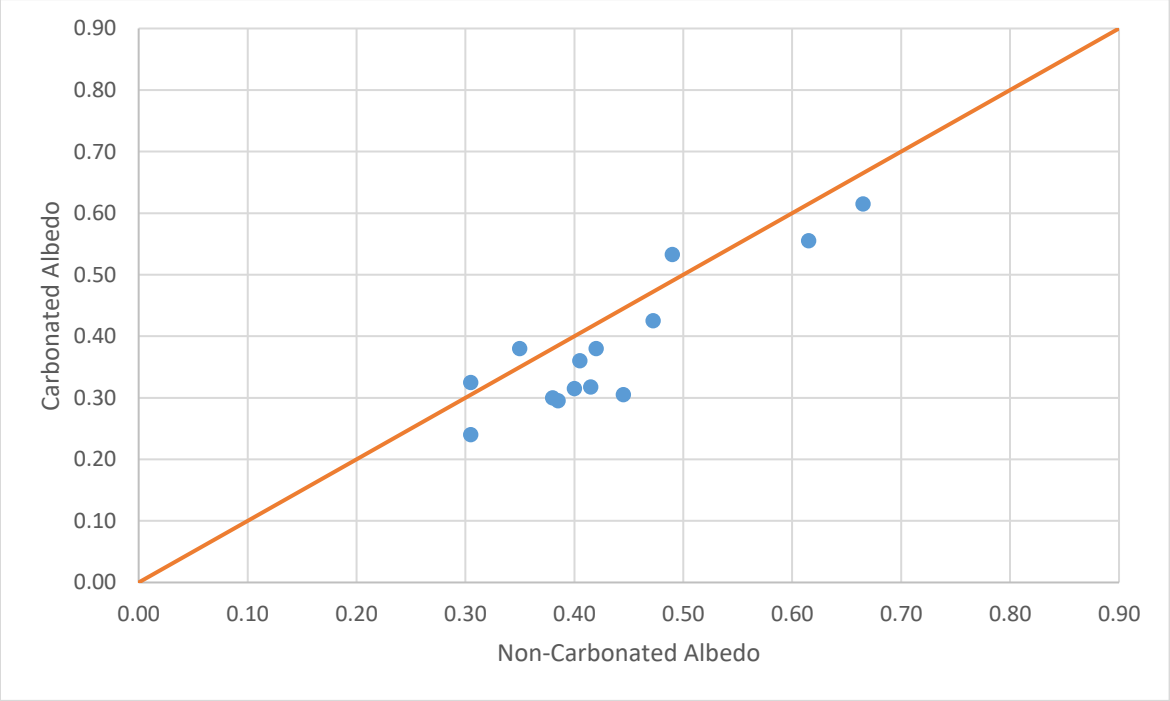

Figure 3-18 Comparison of albedo between non-carbonated and carbonated specimens for each mix design

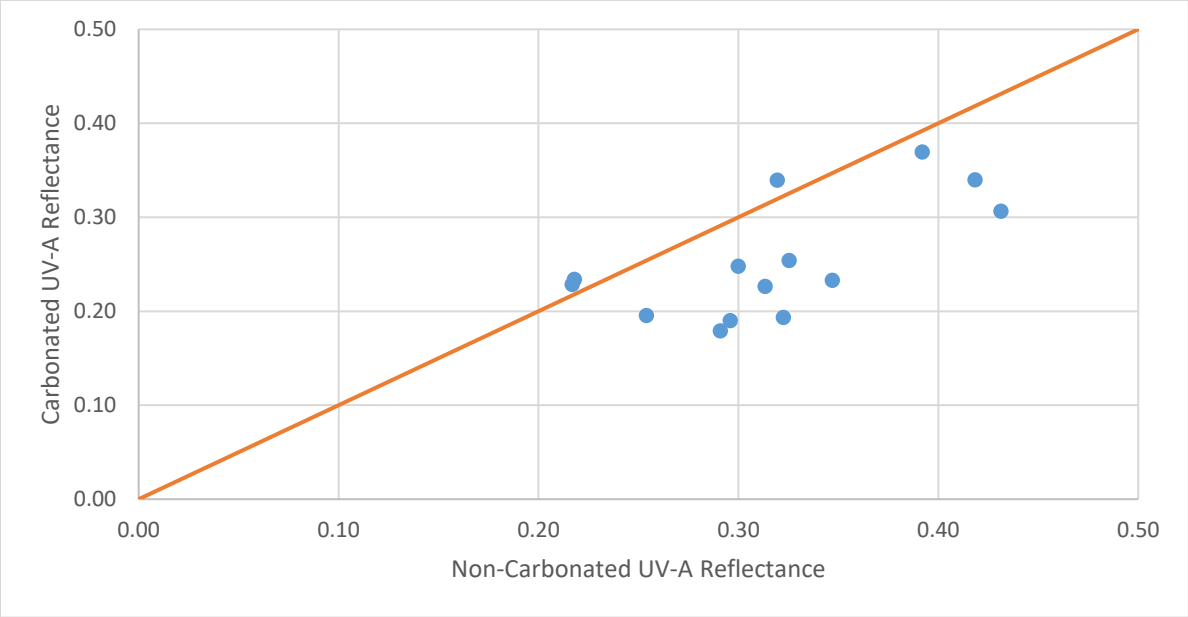

Figure 3-19 Comparison of UV-A reflectance between non-carbonated and carbonated specimens for each mix design

3.6. CONCLUSIONS

The potential environmental benefits of thin, multi-functional flowable fibrous concrete (FFC) inlays were examined through laboratory photoreactor testing to determine NOx removal ability. FFC mixtures were prepared with varying characteristics, including cement type, TiO_2 content, and addition of supplementary cementitious materials, to determine their impact on photocatalytic performance under varying conditions, including artificial carbonation. Spectrophotometer testing was also performed to analyze the spectral reflectance of the FFC specimens to characterize the relationship between reflectance and NOx removal ability.

The overall photocatalytic performance of the FFC specimens in this experiment was satisfactory and consistent with previous research performed on mixes with similar characteristics, demonstrating the NOx-removal potential of thin photocatalytic FFC inlays. However, artificial carbonation was found to severely curtail the magnitude of photocatalytic performance, to an even greater extent than in previous studies. These results highlight the need to identify methods to mitigate the impact of carbonation on photocatalytic concrete, since long-term exposure to carbon dioxide is unavoidable for pavement applications.

The two most important properties observed to correlate with photocatalytic performance were fly ash content and reflectance. Although the effects of these two parameters on photocatalytic efficiency interfered with each other when looking at the entire population of mixes in the study, and were affected differently by carbonation, analysis of smaller subsets of data allowed for a clearer view of their impacts.

The addition of fly ash appeared to be an effective method for partial mitigation of the negative impact of carbonation on photocatalytic efficiency. The observed correlation was strongest in the White TiO_2 mixes, where increasing the fly ash replacement of cement up to 30% helped offset the decline in PEF caused by carbonation. For other samples, competing effects of carbonation

and substitution rate may have diluted the impact of fly ash. The addition of silica fume did not appear to successfully mitigate carbonation or otherwise impact performance but these conclusions are based on 3 day cured samples with condensed silica fume.

Enhanced reflectance, measured by both UV-A reflectance and albedo, correlated with greater photocatalytic efficiency. This trend was especially evident when comparing mixes made with white and gray cement. White cement samples were much more reflective than gray cement samples, and in turn demonstrated significantly greater NOx removal ability before carbonation. Photocatalytic performance also appeared to be sensitive to changes in reflectance driven by the addition of supplementary cementitious materials to the mix. The phenomenon of diffuse reflectance at the surface of the concrete drove the relationship between reflectance and photocatalytic efficiency.

For specimens in which TiO_2 content was varied, evidence suggested that there may be an upper limit around 2.5% TiO_2 by mass after which increasing TiO_2 content did not lead to further gains in photocatalytic efficiency. However, after artificial carbonation, specimens with TiO_2 contents as high as 10% appeared to be more resilient in maintaining NOx removal ability compared to specimens at lower TiO_2 contents, suggesting that a higher TiO_2 content may help mitigate carbonation as well.

Through quantifying the impact of different mix characteristics on photocatalytic performance, the results of this study can be used to optimize an FFC (or any type of photocatalytic concrete) mix design for NOx removal. Based on the mixes used in this investigation, a concrete made from a commercial white photocatalytic cement blend with 15% fly ash replacement would prove most effective by combining a high reflectance with resilience to carbonation.

Further mitigation of the impact of carbonation could also be achieved if it were practical or economical to increase the amount of TiO_2 in the cement blend to offset the fly ash replacement and/or further increase TiO_2 content. The NOx removal ability of this mix design, as well as the others considered in this study, demonstrated the potential to make a positive impact on the near-road environment and reduce the harmful impacts of NOx emissions.

CHAPTER 4-MICROSTRUCTURAL ANALYSIS OF PHOTOCATALYTIC CEMENT PASTE

4.1. INTRODUCTION

The surface reactions and bulk material properties of photocatalytic concrete and mortar and their effects on NOx removal efficiency have been reported in the literature and previous chapters. To better understand the behavior of TiO_2-containing concrete, it is advantageous to characterize the microstructure of the cementitious matrix. By quantifying the microstructural features and observing their relationship with photocatalytic performance, a better understanding may be ascertained of the surface and mixture properties of photocatalytic cement and the factors that are most important in their ability to react with NOx.

One of the most commonly-used tools for microstructural analysis of cementitious materials is scanning electron microscopy (SEM). Through interactions between the electron beam and the sample surface, images may be taken at high magnifications with a very fine resolution. The contrast in these SEM micrographs may be related to either the topography or composition of the sample, allowing for identification and measurement of different phases and properties in the microstructure of cement paste. Another technique that often accompanies SEM is energy-dispersive x-ray spectroscopy (EDS). In EDS analysis, characteristic x-rays produced by interactions between electrons and the specimen are detected and used to analyze the elemental composition of the material.

In this study, the microstructure of TiO_2-containing cement paste was analyzed to investigate the relationship between microstructural properties and photocatalytic performance. SEM and EDS were used to characterize the microstructural morphology of the photocatalytic cement paste, including the locations and relative dispersion of the TiO_2 nanoparticles. Backscatter micrographs from the SEM were analyzed to measure microstructural properties, including porosity and estimated pore size, to determine if these properties impact photocatalytic efficiency. Porosity was also related to carbonation and the addition of supplementary cementitious materials. The anticipated results should facilitate understanding of the performance of photocatalytic cement and provide insight into the most advantageous cementitious characteristics to promote NOx removal ability.

4.2. LITERATURE REVIEW

4.2.1. Microstructural Analysis of Cement Paste

The microstructure of cement paste consists of the various phases, such as calcium silicate hydrate (C-S-H), calcium hydroxide (CH), and the capillary pore structure, that develop during

the hydration of Portland cement. Virtually every physical characteristic of concrete, including strength, elastic modulus, permeability, and shrinkage, is influenced by the properties of the microstructure. Because of its very small scale, microscopy is well-suited to microstructural investigation, and scanning electron microscopy and related techniques have proved especially useful.

4.2.1.1. Scanning Electron Microscopy and Backscatter Electron Imaging

Scanning electron microscopy (SEM) allows for observation of materials at very high magnifications using an electron microscope. Samples are placed under vacuum inside the microscope and an incident electron beam is focused onto the specimen surface. Interaction between the beam and surface results in elastic and inelastic scattering of electrons within a teardrop-shaped, three-dimensional interaction volume, producing secondary and backscattered electrons, respectively. The intensity of the ejected electrons depends on the composition (backscattered) and topography (secondary and backscattered) of the sample. Topographic and/or compositional images of the material may be formed by scanning the beam progressively farther down across the specimen surface to create a raster. Properties of the electron beam such as current (via accelerating voltage) and diameter (via spot size) can be adjusted to control the brightness, resolution, and contrast of the image, and the instrument lenses control magnification.

Backscatter electron imaging (BEI) is primarily used to characterize the microstructural morphology (phase composition) of cement paste. The intensity of backscattered electrons is governed by the backscatter coefficient (η). Backscatter coefficent is a unique material property that depends on atomic number (Z). For flat, polished samples, η may be estimated for a given phase according to Equation 4.1 (Goldstein *et al.* 1992). For mixtures, η may be calculated by weighting the η values of the individual components based on their relative mass concentrations.

$$\eta = -0.0254 + 0.016Z - 1.86 \times 10^{-4}Z^2 + 8.3 \times 10^{-7}Z^3 \quad (4.1)$$

Backscattered electrons produced by materials with a higher backscatter coefficient are detected with greater intensity, causing them to appear brighter (i.e. more white) in the image. This phenomenon is the basis of compositional contrast between phases in BEI micrographs. Flat, polished samples must be used when performing compositional analysis during BEI, as topography also influences the intensity of backscattered electrons and can alter the image.

Finally, BEI may also be used to measure the porosity of cement paste. In a BEI micrograph, capillary pores appear as black voids. (Gel pores are too small to be resolved by SEM, and are ignored.) These voids contrast significantly with the rest of the cementitious matrix, which appears in white and gray. If the exact threshold in brightness (0-256) between pores and hydration products in the image is known, image processing can be used to segment the pores from the rest of the image, allowing for calculation of two-dimensional pore sizes and total porosity based on the size and number of pixels constituting a pore (Scrivener 2004). This image analysis technique is particularly useful because the most common technique for characterizing the porosity of cement paste, mercury intrusion porosimetry (MIP), has been shown to systematically underestimate the size of the pores by orders of magnitude (Diamond 2000).

4.2.1.2. Energy-Dispersive X-Ray Spectroscopy

Energy-dispersive X-ray spectroscopy (EDS) is used in conjunction with SEM to perform compositional analysis of materials. When the electron beam interacts with the sample surface, inelastic scattering causes the ejection of secondary electrons and the emission of characteristic X-rays. These characteristic x-rays have a unique energy and wavelength that correspond to the

element in the specimen from which the x-ray was emitted. An X-ray detector in the SEM measures the energy level of these x-rays and matches them to their corresponding element, allowing for qualitative and quantitative analysis to characterize the elemental composition of the sample surface (Goldstein *et al.* 1992).

4.2.1.3. Studies of Photocatalytic Cement Paste

Photocatalytic concrete has been studied using SEM by a few researchers in the literature. Notably, Lee (2012) studied the surface of photocatalytic cement paste samples before and after wet/dry cycling and NOx exposure to gain insight into the long-term durability of the material. Hassan *et al.* (2010) used SEM to study a concrete surface with a TiO_2-based coating, and to evaluate its durability under simulated weathering and abrasion. It is important to note that these studies both utilized secondary electron imaging (SEI) to observe topographical changes to sample surfaces, not backscatter imaging to determine microstructural morphology.

Several researchers have used EDS to characterize elemental composition on the surface of photocatalytic mortar or concrete samples. Diamanti *et al.* (2013) characterized a titanium profile within the interior of photocatalytic concrete to confirm the presence of the nanoparticles and observe variation as a function of the analysis area. Sikkema *et al.* (2012) used EDS to identify nitrate byproducts deposited on the surface of samples that had been previously exposed to NOx in a laboratory photoreactor. Hanson (2014) analyzed spatial Ti concentrations by performing a map scan on different photocatalytic concrete surface finishes as well as on carbonated concrete that had been exposed to the environment, reporting a 60% reduction in Ti at the surface. Hassan *et al.* (2010) observed a relative decrease in Ti peaks in the x-ray spectrum obtained for samples exposed to simulated weathering and abrasion.

Despite the number of studies in the literature performing EDS analysis on photocatalytic concrete, each of the studies cited here contain a major limitation: the samples were obtained either from unprepared sample surfaces or fracture surfaces. When performing EDS, X-ray detectors determine elemental composition based on the angle of incidence of the X-ray according to Bragg's Law (Goldstein *et al.* 1992). A rough, unprepared specimen surface will scatter X-rays in all directions and produce a weaker and ultimately different spectrum from that of a flat surface, leading to errors in the analysis (ASTM 2010). Thus, it is likely that these EDS results in the literature could be inaccurate, particularly those which make quantitative inferences.

4.2.2. Porosity

Porosity is one of the most important properties of the microstructure of hydrated cement paste. The size and extent of the pore structure affects nearly every aspect of concrete durability and performance. Porosity is controlled primarily by the ratio of water to cementitious materials (w/cm) and the extent of hydration. A higher w/cm results in a more porous microstructure, while increasing curing time to promote a greater degree of hydration and a lower porosity microstructure. With respect to photocatalytic concrete, studies by Nazari and Riahi (2011) and Zhang and Li (2011) showed that the presence of TiO_2 nanoparticles reduced porosity at a constant w/cm, although not significantly.

4.2.2.1. Effect on Photocatalytic Efficiency

The porosity of photocatalytic cement paste has also been linked by researchers to NOx removal efficiency. Using MIP to determine porosity and pore size, Chen and Poon (2009), Sugrañez *et al.* (2013) and Lucas *et al.* (2013) all reported that a more porous microstructure (produced by increasing w/cm) promoted a higher degree of photocatalytic efficiency. Lucas *et al.* (2013) also found that a higher incidence of nanopores (smaller pore sizes) decreased NOx removal ability. Larger capillary pores have been found to be best for photocatalytic performance.

These results in the literature infer that a more porous microstructure provides more opportunities for reactions between NOx and TiO_2. Following pore size estimations using MIP testing, Lee *et al.* (2014) used a nitrogen BET method to measure the surface area of photocatalytic cement paste samples at different w/cm ratios. The results showed that pastes that absorbed more nitrogen (higher surface area) also exhibited a greater NO binding rate, indicating a direct correlation between photocatalytic efficiency and surface area.

4.2.2.2. Relationship with Supplementary Cementitious Materials and Carbonation

Replacing some cement with supplementary cementitious materials (SCMs), such as fly ash and silica fume, may produce a less porous microstructure overall. Pozzolanic reactions between the SCMs and CH produce more C-S-H, helping reduce the size of the capillary pores, especially when using silica fume. However, since pozzolanic reactions are slower than hydration of Portland cement, sufficient curing of the concrete must be maintained to realize these effects.

Carbonation of CH in the microstructure may lead to a decrease in porosity as well, as $CaCO_3$ precipitation fills in the capillary pores. However, in general these effects are only realized in concrete samples that are thin or have a high initial porosity (Mindess *et al.* 2003). A helium porosimetry test on carbonated concrete by Claisse *et al.* (1999) suggested that, while porosity clearly decreases in carbonated concrete with a high w/cm and larger pore sizes, carbonation may not cause a significant difference in the permeability in a mix with a w/cm as low as 0.45.

4.3. EXPERIMENTAL METHODS

To study the microstructure, photocatalytic cement paste samples (excluding sand) were prepared in the laboratory using the same mixes (varying cement type and SCM additions) as in Chapter 3. After curing and (for some samples) carbonation, flat, polished SEM specimens were created by cutting a thin, square section of paste from just below the sample surface, impregnating in epoxy, and polishing. The specimens were examined under an electron microscope to take backscatter images and analyzed using EDS for a characterization of the hardened microstructure. The BEI micrographs and compositional scans and maps obtained from EDS were used to evaluate the phases and elements present in the sample, including the relative dispersion of TiO_2 nanoparticles, and to estimate porosity and median pore size. The procedures used for this testing are outlined in the sections below.

4.3.1. Sample Preparation

Photocatalytic cement paste mixes (w/cm of 0.40) were prepared according to the same procedure used for the preparation of mortar mixes in Chapter 3. The test matrix of specimens was also identical to Chapter 3: White TiO_2, Gray TiO_2, and hand-mixed Anatase with gray Type I cement with straight cement samples and cement replacements of 15% fly ash, 30% fly ash, and 5% silica fume, along with a control sample of plain Type I cement. After three days moist curing, specimens for each mix selected for carbonation were artificially carbonated under the same conditions (28 days at 5% CO_2, 22°C, 55 to 80% RH environment).

After curing and (when pertinent) carbonation of the cement paste specimens (100 mm x 50 mm x 20 mm thick), cross-sections of the sample were cut with a low-friction diamond saw to produce SEM specimens. The specimens measured roughly 20 mm x 20 mm in surface area and were cut as thin as the saw blade allowed. The specimens could not be taken directly from the surface of the paste blocks because they needed to be as flat as possible for successful epoxy impregnation, polishing, and analysis. Instead, care was taken to cut specimens from as shallow of a depth from the paste sample surface as possible to preserve the near-surface structure for analysis, particularly for carbonated samples to ensure the carbonated depth was picked up in the testing and analysis. However, the specimens could not be created directly from the exposed sample surface, and thus the requirements of SEM sample fabrication is a possible limitation of this study.

After cutting the SEM specimens, they were placed in a house vacuum desiccator (254 mm Hg) overnight. After initial desiccation, the specimens were placed in cylindrical molds and impregnated in a very low viscosity carbon-based epoxy cut with a small amount of toluene. This impregnation was performed in a higher vacuum chamber (762 mm Hg) to allow for full intrusion of epoxy into the pores. The epoxy was allowed to set in the molds for 24 hours in the open laboratory environment.

After setting, the epoxy-impregnated paste samples were removed from the molds and ground with silicon carbide (SiC) grit papers with successively smaller grit sizes (400, 600, 800, and 1200) and polished with diamond pastes containing successively finer particle sizes (4 μm, 1 μm, 0.25 μm). Polish quality and progress was checked under an optical microscope. A fully-polished sample is shown in Figure 4.1.

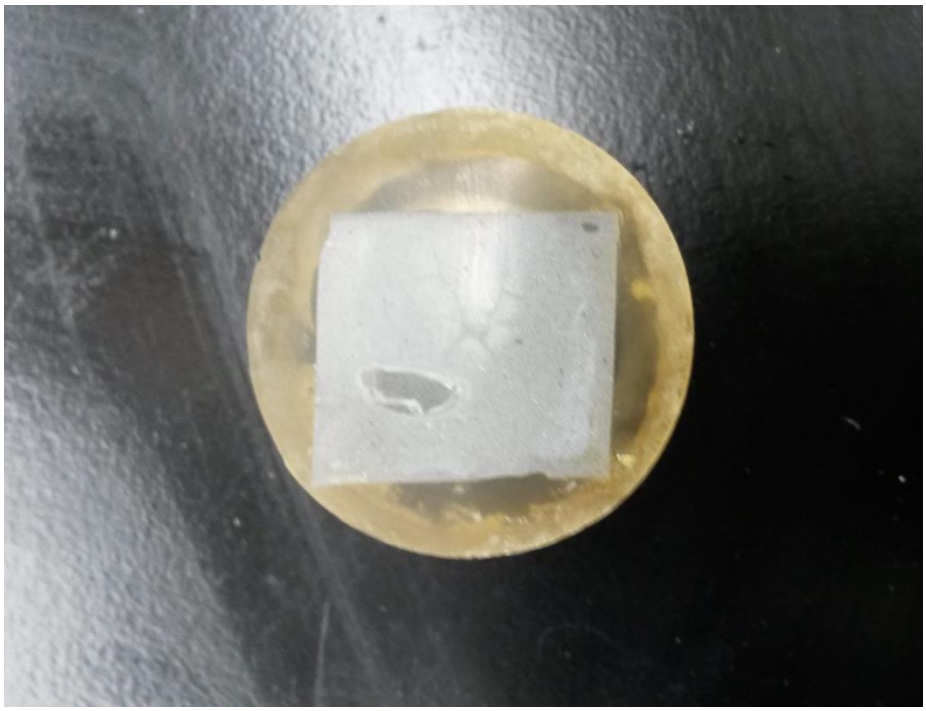

Figure 4-1 Epoxy-impregnated, polished photocatalytic cement paste sample

After polishing, the sides of the specimen were coated with graphite paint, and aluminum tape was applied to the sides to promote conductivity under the electron microscope. The specimen was returned to the house vacuum desiccator until SEM analysis. Finally, just before placing the sample into the microscope, it was sputter coated with a gold-palladium (Au-Pd) alloy to prevent charging.

4.3.2. Scanning Electron Microscopy and Backscatter Electron Imaging

4.3.2.1. Microscope Parameters and Methodology

A JEOL 6060 LV scanning electron microscope featuring a solid-state detector for BEI was used in this analysis. This study is believed to be the first time backscatter imaging was used to characterize photocatalytic cement paste. To produce high-quality BEI micrographs with sufficient resolution to observe the TiO_2 nanoparticles, the microscope was set to an accelerating voltage of 12 kV, spot size of 45 nm, and working distance of 10 mm. Images were taken at magnifications of 600x and 1200x. The phases observed in the micrographs were identified according to guides to BEI of cement paste written by Scrivener (2004) and Diamond (2004), which offer comprehensive descriptions and numerous visual examples of the appearance of common cement paste phases such as C-S-H and CH. Additional guidance in phase identification, especially in identifying TiO_2 nanoparticles, was predicted by the backscatter coefficient for phases based on relationships between Z and η described in Equation 1.

BEI micrographs were also used to determine the porosity of the mixes. Based on findings by Lange *et al.* (1994), a total of 15 micrographs were taken of each SEM specimen at 600x to make a reliable determination of the porosity of each mix design in the test matrix. The methodology for calculation of porosity is detailed in the following section.

4.3.2.2. Image Thresholding for Porosity Calculations

Given the contrast between the pores and the cementitious matrix in BEI micrographs, it may seem simple to separate (or segment) the capillary pores from the rest of the image. However, even at the minimum spatial resolution that can be achieved BEI, it can still be difficult to determining exactly where pores/voids end and hydration products begin. Wong *et al.* (2006) developed an objective method for segmenting the pores from the rest of the image to characterize porosity. The pore threshold was defined from the inflection point of the cumulative brightness histogram of the backscatter images, as shown in Figure 4.2. Any pixels with a brightness value less than the point at which the two tangent lines intersect are considered pores.

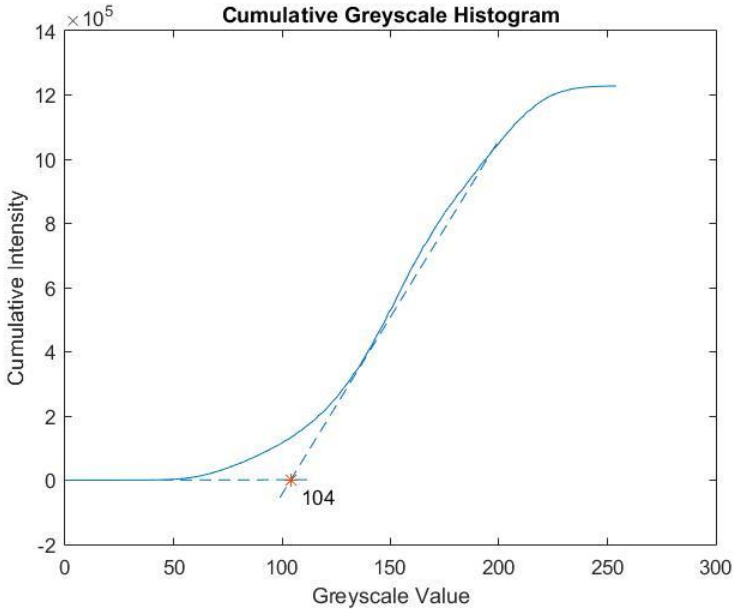

Figure 4-2 Example of cumulative greyscale histogram used for image thresholding

Using the technique described by Wong *et al.* (2006), MATLAB was used to develop a cumulative greyscale histogram for each BEI micrograph. After determining the pore threshold, the micrograph was converted to a binary image, as seen in Figure 4.3. During this step, to filter out noise in the data, at least seven pixels had to be connected to be counted as pores. From there, MATLAB was used to calculate the porosity of the paste in terms of a 2-D pore area fraction as well as median pore size based on the size of the pixels in the image.

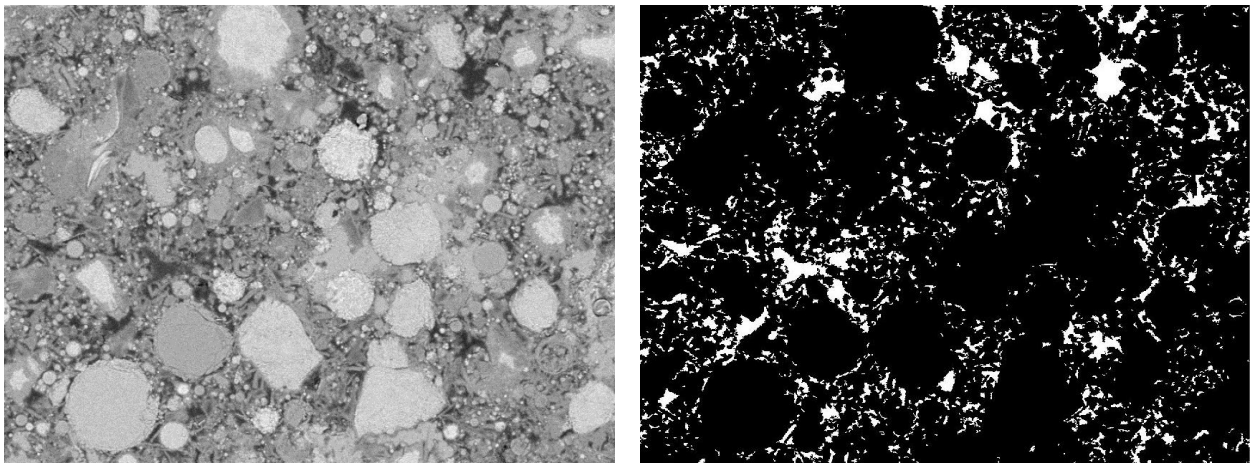

(a) (b)

Figure 4-3 Transformation of (a) a BEI micrograph to (b) a binary image where pores are indicated in white

4.3.3. Energy Dispersive X-Ray Spectroscopy

The JEOL 6060 LV SEM featured an x-ray detector for performing EDS analysis, and Iridium Ultra software was used for data collection and visual interpretation of EDS results. Microscope parameters were changed slightly to increase count rate to produce high-quality EDS scans. Accelerating voltage was raised to 15 kV and spot size was raised to 55 nm.

Two types of EDS scans were performed, line scans and map scans. During a line scan, the electron beam is repeatedly rastered in a straight line down the specimen surface. The energy of the detected x-rays is used to produce an elemental spectrum for the line being analyzed. Line scans also offer the ability to obtain spectra for individual elements as a function of distance along the scan. Line scans over the photocatalytic cement paste were used to obtain Ti spectra for positive identification of the TiO_2 nanoparticles in the microstructure.

A map scan obtains the x-ray spectrum encompassing the entire field of view in the SEM. In addition to producing a typical elemental spectrum, this data may also be used to produce 2-D spatial maps of the location of each element detected during the scan. Map scans of the paste specimens were used to locate TiO_2 nanoparticles within the microstructure and evaluate their relative dispersion. The map scans were also overlaid onto semi-transparent BEI micrographs, with the detected Ti presented in color, allowing for easy determination of the location of the nanoparticles in the microstructure.

Based on x-ray spectra obtained from a line or map scan, the relative abundance of the various elements in terms of weight percentage could be quantitatively calculated by the EDS software using an internal standard. However, using the software's internal standard with a material as complex as cement paste, which has numerous elements and phases, can lead to significant imprecision in the computations. Thus, quantitative analysis was not performed on the paste samples. Instead, the map scans obtained for each mix were analyzed to infer the TiO_2 content of the commercial mixes (White TiO_2, Gray TiO_2) by comparing the calculated Ti content to the hand-mixed Anatase mixes with known TiO_2 addition rates.

4.4. RESULTS

4.4.1. Backscatter Electron Imaging

4.4.1.1. Microstructural Analysis

Sample BEI micrographs of photocatalytic cement paste specimens, featuring labeling of some of the most prevalent phases, are shown in Figures 4.4 and 4.5 at magnifications of 600x and 1200x, respectively. Only a few examples of each phase are identified in the figures, i.e., a large number of unreacted cement grains are present in the micrograph in Figure 4.4, but only four are circled. Since C-S-H gel is the most abundant phase in cement paste and constitutes the vast majority of the groundmass (porous gray regions away from cement grains), only certain instances of C-S-H are labeled by stars in Figure 4.4 to distinguish them from surrounding phases. The color and morphology of C-S-H varies between multiple shades of gray because of its variable chemical composition (Scrivener 2004). C-S-H in the groundmass (outer product) tends to have a darker appearance, while C-S-H surrounding cement grains (inner product) has a lighter appearance. As previously discussed, the black void areas in Figures 4.4 and 4.5 correspond to pores.

The small white dots in the micrographs (easier to distinguish at the higher magnification in Figure 4.5, where they are labeled) appeared to fit the profile of the TiO_2 nanoparticles, small in size and bright in appearance. (Estimated η for TiO_2 is 0.184, similar to the bright white unreacted cement grains with estimated η of 0.174, and higher than any other phases present in cement paste.) EDS analysis (section 4.4.2) would confirm that these particles are indeed TiO_2 and assisted in evaluating their distribution throughout the microstructure. Typical Anatase TiO_2 particle sizes are on the order of 3-67 nm (Jiang *et al.* 2008), while a spot size of 45-55 nm was used in the SEM imaging, so the white dots themselves may represent either individual nanoparticles or small clusters.

4.4.1.2. Porosity and Pore Size Distribution

The porosity and median pore size calculated for each mix from the image thresholding are contained in Tables 4.1 and 4.2, respectively. Separate columns are provided for carbonated and non-carbonated specimens for easier analysis of the effects of carbonation.

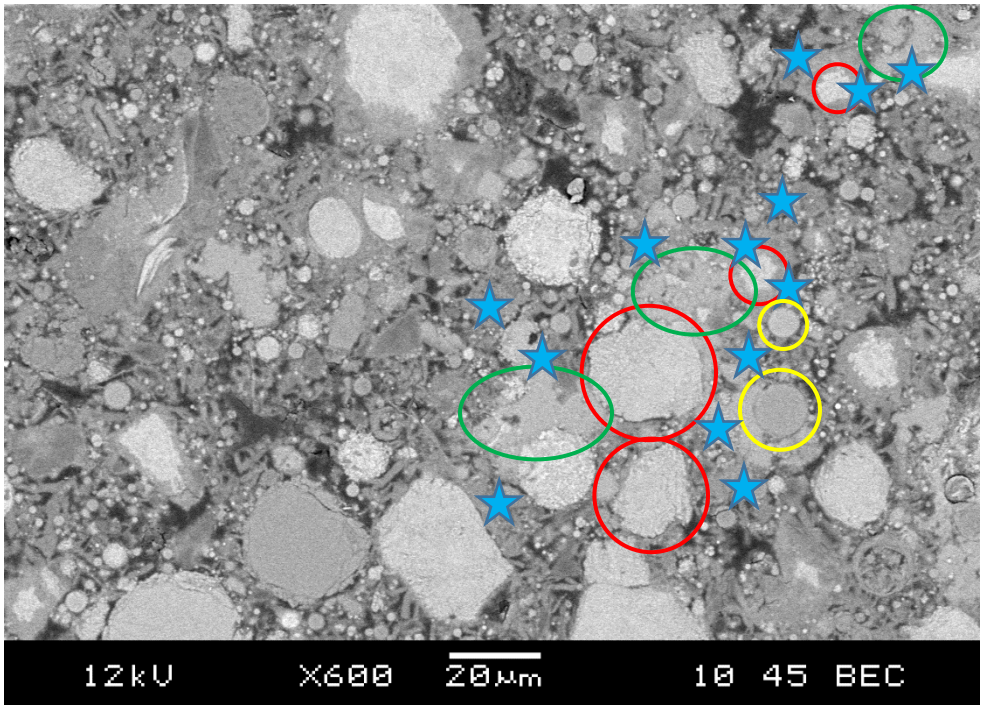

Figure 4-4 White TiO_2, 30% Fly Ash Micrograph with the following phases circled: unreacted cement grains (red), CH (green), and unreacted fly ash (yellow). C-S-H gel is prevalent throughout and marked by stars. Black void areas are pores

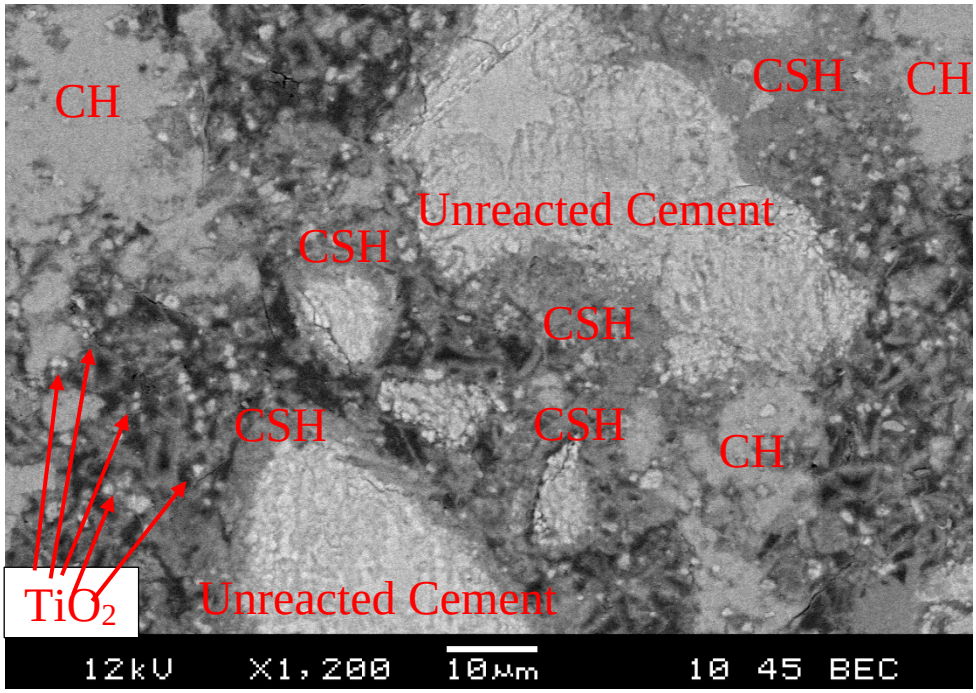

Figure 4-5 White TiO_2, 0% SCMs Micrograph with phases labeled

Table 4-1 Porosity results

Porosity (2-D Pore Area Fraction)			
Non-carbonated		Carbonated	
Plain Type I	0.121	Plain Type I	0.085
White TiO_2, 0% SCMs	0.184	White TiO_2, 0% SCMs	0.176
White TiO_2, 15% Fly Ash	0.173	White TiO_2, 15% Fly Ash	0.200
White TiO_2, 30% Fly Ash	0.135	White TiO_2, 30% Fly Ash	0.127
White TiO_2, 5% Silica Fume	0.198	White TiO_2, 5% Silica Fume	0.144
Gray TiO_2, 0% SCMs	0.112	Gray TiO_2, 0% SCMs	0.085
Gray TiO_2, 15% Fly Ash	0.163	Gray TiO_2, 15% Fly Ash	0.165
Gray TiO_2, 30% Fly Ash	0.135	Gray TiO_2, 30% Fly Ash	0.127
Gray TiO_2, 5% Silica Fume	0.141	Gray TiO_2, 5% Silica Fume	0.151
2.5% Anatase, 0% SCMs	0.084	2.5% Anatase, 0% SCMs	0.132
5% Anatase, 0% SCMs	0.123	5% Anatase, 0% SCMs	0.112
10% Anatase, 0% SCMs	0.142	10% Anatase, 0% SCMs	0.085
5% Anatase, 15% Fly Ash	0.096	5% Anatase, 15% Fly Ash	0.164
5% Anatase, 30% Fly Ash	0.107	5% Anatase, 30% Fly Ash	0.193
5% Anatase, 5% Silica Fume	0.077	5% Anatase, 5% Silica Fume	0.155

Table 4-2 Median pore size results

Median Pore Area (μm^2)			
Non-carbonated		Carbonated	
Plain Type I	0.502	Plain Type I	0.530
White TiO_2, 0% SCMs	0.530	White TiO_2, 0% SCMs	0.418
White TiO_2, 15% Fly Ash	0.948	White TiO_2, 15% Fly Ash	0.586
White TiO_2, 30% Fly Ash	0.641	White TiO_2, 30% Fly Ash	0.697
White TiO_2, 5% Silica Fume	0.363	White TiO_2, 5% Silica Fume	0.530
Gray TiO_2, 0% SCMs	0.335	Gray TiO_2, 0% SCMs	0.418
Gray TiO_2, 15% Fly Ash	1.090	Gray TiO_2, 15% Fly Ash	0.558
Gray TiO_2, 30% Fly Ash	0.723	Gray TiO_2, 30% Fly Ash	0.641
Gray TiO_2, 5% Silica Fume	0.363	Gray TiO_2, 5% Silica Fume	0.614

2.5% Anatase, 0% SCMs	0.335	2.5% Anatase, 0% SCMs	0.307
5% Anatase, 0% SCMs	0.446	5% Anatase, 0% SCMs	0.363
10% Anatase, 0% SCMs	0.488	10% Anatase, 0% SCMs	0.530
5% Anatase, 15% Fly Ash	0.390	5% Anatase, 15% Fly Ash	0.446
5% Anatase, 30% Fly Ash	0.558	5% Anatase, 30% Fly Ash	0.558
5% Anatase, 5% Silica Fume	0.279	5% Anatase, 5% Silica Fume	0.558

4.4.2. Energy Dispersive X-Ray Spectroscopy

A sample line scan obtained during EDS analysis is shown in Figure 4.6, with the analysis line and Ti spectrum overlaying a BEI micrograph. (The diminished image quality in Figure 4.6 compared to other BEI micrographs in this chapter is a result of changes to the microscope parameters to increase the precision of the EDS analysis.) Two map scans with Ti overlays (accompanied by the original BEI micrographs) of the same sample at magnifications of 600x and 1200x are shown in Figures 4.7 and 4.8, respectively. Finally, the full elemental spectrum for the map scan in Figure 4.8 is presented in Figure 4.9, with the element corresponding to each peak identified in the figure. Peaks that appear in Figure 4.9 but are not labeled correspond to gold and palladium from the sputter coat and carbon from the epoxy. The highest peaks belong to Ca (for which a second-order peak is also visible) and Si, which was expected because of the dominance of C-S-H and CH in the microstructure, followed by elements contained in the less prevalent phases and finally Ti.

The Ti peaks in Figure 4.6 and highlighted areas in Figures 4.7 and 4.8 confirm that the small, bright white particles in the BEI micrographs correspond to TiO_2 nanoparticles (or small clusters). The map scans also make it significantly easier to identify the location and dispersion of the nanoparticles relative to other microstructural features, especially at lower magnifications.

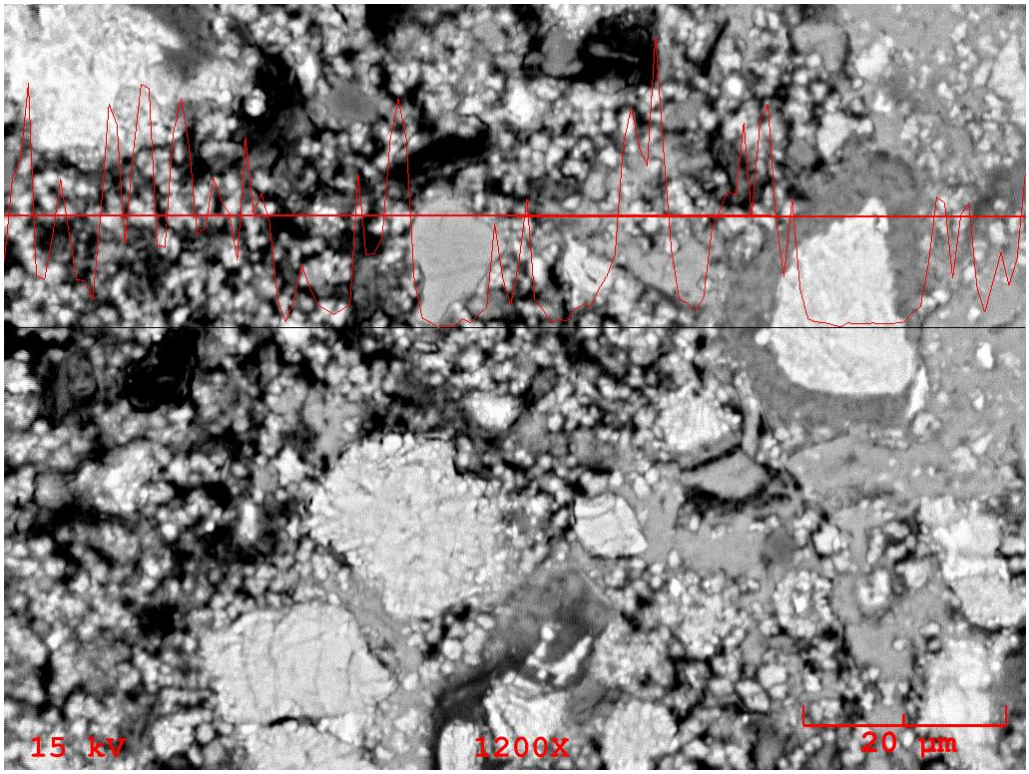

Figure 4-6 EDS line scan of 10% Anatase, 0% SCM sample plotted on top of the backscatter image. Red line indicates scan location. Spectral peaks (in red) correspond to Ti detected during scanning. Black line represents x-axis of the spectrum

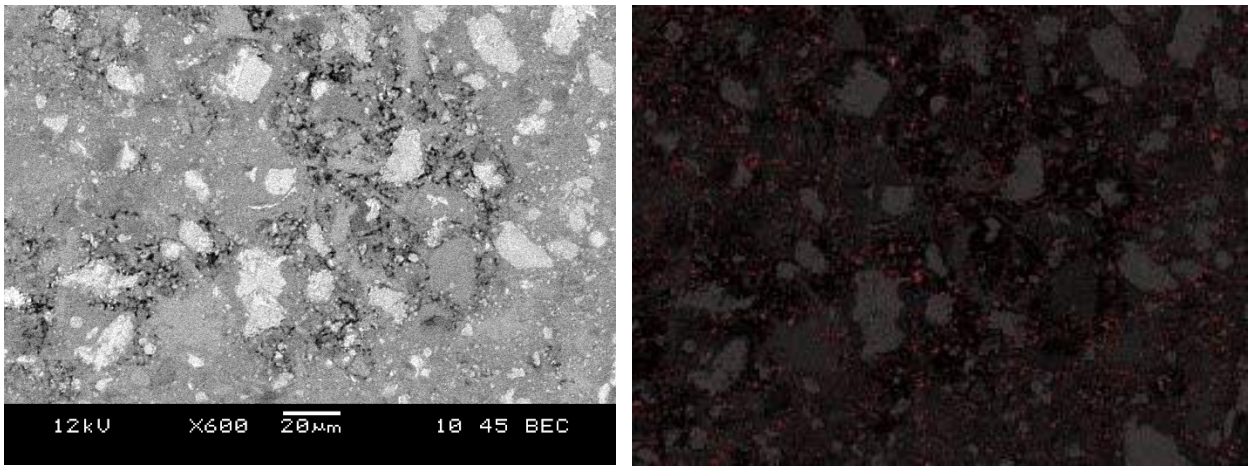

(a) (b)

Figure 4-7 White TiO_2, 0% SCM micrograph at (a) 600x magnification and (b) an accompanying Ti EDS element map overlay. Ti indicated in red

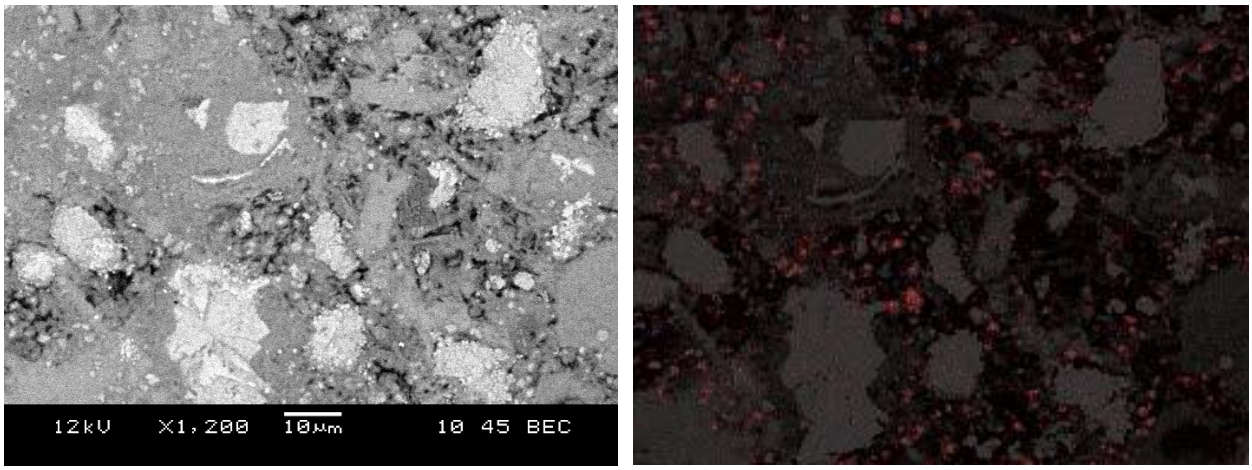

(a) (b)

Figure 4-8 White TiO_2, 0% SCM micrograph at (a) 1200x magnification and (b) an accompanying Ti EDS element map overlay. Ti indicated in red

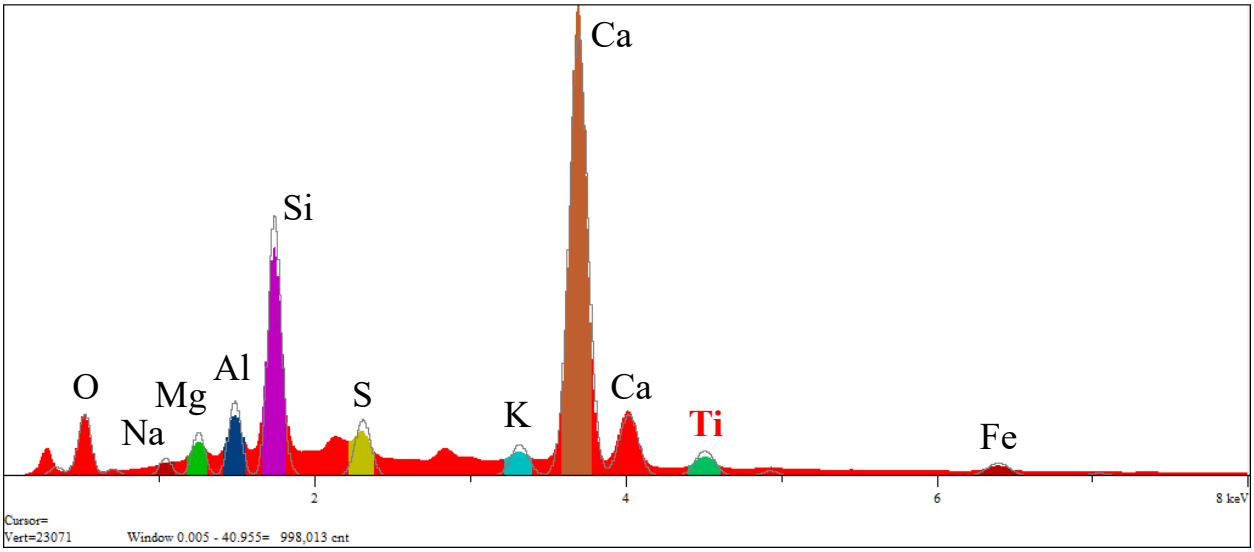

Figure 4-9 Full elemental spectrum for White TiO_2 map scan in Figure 4.8

4.5. DISCUSSION OF RESULTS

4.5.1. Microstructural Analysis

4.5.1.1. Phase and Compositional Analysis

The phases observed in BEI of photocatalytic cement paste were consistent with those described in the literature for Portland cement paste. Besides the presence of TiO_2 nanoparticles, no significant differences were observed between the microstructures of the photocatalytic and control samples. For all mixes, the TiO_2 nanoparticles appeared to be relatively well-dispersed throughout the samples, i.e. few large clusters or bunches. Some small clusters appear to be visible in the map scans in Figures 4.7 and 4.8. The EDS line scan (Figure 4.6) also shows variation in the Ti spectrum as a function of distance along the scan, with higher peaks occurring where nanoparticles appear to be spaced more closely together.

Although a full quantitative analysis was not performed, a quick calculation performed on the map scans for each mix inferred that the content of the commercial photocatalytic cement samples (White TiO_2 and Gray TiO_2) appeared to be similar to the hand-mixed Anatase samples with a 2.5% TiO_2 replacement rate.

The most important finding in characterizing the microstructure of the specimens through BEI and EDS was the general location of the TiO_2 nanoparticles. As demonstrated by Figures 4.7 and 4.8, the nanoparticles were found mostly in the porous groundmass and surrounding the larger capillary pores, and this finding was consistent for all mixes. The nanoparticles were not nearly as prevalent in areas containing solid hydration products or unreacted cement particles. The consistency with which TiO_2 nanoparticles were located in and near pores suggests that, as described in the literature, porosity plays a crucial role in photocatalytic activity.

The 10% Anatase sample from Figure 4.6 probably contained the most TiO_2 within the solid hydration products. Despite the poor image quality, Ti peaks can be observed in some of these solid areas, particularly on the far right edge of the scan. Nevertheless, the highest Ti peaks occur where the analysis line is passing over the groundmass, where capillary pores are woven around amorphous C-S-H gel. The high TiO_2 content of this mix likely caused some nanoparticles to be located in areas where they were not typically found.

4.5.1.2. Impact of Supplementary Cementitious Materials and Carbonation

Small, rounded fly ash particles were observed in the microstructure of the mixes containing fly ash, as indicated in Figure 4.4. As discussed in Chapter 3, fly ash (and silica fume) should react with CH to produce more C-S-H in the microstructure. However, this impact on the morphology could not be characterized by appearance alone, as CH phases were still visible in the micrographs of fly ash specimens and would not be completely consumed anyway, even if the specimens had been cured for longer than 3 days. EDS could also not be used to quantify the impact of fly ash on the microstructure. EDS only offers elemental analysis, so it was not possible to distinguish between C-S-H and CH.

Silica fume particles were also observed throughout the microstructure. However, these particles were often very large, appeared to have agglomerated, and had reacted to a limited extent, if at all. An example of a silica fume particle that appears to be undisturbed in the microstructure can be seen in Figure 4.10. The particle was positively identified as Si by an EDS map scan, and its dark color in the BEI micrograph fits the profile of SiO_2, for which the estimated η (0.125) would be lower than any of the hydrated cement phases. The size of the unreacted particle in

Figure 4.10 makes it somewhat of an extreme example, but illustrates the phenomenon very clearly. The agglomeration and lack of reactivity would seem to indicate that the silica fume may be too dense, or was not mixed thoroughly enough into the paste. Future studies incorporating silica fume should aim to use undensified silica fume.

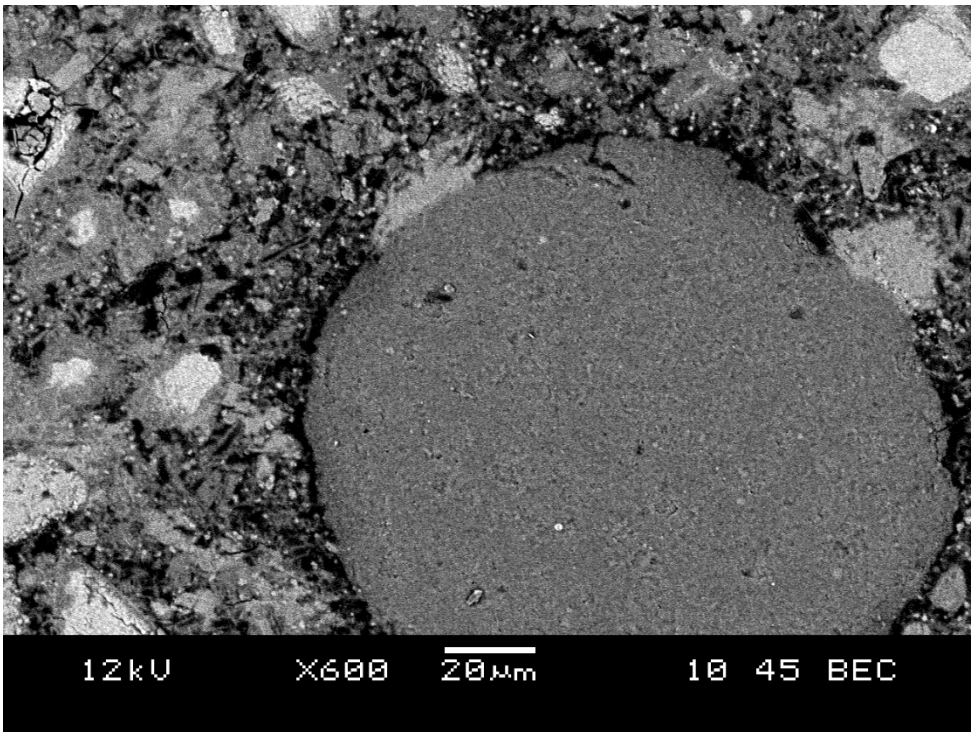

Figure 4-10 TiO_2 White, 5% Silica Fume micrograph featuring a very large, unreacted or agglomerated silica fume particle

Limited insight was gained into carbonation from BEI and EDS. Although calcium carbonate should have precipitated onto the carbonated sample surfaces, it was not detected by either backscatter imaging or EDS compositional analysis. In the case of BEI, the η of $CaCO_3$ is 0.142, which falls within the estimated range of η values for C-S-H (0.130-0.150). Thus, $CaCO_3$ cannot easily be distinguished from C-S-H in backscatter images. It is also not possible to detect $CaCO_3$ in EDS, as the carbon-based epoxy in which the samples are impregnated causes a uniform C profile to appear across the entire sample surface.

As discussed in Chapter 3, one proposed theory for why carbonation harms photocatalytic efficiency is that the precipitation of $CaCO_3$ shields the TiO_2 nanoparticles at the surface (Diamanti *et al.* 2013, Hanson 2014). Although EDS could not be used to detect $CaCO_3$, the surfaces of the carbonated specimens were analyzed to see if there was a noticeable drop in Ti content compared to non-carbonated specimens. Ultimately, no difference in Ti content was observed between the carbonated and non-carbonated mixes. EDS may have been able to detect Ti below the surface or carbonates but within the interaction volume, causing no difference to be observed. Either way, the findings do not show any evidence of shielding or coverage of TiO_2 at the surface because of carbonation.

4.5.1.3. Porosity

Based on the results found in Tables 4.1 and 4.2, there was limited differentiation in the measured porosity and pore size between the mixes tested in this study. For all mixes, 2-D pore area fraction generally fell in the range of 0.08-0.20, and median pore sizes for all mixes were roughly within the range of 0.3 to 1.0 µm, a narrow band in terms of pore size indicative of larger capillary pores, or macropores (Mindess *et al.* 2003). If there were significant differences in pore size distribution, the median pore size would be expected to differ by orders of magnitude, particularly for a mix with smaller- to medium-sized capillary pores, or mesopores.

Minimal differentiation in porosity was also measured between the TiO_2 mixes and the control mixes, which was not expected based on previous studies where nanoparticles led to measurable decrease in porosity measured by MIP (Nazari and Riahi 2011, Zhang and Li 2011). Increasing TiO_2 content in the hand-mixed Anatase specimens from 2.5 to 10% also did not cause any significant or consistent impact on porosity.

Consistent with the findings described above, adding fly ash had no consistent effect on porosity and pore size, which was unexpected. However, since non-carbonated specimens were cut and vacuum dried after only three days of curing, this result may not be indicative of long-term impact on porosity because pozzolanic reactions take a longer time to fully react and consume available calcium hydroxide. The addition of silica fume also had no discernable impact on the pore structure. Although this finding greatly contradicts the known behavior of silica fume (densifies the pore structure), it was unsurprising given that it did not appear to react much within the microstructure, as demonstrated in Figure 4.10. In addition to insufficient curing time, use of densified silica fume also likely exacerbated the issue.

No direct impact of carbonation on porosity was observed in the data. Figures 4.11 and 4.12 plot the carbonated porosity versus the non-carbonated porosity and median pore area, respectively, for each mix. A line of unity is drawn in both figures to help illustrate any trends in the data. However, as seen in Figures 4.11 and 4.12, the data points appear to be scattered randomly on either side of the line, indicating that no effects of carbonation on porosity of the mixes were observed.

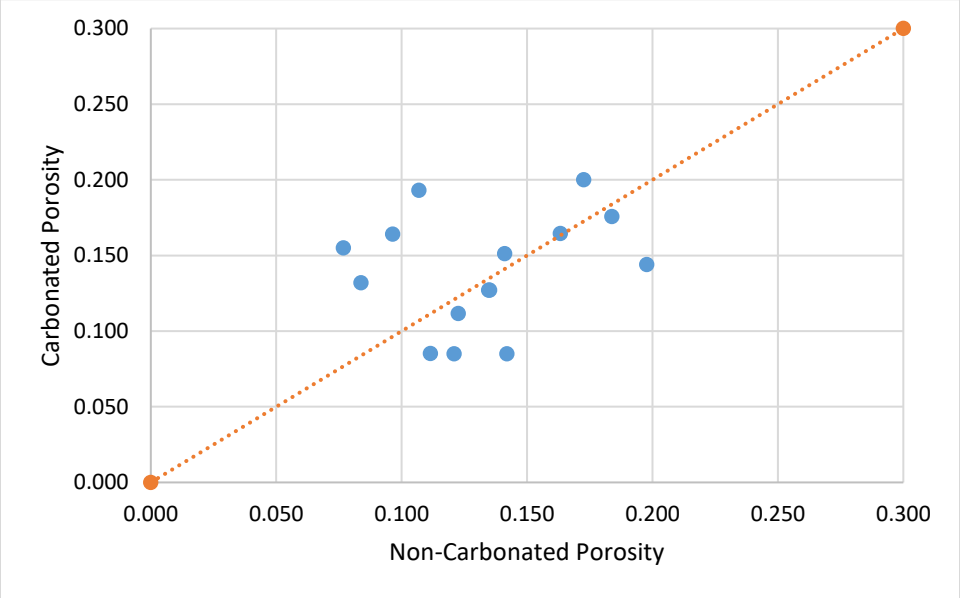

Figure 4-11 Relationship between carbonation and porosity

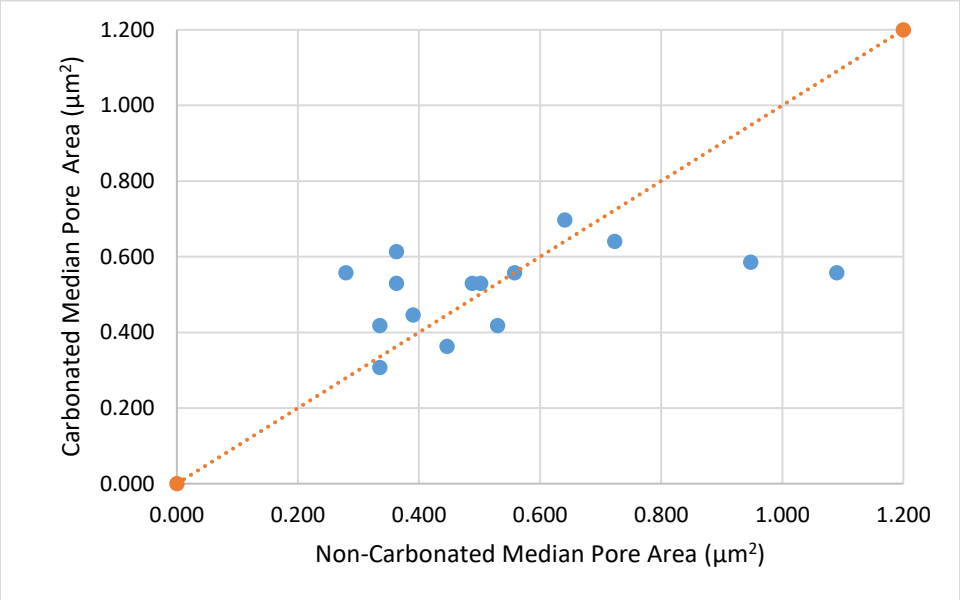

Figure 4-12 Relationship between carbonation and median pore area

Overall the measured porosity values did not differ widely between mixes, making it impossible to discern trends with SCM addition or carbonation. However, these findings most likely result from issues with testing preparation and methodology. Since each photocatalytic specimen was prepared at the same w/cm and cured for only three days, the opportunity for distinctly different pore structures to develop between the mixes may have been limited. The specimen preparation methods may have also made it impossible to measure the true surface porosity. SEM specimens had to be cut from slightly down below the surface in order to obtain flat, polished samples, meaning that the cast surface pore structure may have been lost.

4.5.2. Porosity and Photocatalytic Efficiency

Given the limited differentiation in measured porosity values between the mixes, it is unsurprising that no apparent relationship was observed between porosity and NOx removal efficiency. Scatter plots comparing porosity and PEF (data taken from results in Chapter 3) for each mix are shown in Figures 4.13 and 4.14 for carbonated and non-carbonated specimens, respectively, demonstrate a lack of correlation between PEF and porosity.

As discussed in the previous chapter, the specimen's reflectance was a factor in the enhanced photocatalytic performance of the White TiO_2 samples. As seen in Table 4.1, some of the white cement specimens had higher-than-average porosities, but this finding was not consistent across all white cement samples with all SCM types, so it likely results from normal sample variation. Therefore, no correlation was noted between porosity and albedo for the samples tested.

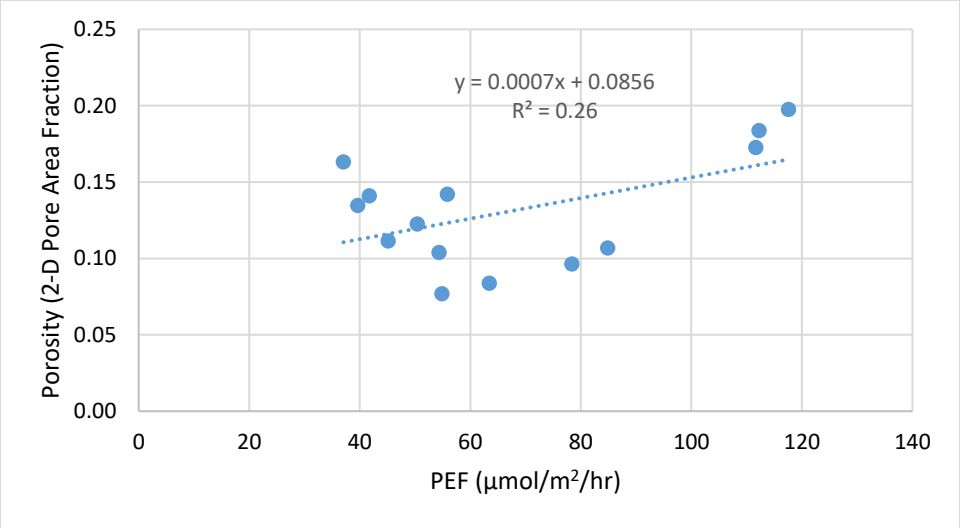

Figure 4-13 Porosity vs. PEF for non-carbonated specimens

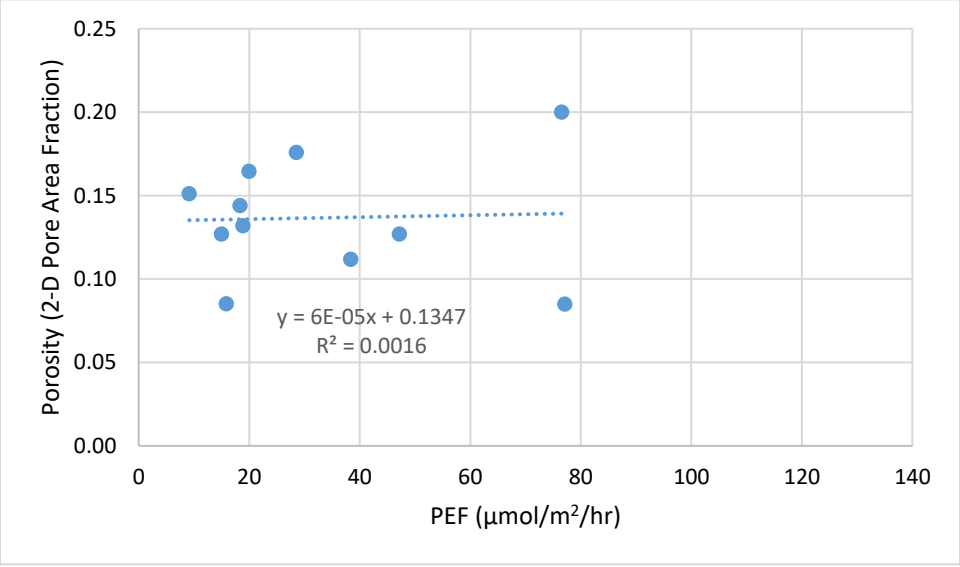

Figure 4-14 Porosity vs. PEF for carbonated specimens

4.5.3. Microstructure of Carbonated Specimens and Photocatalytic Efficiency

As noted in sections 4.5.1.1 and 4.5.1.3, limitations in the testing procedures prevented determination of whether carbonation caused shielding of TiO_2 nanoparticles in the samples or if it affected the porosity or pore size distribution of the paste, which are the most common theories to explain why photocatalytic activity decreases in carbonated concrete. As previously mentioned, a lack of curing time may have prevented the microstructure from fully developing in all specimens, particularly those containing SCMs. The necessity of cutting specimens for SEM analysis from just below the sample's cast surface may also have made it impossible to observe the true surface porosity.

The results of the microstructural analysis did show that the pore structure appeared to be an important factor in photocatalytic ability. EDS compositional analysis also suggested that there

was no decline in the presence of Ti at the sample surface because of carbonation. These findings, coupled with many studies in the literature detailing the importance of porosity and/or w/cm to photocatalytic performance (Chen and Poon 2009, Diamanti *et al.* 2013, Sugrañez *et al.* 2013, Lucas *et al.* 2013, Lee *et al.* 2014), would make it seem more likely that a reduction in porosity is the main cause of the decline in photocatalytic efficiency caused by carbonation.

4.6. CONCLUSIONS

Analyzing the microstructure of photocatalytic concrete can provide a better understanding of the properties of photocatalytic cements and the factors affecting the mechanisms of NOx removal ability. Common microstructural analysis techniques were performed on flat, polished cement paste specimens to characterize microstructural properties such as porosity and determine their role in photocatalytic performance.

Using BEI and EDS, the microstructural morphology of photocatalytic cement paste was characterized. During this analysis, the majority of the TiO_2 nanoparticles appeared well-dispersed. Most importantly, the nanoparticles were predominantly located in and around the pores. Based on these findings, the pore structure would appear to be very important to the NOx removal ability of photocatalytic cement. Analyzing relative Ti compositions determined by EDS, the TiO_2 content of the commercial photocatalytic cements (used to create the White and Gray TiO_2 specimens) was estimated to be around 2.5% by mass of cement.

Unfortunately, measured values for porosity and pore size were not significantly different between all mixes for the project. Therefore, it was not possible to determine the effects of SCMs or carbonation on porosity, or to directly assess the overall impact of porosity on NOx removal efficiency. These findings likely resulted from limitations inherent in the testing methodology and sample preparation. Despite the fact that it was not possible to draw any conclusions about the relationship between porosity and photocatalytic performance from the results of this study, the microstructural analysis showed evidence that porosity is a key factor in photocatalytic efficiency and is likely behind the decline in NOx removal ability caused by carbonation.

Based on the results of this investigation, and in part to some of the limitations of some of the testing techniques utilized, there are several areas that appear ripe for future work to continue to develop understanding of the microstructural properties of photocatalytic concrete. An experiment in which w/cm ratios and curing times are varied would allow for a greater degree of microstructural development. With more time for hydration, it should be possible to observe significant differences in porosity and pore structure between mixes, allowing for determination of the effect of porosity on photocatalytic performance. Varying w/cm may also provide more insight into the sensitivity of microstructural properties of photocatalytic concrete to carbonation and the addition of SCMs. Additionally testing the cast and mold surface of the same sample would also provide insight into within specimen porosity changes.

Additionally, besides SEM and EDS, other material characterization techniques such as X-ray fluorescence (XRF) may be capable of performing a more accurate quantitative compositional analysis to determine TiO_2 content. Finally, both XRF and Fourier transform infrared spectroscopy (FTIR) are useful for studying calcium carbonate phases in cementitious materials. These techniques could be used to further characterize the impact of carbonation on the microstructure and photocatalytic activity.

CHAPTER 5-CONCLUSIONS

5.1. KEY FINDINGS

In this study, FFC mixes constructed with photocatalytic cement were investigated in the laboratory to determine their multi-functional structural and environmental benefits. Fresh concrete was tested to characterize constructability, and beam and cylindrical specimens were cast for testing of strength and fracture properties. NOx removal ability was determined through photoreactor testing, where mortar mixtures were prepared while varying cement type, TiO_2 content, and the addition of supplementary cementitious materials to analyze how those properties impacted photocatalytic performance. Additional specimens were also artificially carbonated to investigate its effect on photocatalytic efficiency, and spectrophotometer testing was performed to characterize the reflectance of the chosen mix designs as well as analyze the impact of reflectance on photocatalytic efficiency. Finally, microstructural analysis was performed using scanning electron microscopy and related image analysis techniques to better characterize the microstructure of photocatalytic cement paste and relate microstructural properties to photocatalytic performance.

Testing of fresh concrete determined that, despite a small but measurable decrease in workability, photocatalytic FFC inlays should offer the same constructability benefits as conventional FFC. Beam and cylindrical specimens tested at 7 and 28 days suggested that mechanical properties of photocatalytic FFC were for the most part statistically the same as conventional FFC. Therefore, photocatalytic FFC mixes appear to be well-suited for application in thin concrete inlays and should provide effective, durable performance for a reasonable service life.

Laboratory photoreactor testing established that the photocatalytic FFC mortar specimens removed NOx at a rate that should make it effective for application in the urban near-road environment. However, artificial carbonation of the specimens demonstrated a significant decrease in NOx removal ability, greater in magnitude than previously noted by several previous researchers. The detrimental effects of carbonation were able to be partially mitigated through the addition of fly ash. Replacing up to 30% of cement with fly ash was shown to help overcome the decline in NOx removal ability because of carbonation, but it may not be advantageous to use replacement rates that high in conjunction with photocatalytic cement blends, as the addition of fly ash also reduces the TiO_2 content of the mix. For this reason, fly ash replacement rates of 15% may prove more optimal for counteracting carbonation. Increasing TiO_2 content up to 10% by weight of cement also showed promise in helping mitigate the decline in photocatalytic efficiency caused by carbonation but probably is not economically practical.

Reflectance was shown to correlate with photocatalytic ability with more reflective mixes, as measured by albedo and/or UV-A reflectance, demonstrating greater NOx removal performance. These effects were particularly evident when comparing mixes cast with white cement versus gray cement. Overall, white cement samples with the same SCM type and replacement rate exhibited significantly greater photocatalytic performance than their gray cement counterparts. These trends were also observed when reflectance changed for samples of a given cement type.

For example, adding more fly ash to Anatase samples made with gray cement increased their reflectance, leading to a corresponding increase in photocatalytic efficiency. The relationship between reflectance and photocatalytic performance was likely because of the diffuse reflectance at the sample surface that promoted more absorbance of UV-A radiation by near-surface TiO_2 nanoparticles, driving the photocatalytic reaction with NOx.

Microstructural analysis of cement paste samples revealed that TiO_2 nanoparticles were well-dispersed in the cementitious matrix, primarily located in and around pores. This finding suggested that, following work by other researchers, porosity plays a key role in photocatalytic ability. Image thresholding analysis to quantify porosity and relate it to factors including carbonation and addition of supplementary cementitious materials was largely inconclusive because of limitations inherent in the sample preparation and testing procedures. The results did provide insight into the mechanism through which carbonation inhibits photocatalytic performance. Between the two prevailing theories, the microstructural morphology suggested it is more likely that reduced porosity caused by carbonation is what constrains the reaction, as opposed to shielding of TiO_2 nanoparticles.

Taking into consideration the collective findings of this study, the most photocatalytic mix design for NOx removal that could be achieved using the materials available in this study would incorporate a white photocatalytic cement blend with 15% fly ash replacement. Such a mix design provides a balance between the benefits associated with adding fly ash to provide resilience to carbonation as well as the enhanced photocatalytic activity associated with white cement and a greater reflectance. Further improvements could be made at the margins by making slight increases to TiO_2 content to further protect against carbonation or to w/cm to increase porosity and promote NOx removal.

5.2. FUTURE WORK

Certain key findings of this study will provide immediate benefits to selection and application of photocatalytic cements in pavements and other concrete-related uses. Other findings may not provide immediate insight, but still serve as a point from which to launch further research of photocatalytic cementitious materials. One future research area could be to study the effects of carbonation and reflectance on cement of mortar samples treated with photocatalytic surface coatings to see if a different type of TiO_2 application is affected differently by those factors. The relationship between reflectance and photocatalytic performance is also a good topic for further investigation, especially into the mechanism causing a spike in photocatalytic activity and how it can be utilized most effectively.

The microstructural analysis performed in this study can also be expanded upon for future work. A more thorough investigation of the porosity of photocatalytic cement paste could be achieved by analyzing different mixture properties such as w/cm and curing condition. These changes could allow for a more thorough characterization of the impact of porosity on photocatalytic performance as well as carbonation on photocatalytic cement. Seeking out more and different alternative material characterization techniques can also help provide more information about the microstructure and help overcome some of the limitations associated with sample preparation for the techniques used in this study.

Above all, with work in the laboratory setting continuing to establish the viability of photocatalytic cementitious materials, more research needs to move into the field to verify its

performance in real-world applications. As discussed in this study, field testing poses a significant number of challenges. An urban test section that can be treated or reconstructed with a photocatalytic pavement must be identified. The type and placement of NOx analyzers must ensure that accurate and useful data on near-road NOx levels is obtained. From there, expensive and meticulous real-time monitoring is required to fully characterize the impact of variables such as traffic levels, wind speed and direction, sunlight and weather, but long-term monitoring is also necessary to characterize longer-term impacts on NOx levels. Though the sheer number of issues that need to be addressed for field testing can be daunting, the findings of this study can provide guidance for choosing the right mix properties and environmental variables to consider, providing a strong foundation for a successful field experiment.

REFERENCES

1. ASTM. 2003. “Standard Tables for Reference Solar Spectral Irradiances: Direct Normal and Hemispherical on 37° Tilted Surface.” G173, West Conshohocken, PA.

2. ASTM. 2005. “Standard Test Method for Compressive Strength of Cylindrical Concrete Specimens.” C39, West Conshohocken, PA.

3. ASTM. 2010. “Standard Guide for Examination of Hardened Concrete Using Scanning Electron Microscopy.” C1723, West Conshohocken, PA.

4. ASTM. 2011. “Standard Test Method for Splitting Tensile Strength of Cylindrical Concrete Specimens.” C496, West Conshohocken, PA.

5. ASTM. 2012. “Standard Test Method for Solar Absorptance, Reflectance, and Trasmittance of Materials Using Integrating Spheres.” E903, West Conshohocken, PA.

6. ASTM. 2013. “Standard Test Method for Flexural Performance of Fiber-Reinforced Concrete.” C1609, West Conshohocken, PA.

7. ASTM. 2014. “Standard Test Method for Air Content of Freshly Mixed Concrete by the Pressure Method.” C231, West Conshohocken, PA.

8. ASTM. 2014. “Standard Practice for Mechanical Mixing of Hydraulic Cement Pastes and Mortars of Plastic Consistency.” C305, West Conshohocken, PA.

9. ASTM. 2015. “Standard Practice for Making and Curing Concrete Test Specimens in the Laboratory.” C192, West Conshohocken, PA.

10. Ballari, M. M., Hunger, M., Husken, G., and Brouwers, H. J. H. 2010. “NOx Photocatalytic Degradation Employing Concrete Pavement Containing Titanium Dioxide.” Applied Catalysis B: Environmental: 245-254.

11. Beeldens, A., and Boonen, E. 2012. “A Double Layered Photocatalytic Concrete Pavement: a Durable Application with Air-Purifying Properties.” Proceedings of the 10th International Conference on Concrete Pavements: 924-935.

12. Boonen, E., and Beeldens, A. (2013). “Photocatalytic Roads: From Lab Tests to Real Scale Applciations.” European Transportation Review, 5: 78-89.

13. Bordelon, A.C. 2011. “Flowable Fibrous Concrete for Thin Concrete Inlays.” PhD Dissertation, University of Illinois at Urbana-Champaign.

14. Bordelon, A. C., and Roesler, J. R. 2011. “Flowable Fibrous Concrete for Thin Concrete Inlays.” Proceedings of the 1st Congress of the Transportation and Development Institute of ASCE, American Society of Civil Engineers: 874-883.

15. Berkowicz, R. 2000. “OPSM – A Paramterised Street Pollution Model.” Environmental Monitoring and Assessment, 65: 323-331.

16. Bygott, C. E., Maltby, J. E., Stratton, J. L., and McIntyre, R. 2007. “Photocatalytic Coatings for the Construction Industry.” Proceedings of the International RILEM Symposium on Photocatalysis, Environment and Construction Materials, Florence, Italy.

17. Cackler, T., Allerman, J., Kevern, J., and Sikkema, J. 2012. “Technology Demonstrations Project: Environmental Impact Benefits with TX Active Concrete Pavement in Missouri DOT Two-Lift Highway Construction Demonstration.” National Concrete Pavement Technology Center, Report No. DTFH61-H-00011.

18. Cassar, L., Pepe, C., Tognon, G., Guerrini, G. L., and Amadelli, R. 2003. “White Cement for Architectural Concrete Possessing Photocatalytic Properties.” Proceedings of the 11th International Congress on the Chemistry of Cement. Durban.

19. Chen, J., and Poon, C. 2009. “Photocatalytic Cementitious Materials: Influence of the Microstructure of Cement Paste on Photocatalytic Pollution Degradation.” Environmental Science and Technology, 43 (23).

20. Chen, J., Kou, S. C., and Poon, C. S. 2011. “Photocatalytic Cement-Based Materials: Comparison of Nitrogen Oxides and Toluene Removal Potentials and Evaluation of Self-Cleaning Performance.” Building and Environment, 46: 1827-1833.

21. Claisse, P. A., Elsayad, H. I., and Shaaban, I. G. 1999. “Permeability and Pore Volume of Carbonated Concrete.” ACI Materials Journal, 96 (3): 378-381.

22. Clements, A., Jia, Y., Denbleyker, A., McDonald-Buller, E., Fraser, M., Allen, D., Collins, D., Michel, E., Pudota, J., Sullivan, D., and Zhu, Y. 2009. “Air Pollutant Concentrations near Three Teas Roadways, Part II: Chemical Characterization and Transformation of Pollutants.” Atmospheric Enivroment, 43: 4523-4534.

23. Crittenden, J. C., Zhang, Y., Hand, D. W., and Marchand, E. G. 1996. “Solar Detoxification of Fuel-Contaminated Groundwater Using Fixed-Bed Photocatalysis.” Water Environment Research, 68 (3): 270-277.

24. Devahasdin, S., Fan Jr., C., Li , K., and Chen, D. H. 2003. “TiO_2 Photocatalytic Oxidation of Nitrogen Oxide: Transient Behavior and Reaction Kinetics. Journal of Photochemistry and Photobiolgoy A: Chemistry, 156: 161-170.

25. Diamanti, M. V., Ormellese, M., and Pedeferri, M. 2008. “Characterization of Photocatalytic and Supherhydrophilic Properties of Mortars Containing Titanium Dioxide.” Cement and Concrete Research, 38: 1349-1353.

26. Diamanti, M. V., Lollini, F., Pedeferri, M. P., and Bertolini, L. 2013. “Mutual Interactions Between Carbonation and Titanium Dioxide Photoactivity in Concrete.” Building and Environment, 62: 174-181.

27. Diamond, S. 2000. “Mercury Porosimetry: An Inappropriate Method for the Measurement of Pore Size Distributions in Cement-Based Materials.” Cement and Concrete Research, 30: 1517-1525.

28. Diamond, S. 2004. “The Microstructure of Cement Paste and Concrete—a Visual Primer.” Cement and Concrete Composites, 26: 919-933.

29. Dylla, H., Hassan, M. M., Schmitt, M., Rupnow, T., Mohammad, L. N., and Wright, E. 2011. “Effects of Roadway Contaminants on Titanium Dioxide Photodegradation of Nitrogen Oxides.” Transportation Research Record: Journal of the Transportation Research Board, 2240: 22-29

30. Dylla, H., Hassan, M. M., and Osborn, D. 2012. “Field Evaluation of Ability of Photocatalytic Concrete Pavements to Remove Nitrogren Oxides.” Transportation Research Record: Journal of the Transportation Research Board, 2290: 154-160.

31. Environmental Protection Agency. 2010. “Primary National Ambient Air Quality Standards for Nitrogen Dioxide.” Federal Register, 75 (26).

32. Goldstein, J., Newbury, D. E., Joy, D. C., Lyman, C. E., Echlin, P., Lifshin, E., Sawyer, L., and Michael, J. R. 1992. Scanning Electron Microscopy and X-Ray Microanalysis, Plenum Press, New York.

33. Guerrini, G. L., and Peccati, E. 2007. “Photocatalytic Cementitious Roads for Depollution.” Proceedings of the International RILEM Symposium on Photocatalysis, Environment and Construction Materials, Florence, Italy.

34. Guo, M. Z., and Poon, C. S. 2012. “An Effective Way to Incorporate Nano-TiO2 in Photocatalytic Cementitious Materials.” Proceedings of the Third International Conference on Sustainable Construction Materials and Technologies, Kyoto, Japan.

35. Hanson, S., and Tikalsky, P. 2013, “Influence of Ultraviolet Light on Photocatalytic TiO_2 Materials.” Journal of Materials in Civil Engineering, 25: 893-898.

36. Hanson, S. 2014. “Evaluation of Concrete Containing Photocatalytic Titanium Dioxide.” PhD Dissertation, The University of Utah.

37. Hassan, M. M., Dylla, H., Mohammed, L. N., and Rupnow, T. (2010). “Evaluation of the Durability of Titanium Dioxide Photocatalyst coating for Concrete Pavement.” Construction and Building Materials. 24: 1456-1461.

38. Husken, G., Hunger, M., and Brouwers, H. J. H. (2009). “Experimental Study of Photocatalytic Concrete Products for Air Purification.” Building and Environment, 44: 2463-2474.

39. Hwang, S., Lee, M. C., and Choi, W. (2003). “Highly Enhanced Photocatalytic Oxidation of CO on Titania Deposited with Pt Nanoparticles: Kinetics and Mechanism.” Applied Catalysis B: Enviornmental, 46 (1): 49-63.

40. ISO. 2007. “Fine Ceramics (Advanced Ceramics, Advanced Technical Ceramics) – Test Method for Air-Purification Performance of Semiconducting Photocatalytic Materials – Part 1: Removal of Nitric Oxide.” 22197-1, Switzerland.

41. Jayapalan, A. R., Lee, B. Y., Land, E. M., Bergin, M. H., and Kurtis, K. E. 2015. “Photocatalytic Efficiency of Cement-Based Materials: Demonstration of Proposed Test Method.” ACI Materials Journal, Technical Paper M-2013-222.

42. Jiang, J., Oberdorster, G., Elder, A., Gelein, R., Mercer, P., and Biswas, P. 2008. “Does Nanoparticle Activity Depend upon Size and Crystal Phase?” Nanotoxicology, 2 (1): 33-42.

43. Lackhoff, M., Prieto, X., Nestle, N., Dehn, F., and Niessner, R. 2003. “Photocatalytic Activity of Semiconductor-modified Cement—Influence of Semiconductor Type and Cement Ageing.” Applied Catalysis B: Environmental, 43: 205-216.

44. Lange, D., Jennings, H. M., and Shah, S. P. 1994. “Image Analysis Techniques for Characterization of Pore Structure of Cement-Based Materials.” Cement and Concrete Research, 24 (5): 841-853.

45. Lee, B. Y., and Kurtis, K. E. 2010. “Influence of TiO_2 Nanoparticles on Early C_3S Hydration.” Journal of the American Ceramic Society. 93 (10): 3399-3405.

46. Lee, B. Y. 2012. “Effect of Titanium Dioxide Nanoparticles on Early Age and Long Term Properties of Cementitious Materials.” PhD Dissertation, Georgia Institute of Technology.

47. Lee, B. Y., Jayapalan, A. R., Bergin, M. H., and Kurtis, K. E. 2014. “Photocatalytic Cement Exposed to Nitrogen Oxides: Effect of Oxidation and Binding.” Cement and Concrete Research, 60: 30-36.

48. Levinson, R., and Akbari, H. 2002. “Effects of Composition and Exposure on the Solar Reflectance of Portland Cement Concrete.” Cement and Concrete Research, 32: 1679-1698.

49. Lucas, S. S., Ferreira, V. M., and Barroso de Aguiar, J. L. 2013. “Incorporation of Titanium Dioxide Nanoparticles in Mortars—Influence of Microstructure in the Hardened State Properties and Photocatalytic Activity.” Cement and Concrete Research, 43: 112-120.

50. Mindess, S., Young, J. F., and Darwin, D. 2003. “Concrete,” 2nd Edition, Pearson Education, Inc., Upper Saddle River, NJ.

51. Nakamura, I., Negishi, N., Kutsuna, S., Ihara, T., Sugihara, S., and Takeuchi, K. 2000. “Role of Oxygen Vacancy in the Plasma-Treated TiO2 Photocatalyst with Visible Light Activity for NO Removal.” Journal of Molecular Catalysis A: Chemical, 161: 205-212.

52. Nazari, A., and Riahi, S. 2011. “The Effects of TiO_2 Nanoparticles on Properties of Binary Blended Concrete.” Journal of Composite Materials, 45: 1181-1188.

53. Nazari, A., Riahi, S., Riahi, S., Shamekhi, S. F., and Khademno, A. 2010. “Assessment of the Effects of the Cement Paste Composite in Presence TiO2 Nanoparticles.” Journal of American Science, 6 (4): 43-46.

54. Osborn, D., Hassan, M. M., and Dylla, H. 2012. “Quantification of Reduction of Nitrogen Oxides by Nitrate Accumulation on Titanium Dioxide Photocatalytic Concrete Pavement.” Transportation Research Record: Journal of the Transportation Research Board, 2290: 147-153.

55. Panesar, D.K., and Dolatabadi, M. 2014. “Properties of Photocatalytic Concrete.” Journal of the Chinese Ceramic Society, 42 (5): 579-584.

56. Peshkin, D., Smith, K.L., Wolters, A., Krstulovich, J., Moulthrop, J., and Alvarado, C. 2011. “Preservation Approaches for High-Traffic-Volume Roadways.” SHRP 2 Report S2-R26-RR-1, Transportation Research Board, Washington, D.C.

57. Pinna, F., Trevisan, V., Cassar, L, Peccati, E., Pepe, C., and Pernicone, N. 2007. “Study of the NO2 Surface Saturation of Photocatalytic Cements.” Proceedings of the International RILEM Symposium on Photocatalysis, Environment and Construction Materials, Florence, Italy.

58. Poon, C. S., and Cheung, E. 2007. “NO Removal Efficiency of Photocatalytic Paving Blocks Prepared with Recycled Materials.” Construction and Building Materials, 21: 1746-1753.

59. Poon, C. S., and Guo, M. Z. 2015. “Effect of Cement Types on Photocatalytic NOx Removal and its Underlying Mechanism.” Proceedings of Nanotechnology in Construction Materials, 5: 333-340.

60. Scrivener, K. L. 2004. “Backscattered Electron Imaging of Cementitious Microstructures: Understanding and Quantification.” Cement and Concrete Composites, 26: 935-945.

61. Sen, S. 2015. “Impact of Pavements on the Urban Heat Island.” Master’s Thesis, University of Illinois at Urbana-Champaign.

62. Sen, S., King, D., and Roesler, J. R. 2015. “Structural and Environmental Benefits of Concrete Inlays for Pavement Preservation.” Airfield and Highway Pavements 2015: 697-707.

63. Shah, S.P. 1990. “Determination of Fracture Parameters of Plain Concrete Using Three-Point Bend Tests.” Materials and Structures, 23 (6): 457-460.

64. Siegel, R., and Howell, J. 2002. “Thermal Radiation Heat Transfer.” 4th Ed., Taylor & Francis, New York, NY.

65. Sikkema, J. K., Alleman, J. E., Ong, S. K., Koziel, J. A., Taylor, P. C., and Bai, H. 2012. “Photocatalytic Concrete Pavements: Decrease in NOx Oxidation due to Reaction Product Blinding.” Proceedings of the International Conference on Long-Life Concrete Pavement, September 18-21, Seattle.

66. Sikkema, J. K. 2013. “Photocatalytic Degradation of NOx by Concrete Pavement Containing TiO_2.” PhD Thesis, Iowa State University.

67. Sugrañez, R., Alvarez, J. I., Cruz-Yusta, M., Marmol, I., Morales, J., Vila, J., and Sanchez, L. 2013. “Enhanced Photocatalytic Degradation of NOx Gases by Regulating the Microstructure of Mortar Cement Modified with Titanium Dioxide.” Building and Environment, 69: 55-63.

68. Terpeluk, A. L. 2012. “Effects of Photocatalysis on Concrete Surfaces.” Master’s Thesis, University of Texas at Austin.

69. Thoma, E. D., Shores, R. C., Isakov, V., and Baldauf, R. W. (2008). “Characterization of Near-Road Pollutant Gradients Using Path-Integrated Optical Remote Sensing. Journal of the Air and Waste Management Association, 58: 879-890.

70. Wikipedia, the Free Encyclopedia. 2015. “Diffuse Reflection.” Accessed 15 July 2015. <https://en.wikipedia.org/wiki/Diffuse_reflection>

71. Wong, H. S., Head, M. K., and Buenfeld, N. R. (2006). “Pore Segmentation of Cement-Based Materials from Backscattered Electron Images.” Cement and Concrete Research, 36: 1083-1090.

72. van Ginneken, B., Stavridi, M., and Koenderink, J.J. 1998. "Diffuse and specular reflectance from rough surfaces." Applied optics, 37.1: 130-139.

73. Zhang, J. and Li, V. C. 2002. “Monotonic and Fatigue Performance in Bending of Fiber-Reinforced Engineered Cementitious Composite in Overlay System.” Cement and Concrete Research, 32 (3): 415-423.

74. Zhang, M., and Li, H. 2011. “Pore Structure and Chloride Permeability of Concrete Containing Nano-Particles for Pavement.” Construction and Building Materials, 25: 608-616.

75. Zhao, Y., Han, J., Shao, Y., and Feng, Y. 2009. “Simultaneous SO2 and NO Removal from Flue Gas Based on TiO2 Photocatalytic Oxidation.” Environmental Technology, 30 (14): 1555-1563.

APPENDIX: PHOTOREACTOR TEST DATA

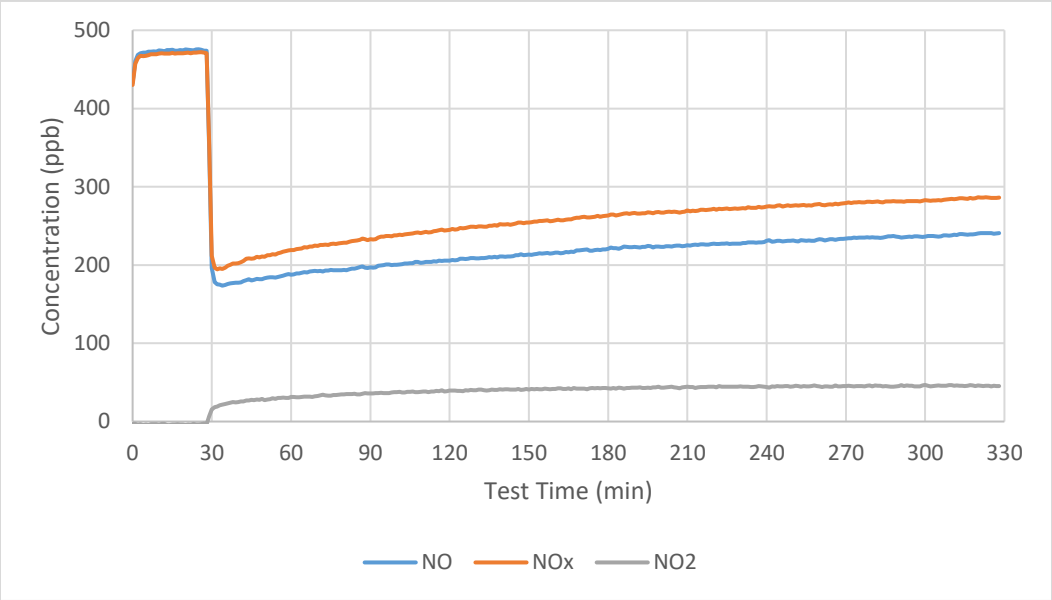

Figure A-1 Non-carbonated White TiO2, 0% SCMs (1/2)

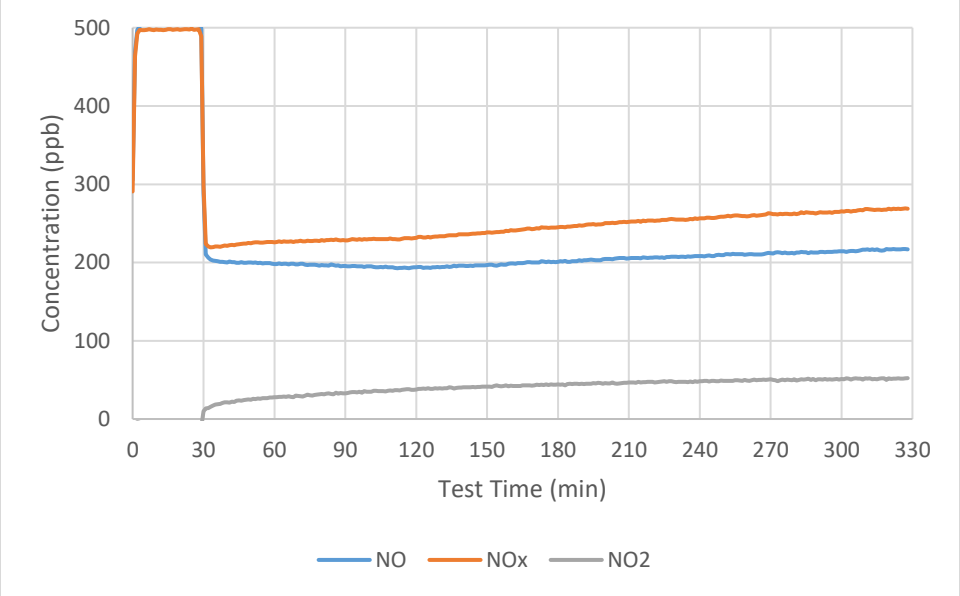

Figure A-2 Non-carbonated White TiO_2, 0% SCMs (2/2)

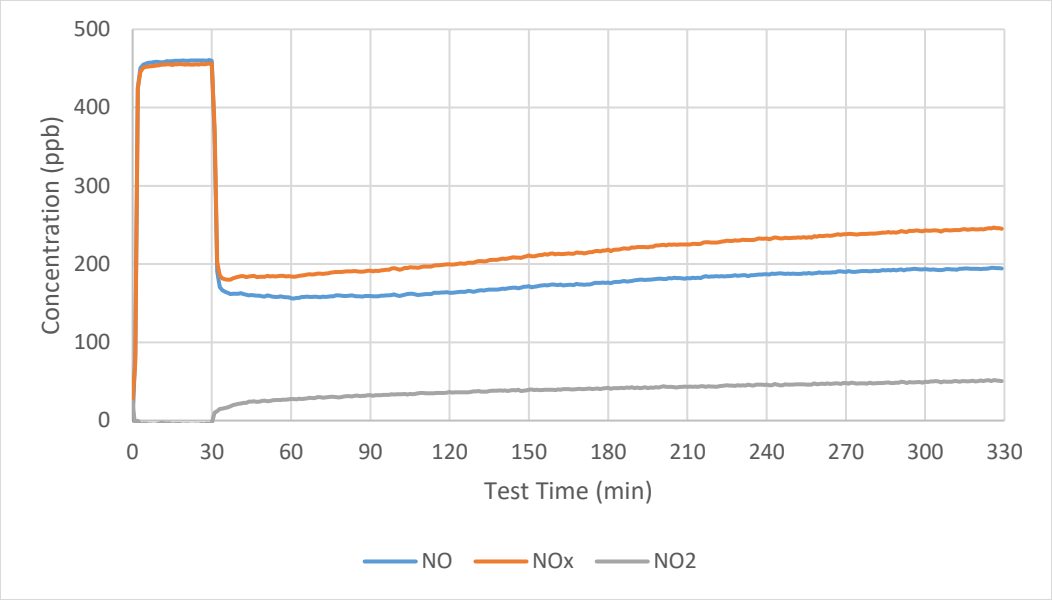

Figure A-3 Non-carbonated White TiO_2, 15% Fly Ash (1/2)

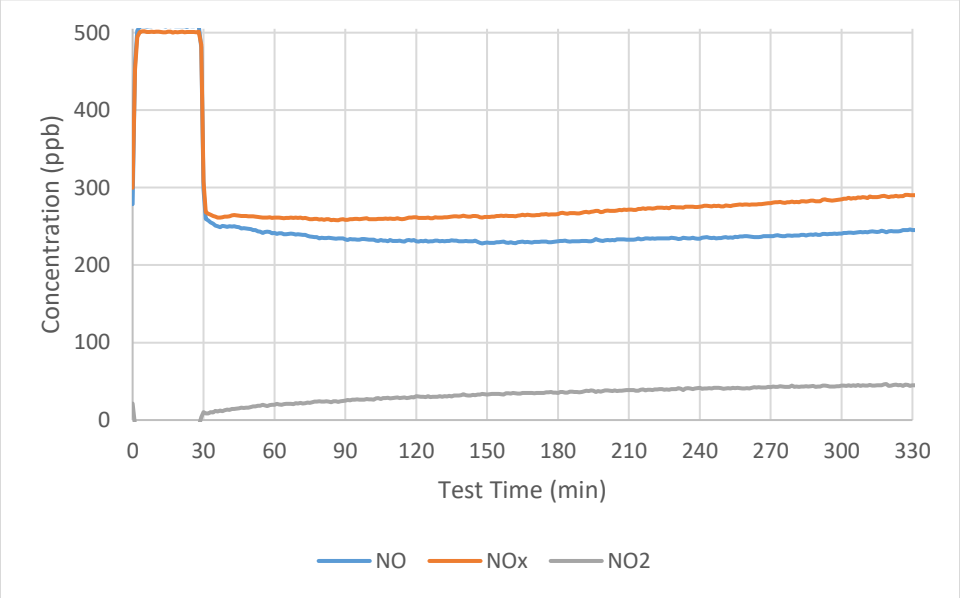

Figure A-4 Non-carbonated White TiO_2, 15% Fly Ash (2/2)

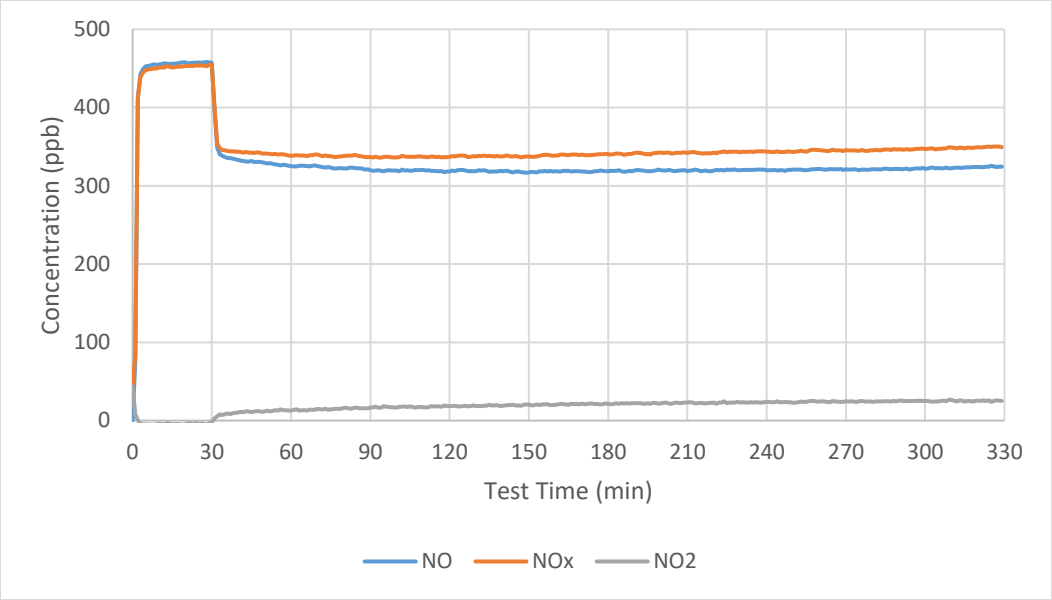

Figure A-5 Non-carbonated White TiO_2, 30% Fly Ash (1/2)

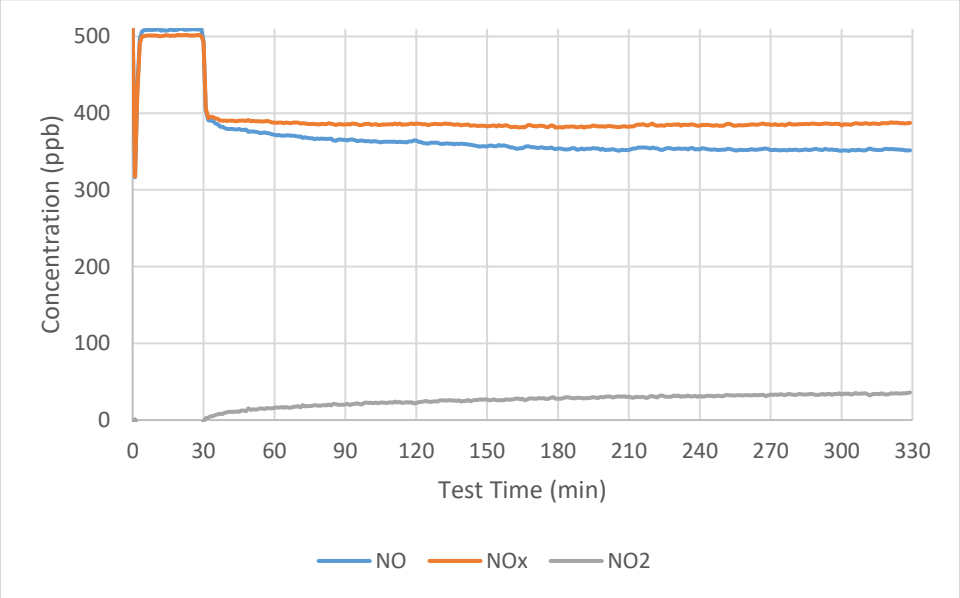

Figure A-6 Non-carbonated White TiO_2, 30% Fly Ash (2/2)

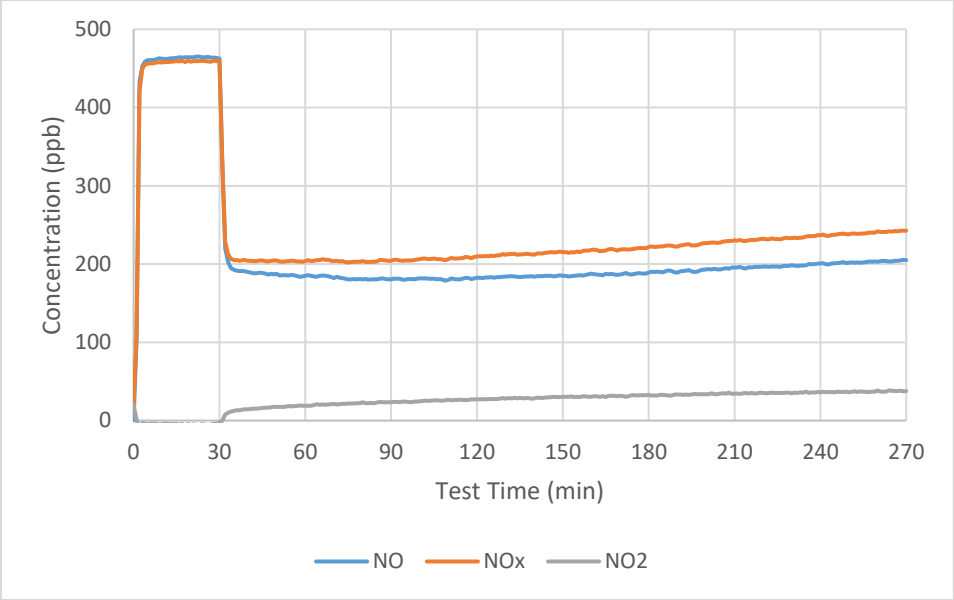

Figure A-7 Non-carbonated White TiO_2, 5% Silica Fume (1/2)

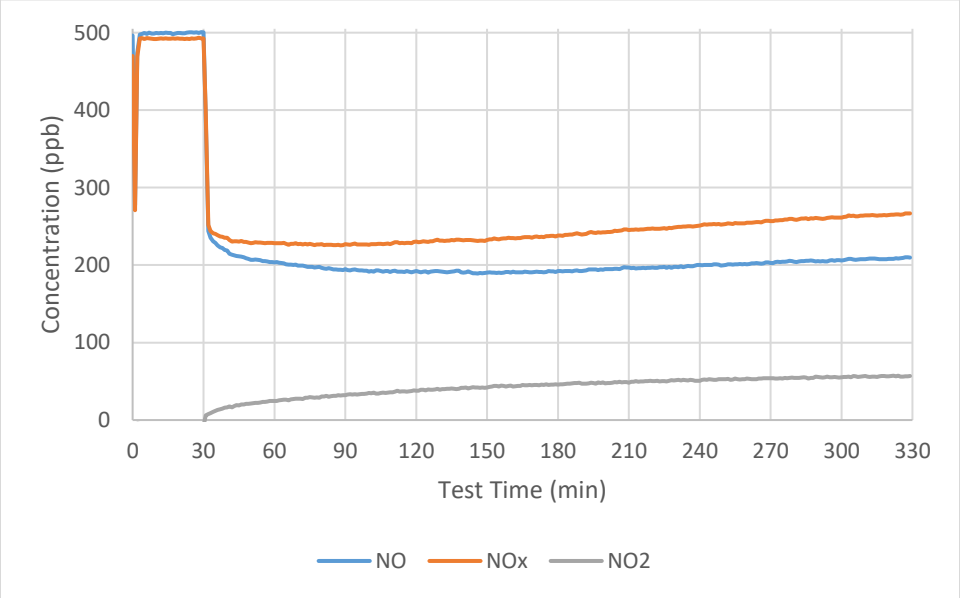

Figure A-8 Non-carbonated White TiO_2, 5% Silica Fume (2/2)

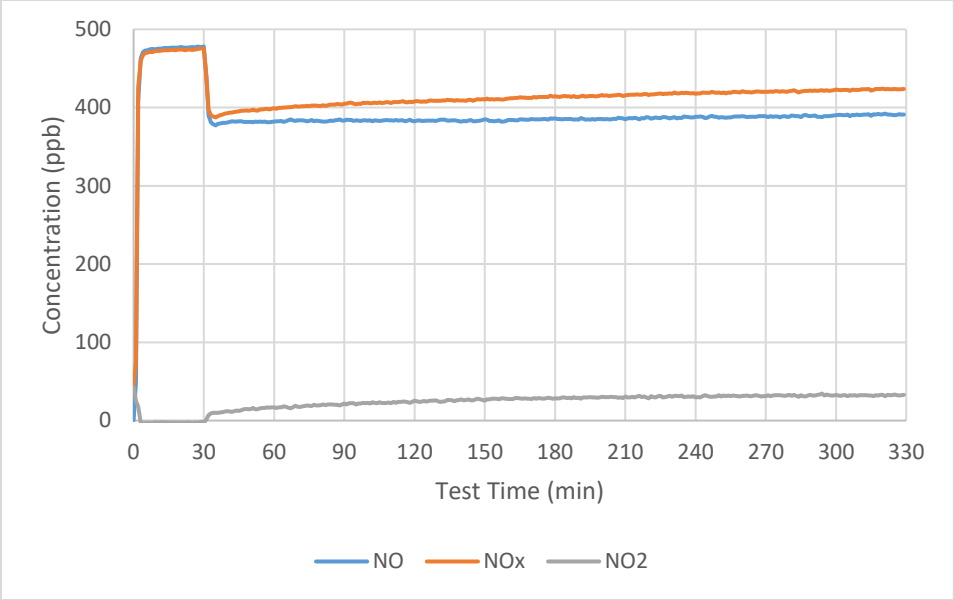

Figure A-9 Carbonated White TiO_2, 0% SCMs (1/2)

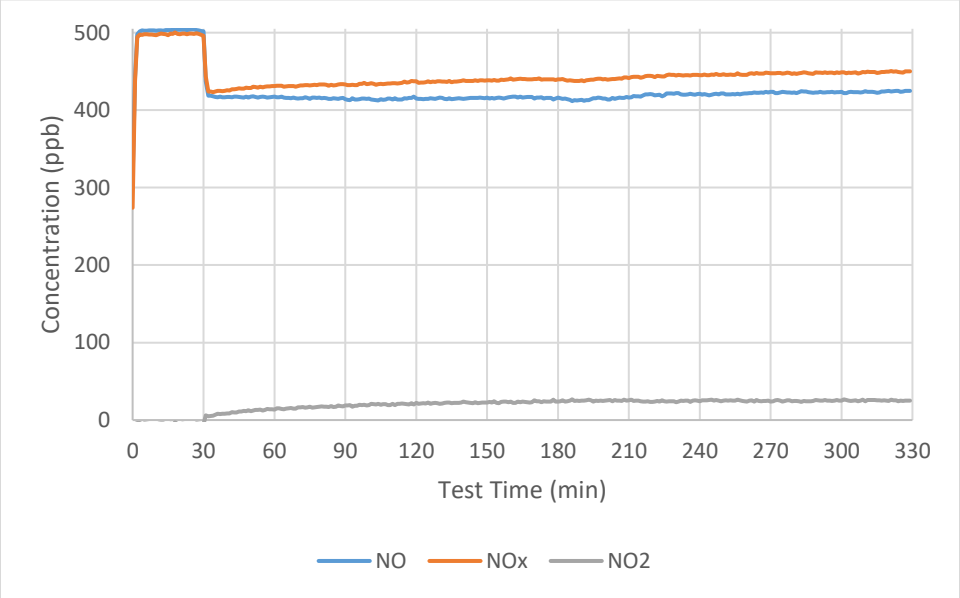

Figure A-10 Carbonated White TiO_2, 0% SCMs (2/2)

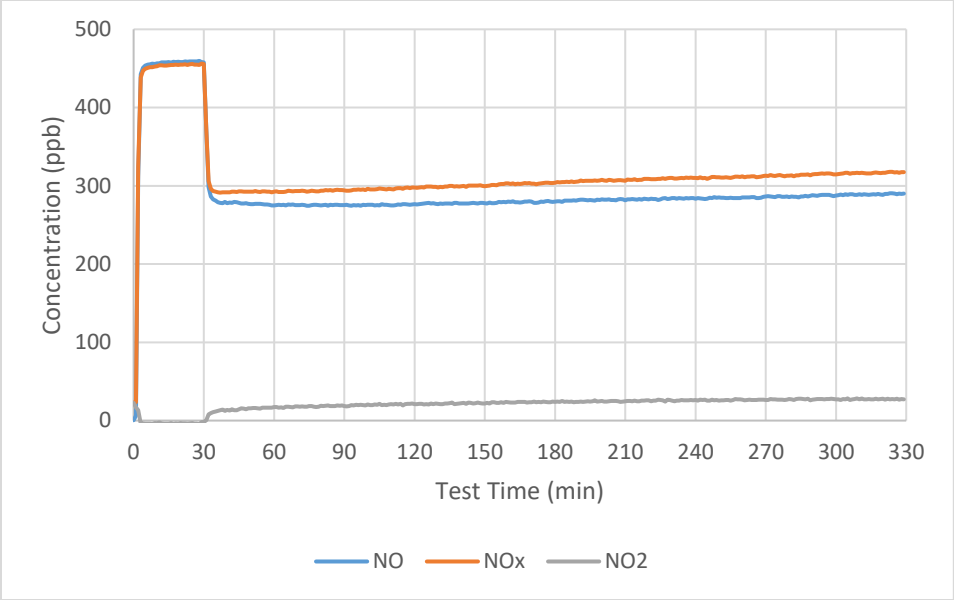

Figure A-11 Carbonated White TiO_2, 15% Fly Ash (1/2)

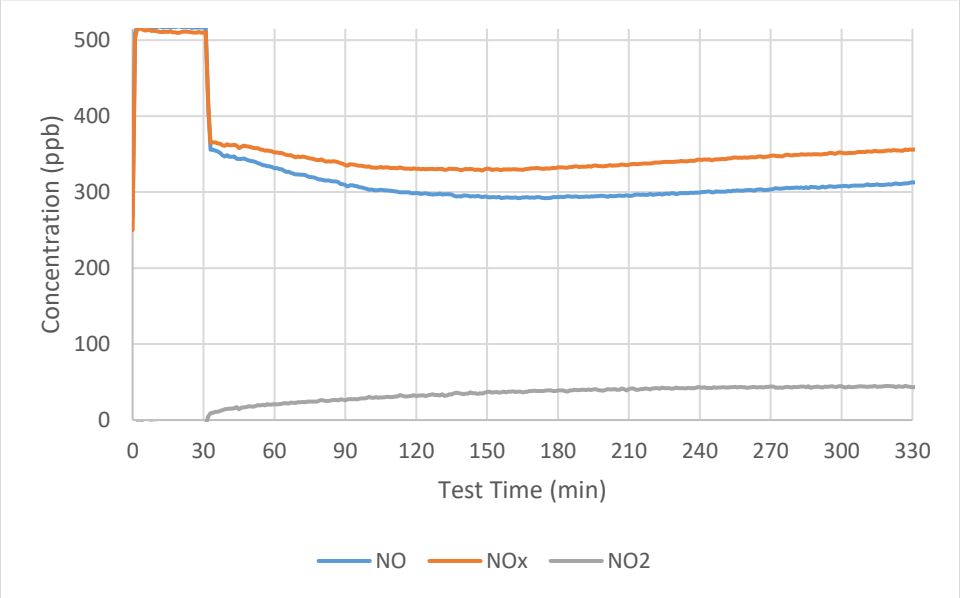

Figure A-12 Carbonated White TiO_2, 15% Fly Ash (2/2)

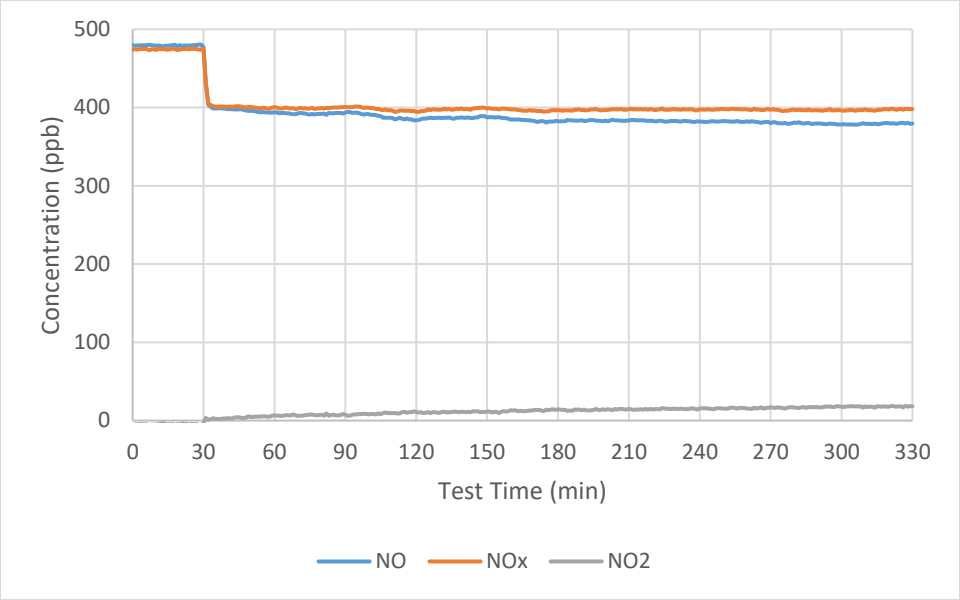

Figure A-13 Carbonated White TiO_2, 30% Fly Ash (1/3)

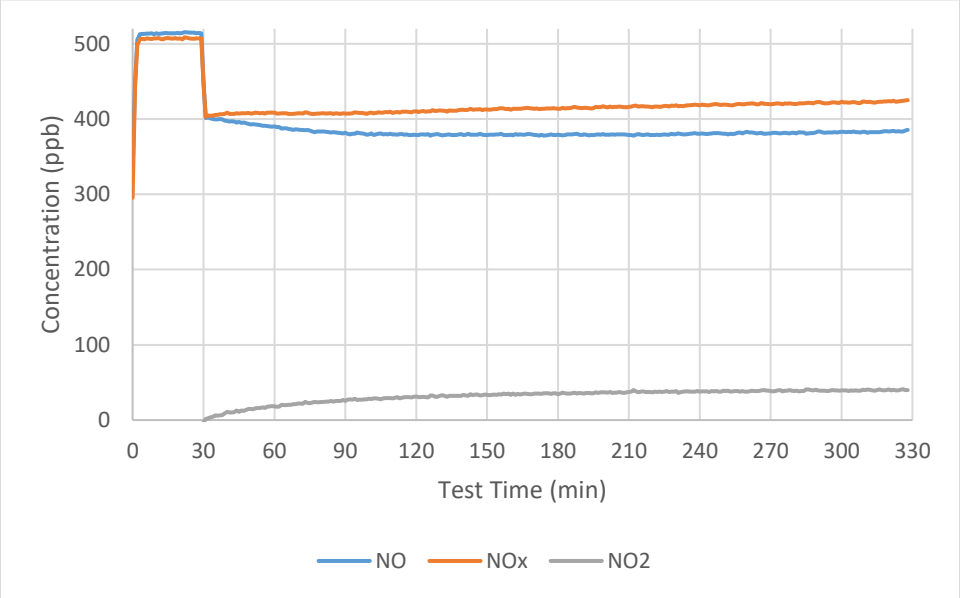

Figure A-14 Carbonated White TiO_2, 30% Fly Ash (2/3)

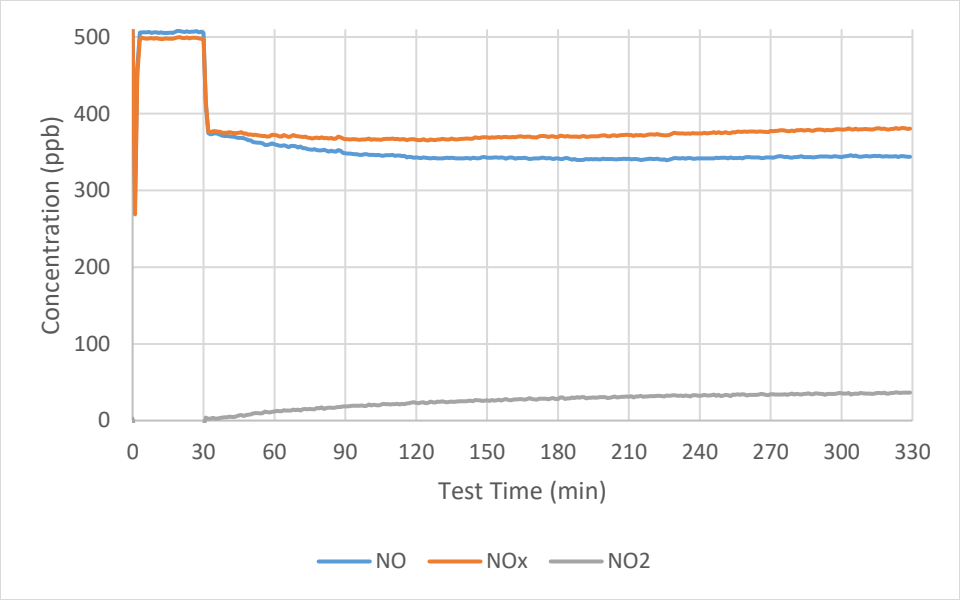

Figure A-15 Carbonated White TiO_2, 30% Fly Ash (3/3)

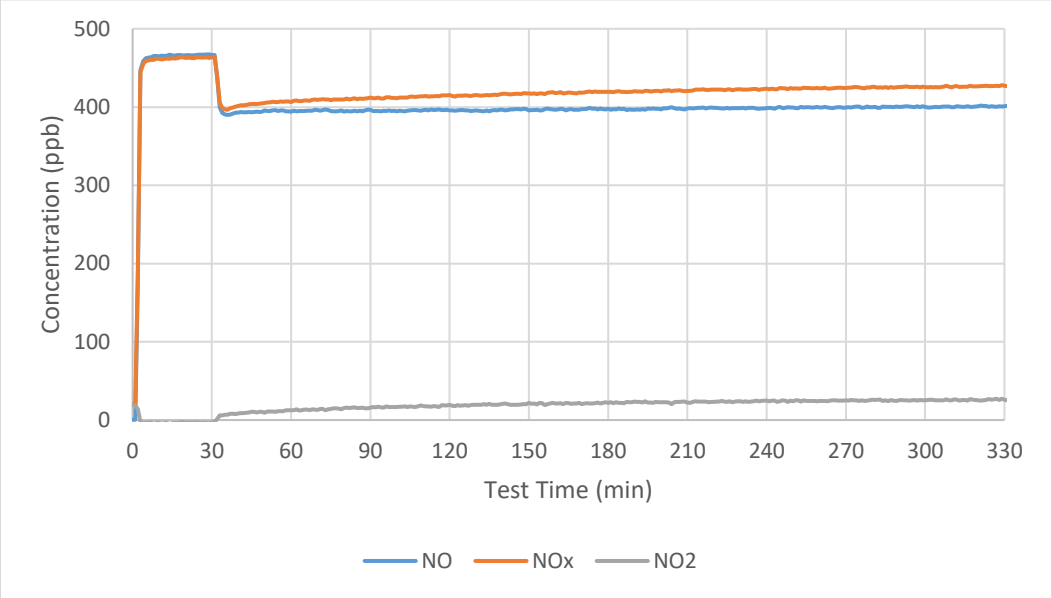

Figure A-16 Carbonated White TiO_2, 5% Silica Fume (1/2)

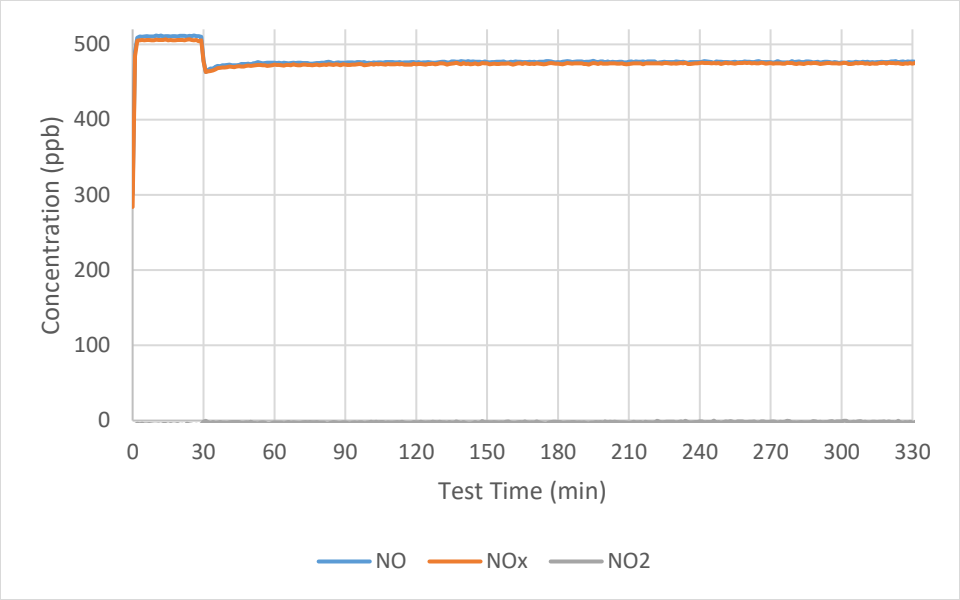

Figure A-17 Carbonated White TiO_2, 5% Silica Fume (2/2)

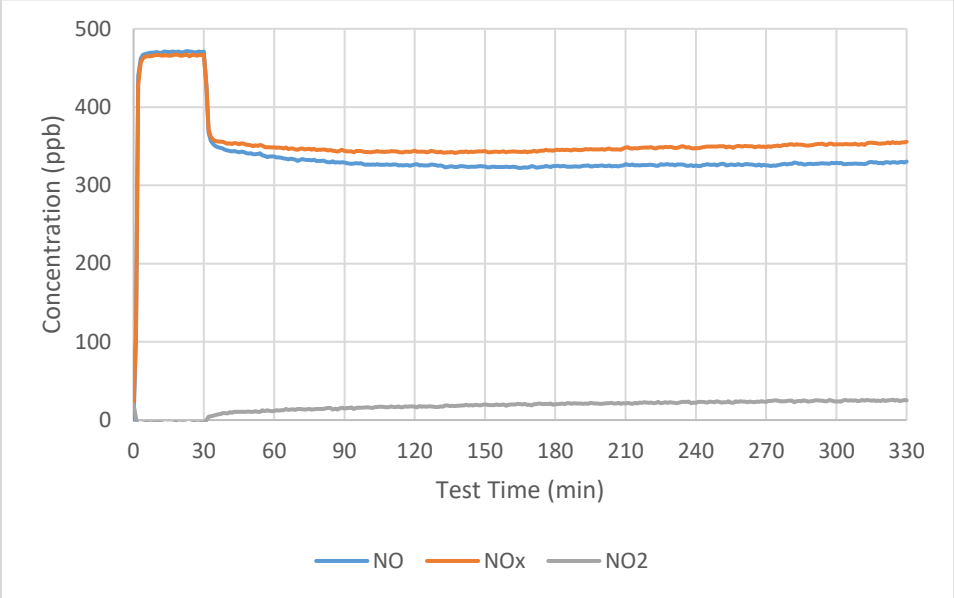

Figure A-18 Non-carbonated Gray TiO_2, 0% SCMs (1/3)

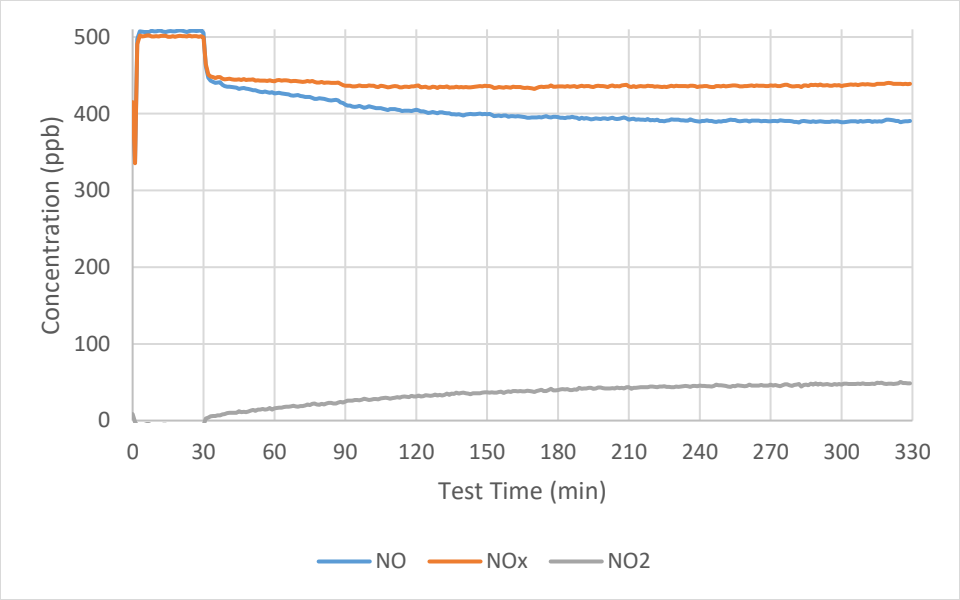

Figure A-19 Non-carbonated Gray TiO_2, 0% SCMs (2/3)

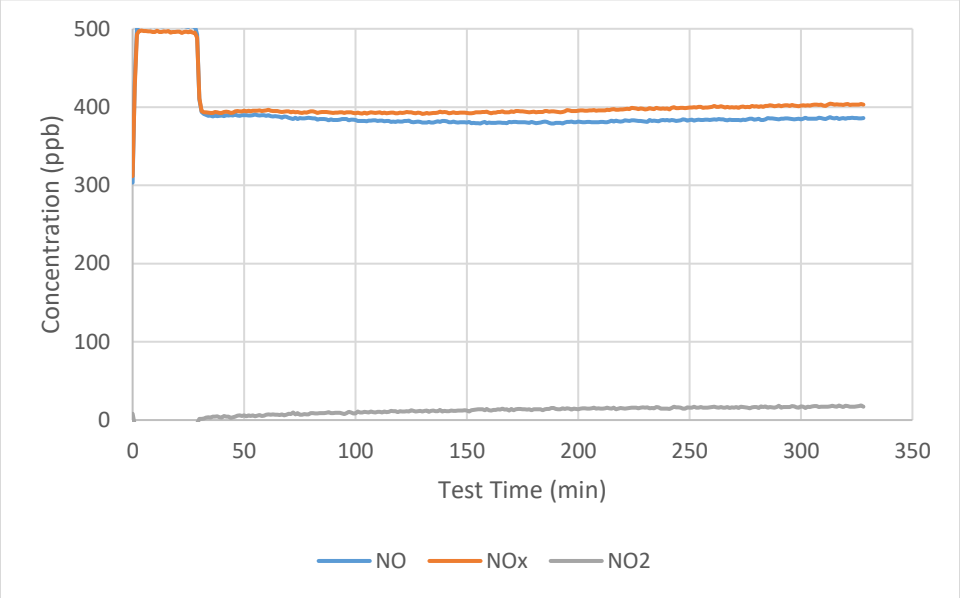

Figure A-20 Non-carbonated Gray TiO_2, 0% SCMs (3/3)

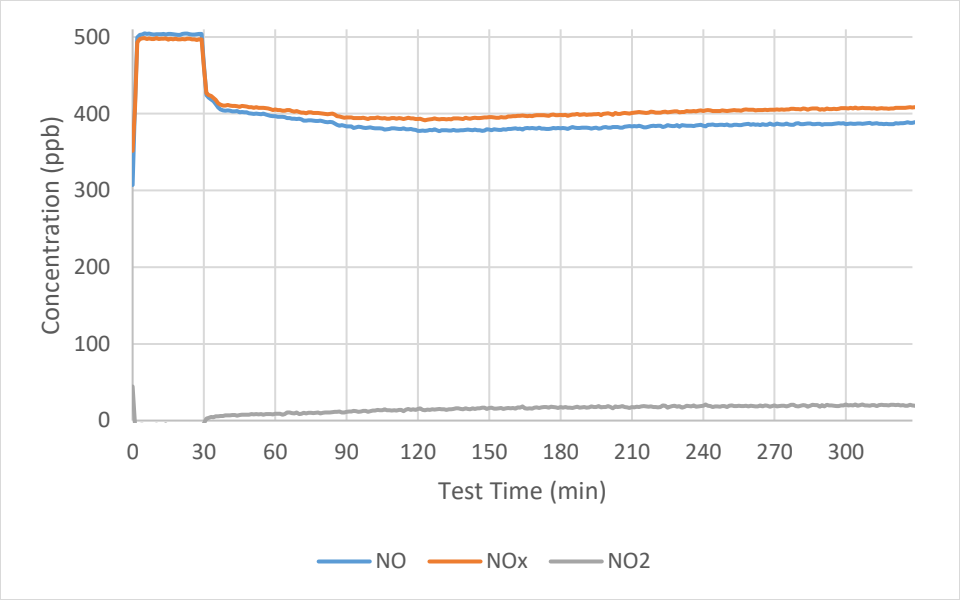

Figure A-21 Non-carbonated Gray TiO_2, 15% Fly Ash (1/2)

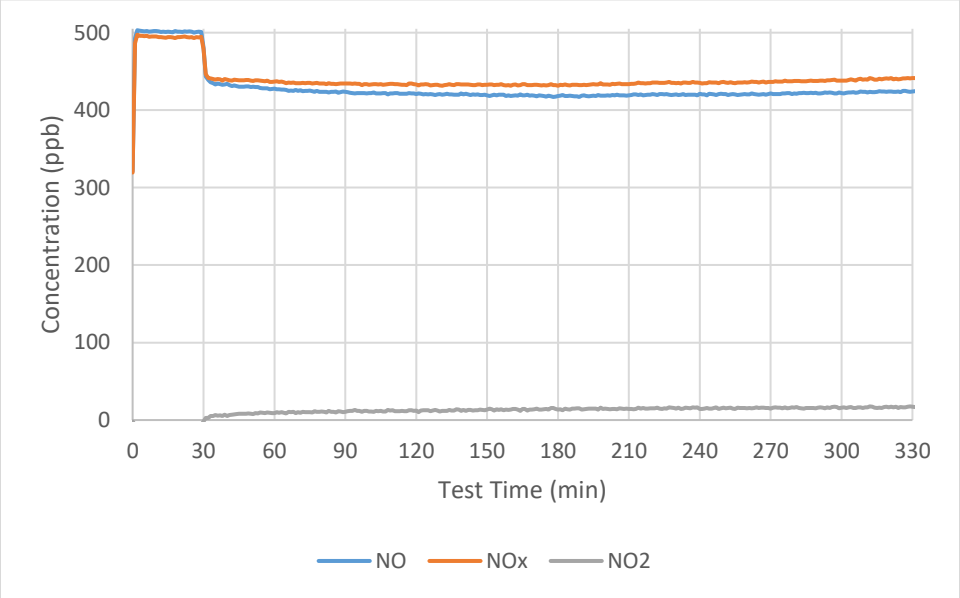

Figure A-22 Non-carbonated TiO_2 Gray, 15% Fly Ash (2/2)

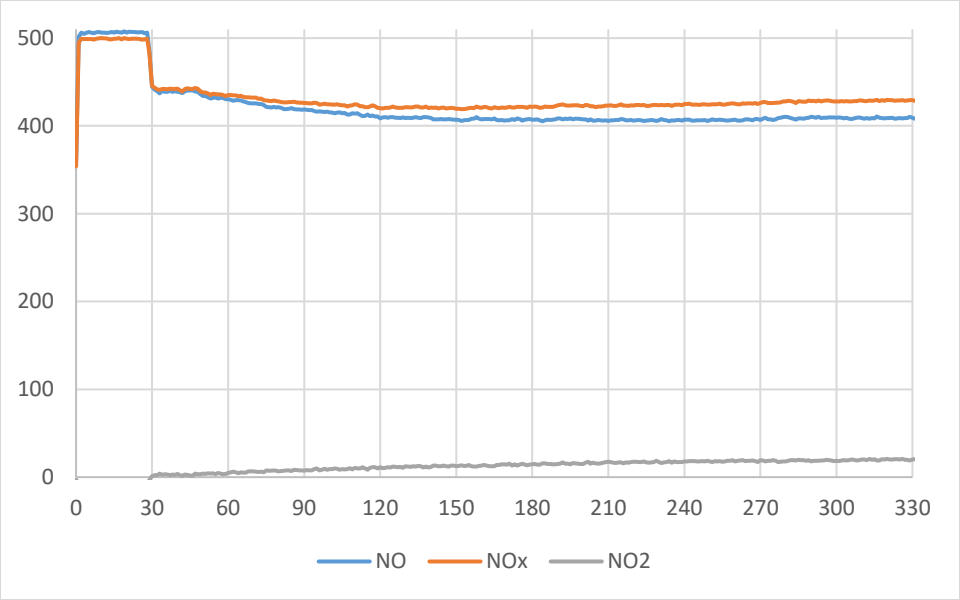

Figure A-23 Non-carbonated Gray TiO_2, 30% Fly Ash (1/2)

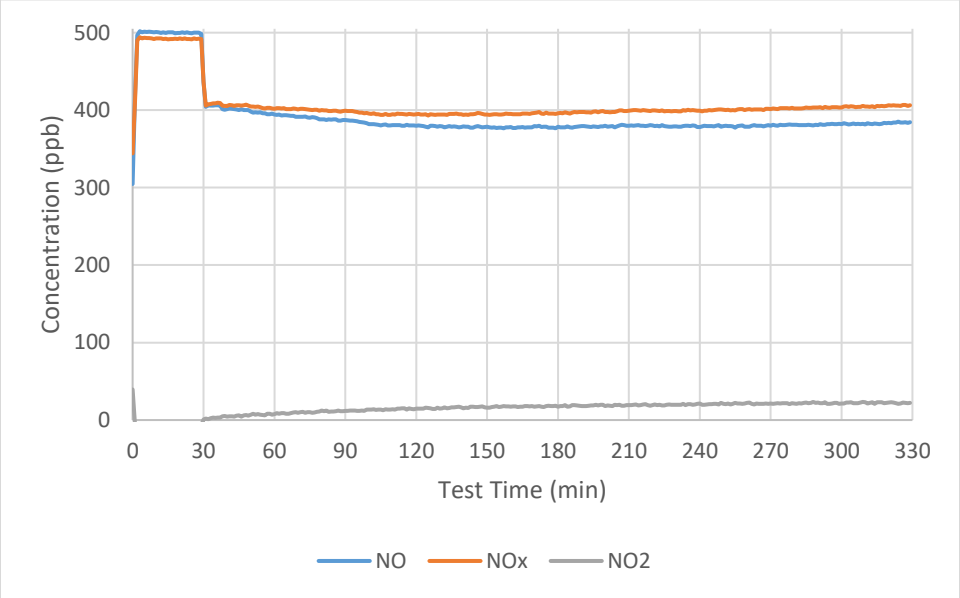

Figure A-24 Non-carbonated TiO_2 Gray, 30% Fly Ash (2/2)

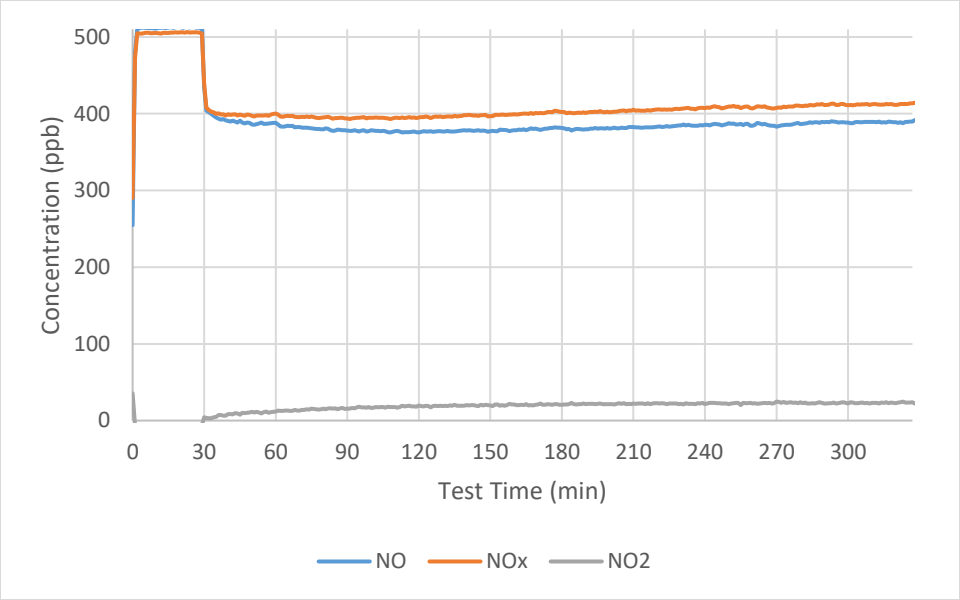

Figure A-25 Non-carbonated Gray TiO_2, 5% Silica Fume (1/2)

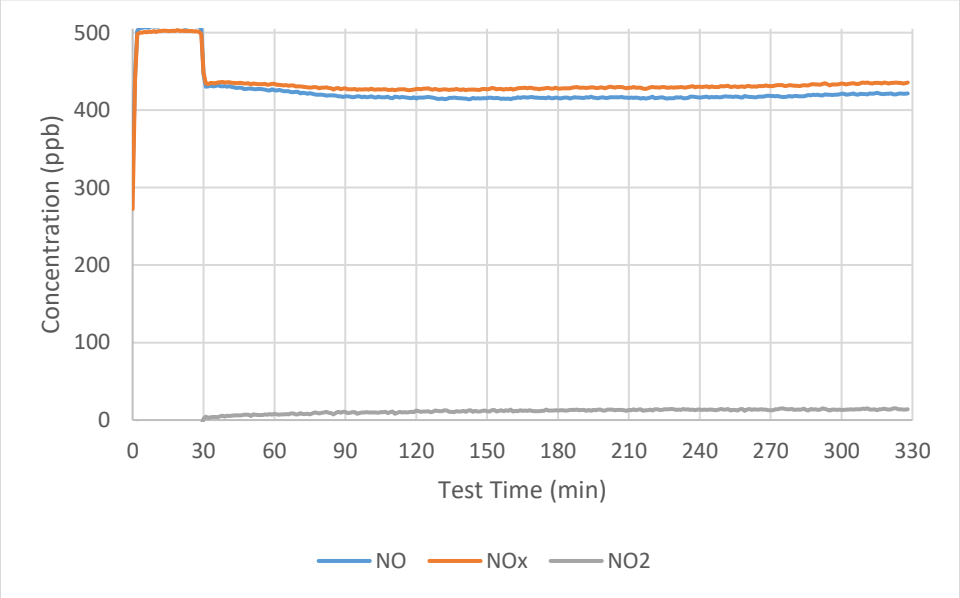

Figure A-26 Non-carbonated Gray TiO_2, 5% Silica Fume (2/2)

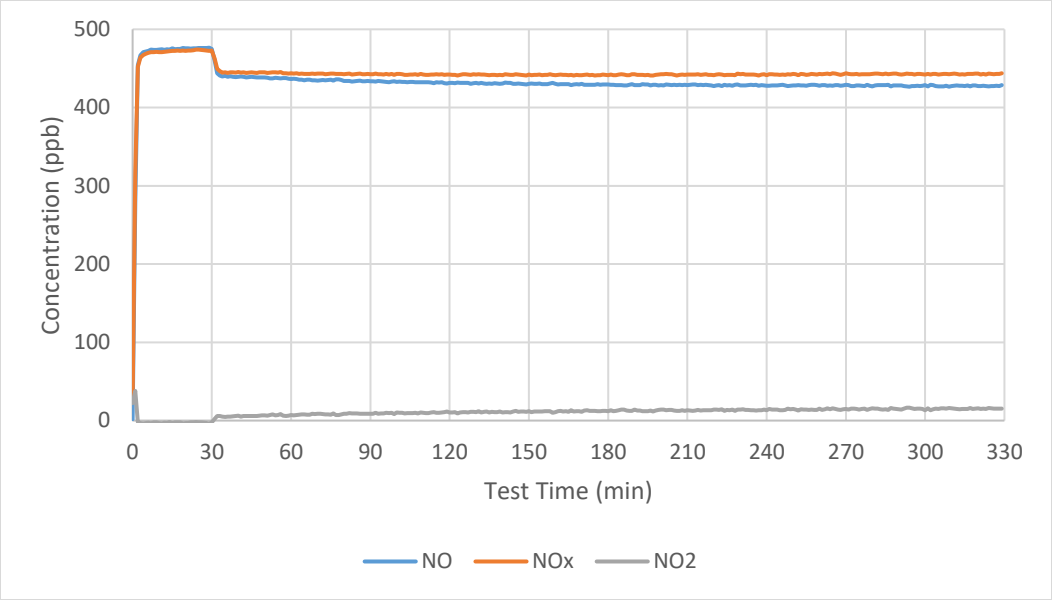

Figure A-27 Carbonated Gray TiO_2, 0% SCMs (1/2)

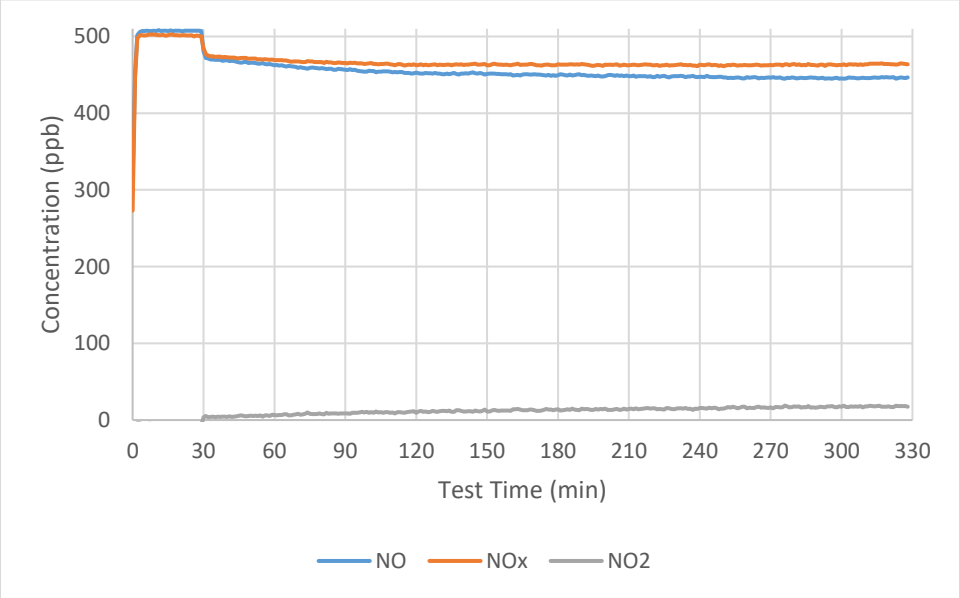

Figure A-28 Carbonated Gray TiO_2, 0% SCMs (2/2)

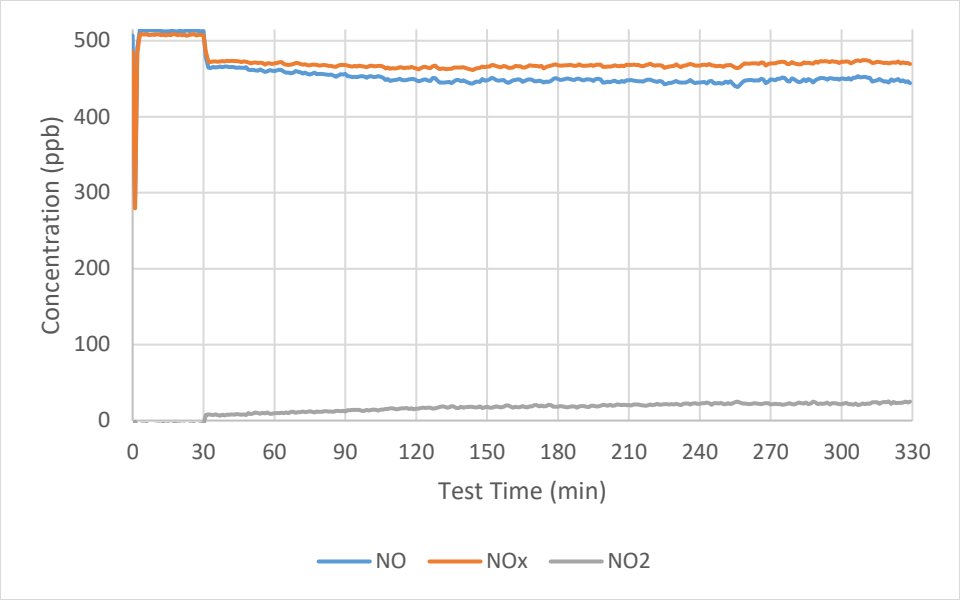

Figure A-29 Carbonated Gray TiO_2, 15% Fly Ash (1/2)

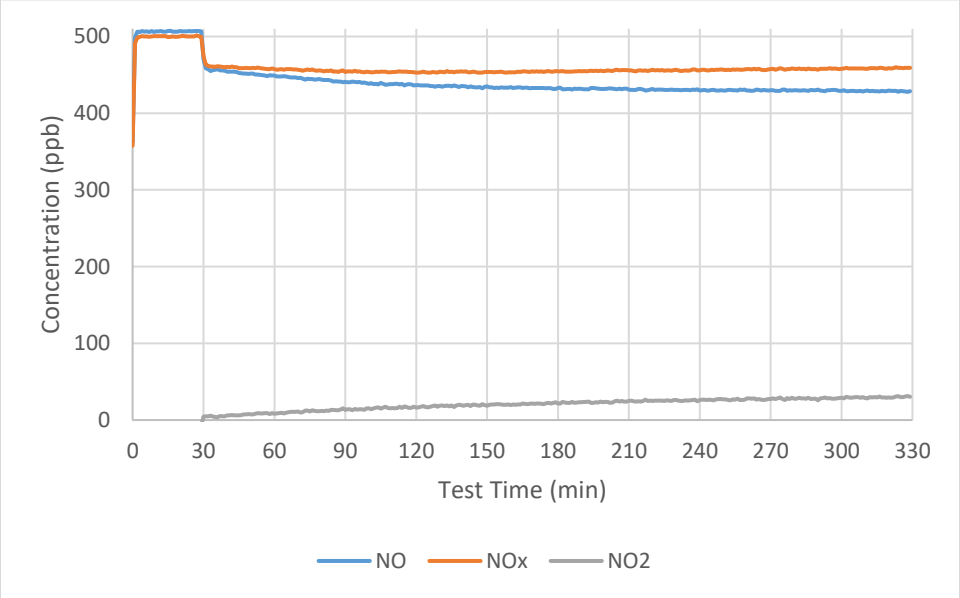

Figure A-30 Carbonated Gray TiO_2, 15% Fly Ash (2/2)

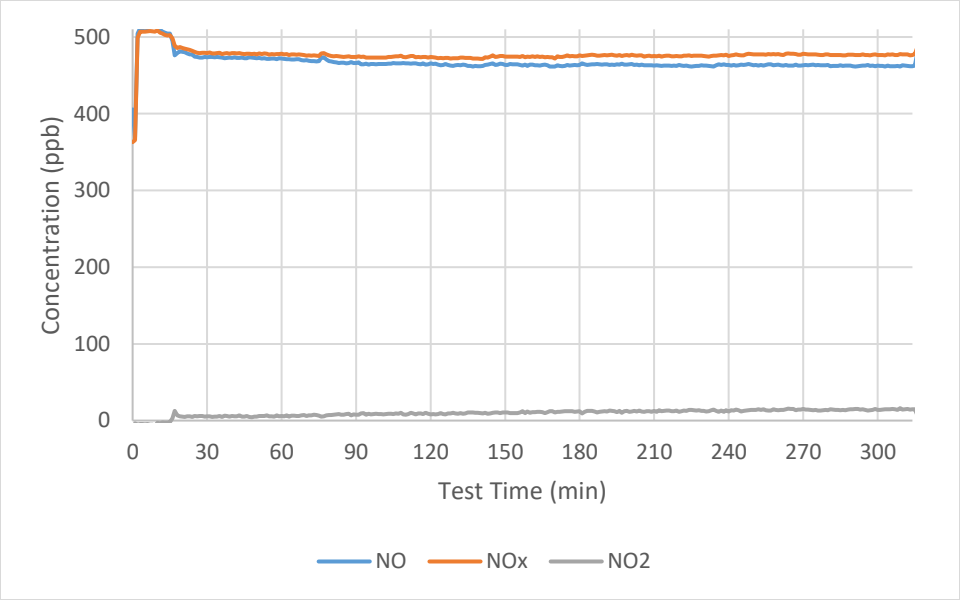

Figure A-31 Carbonated Gray TiO_2, 30% Fly Ash (1/2)

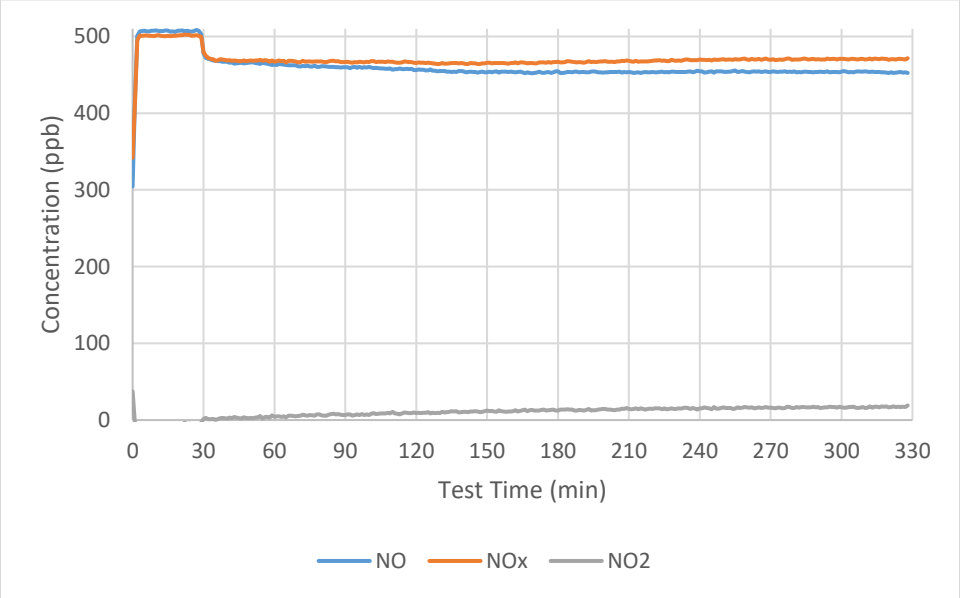

Figure A-32 Carbonated Gray TiO_2, 30% Fly Ash (2/2)

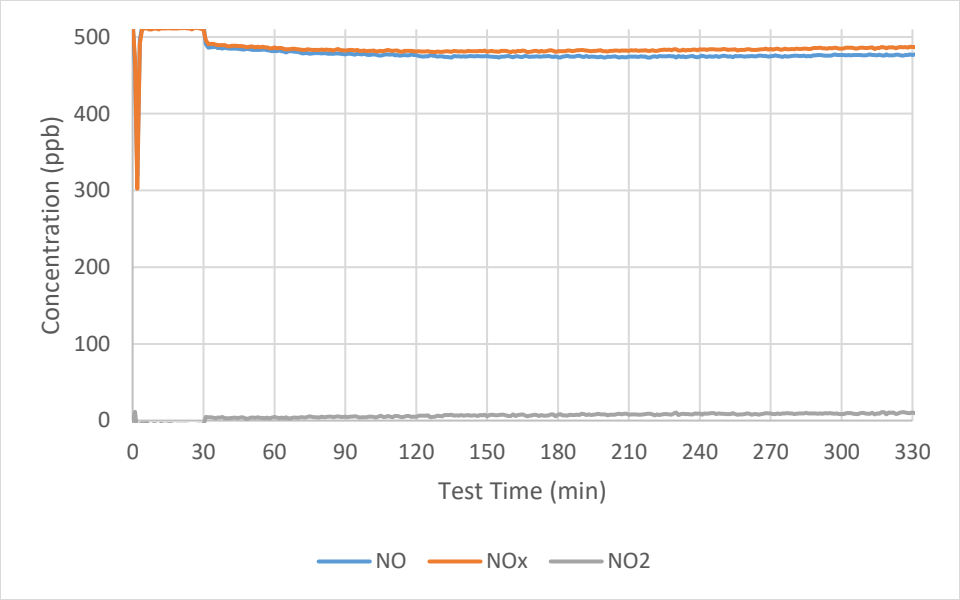

Figure A-33 Carbonated Gray TiO_2, 5% Silica Fume (1/2)

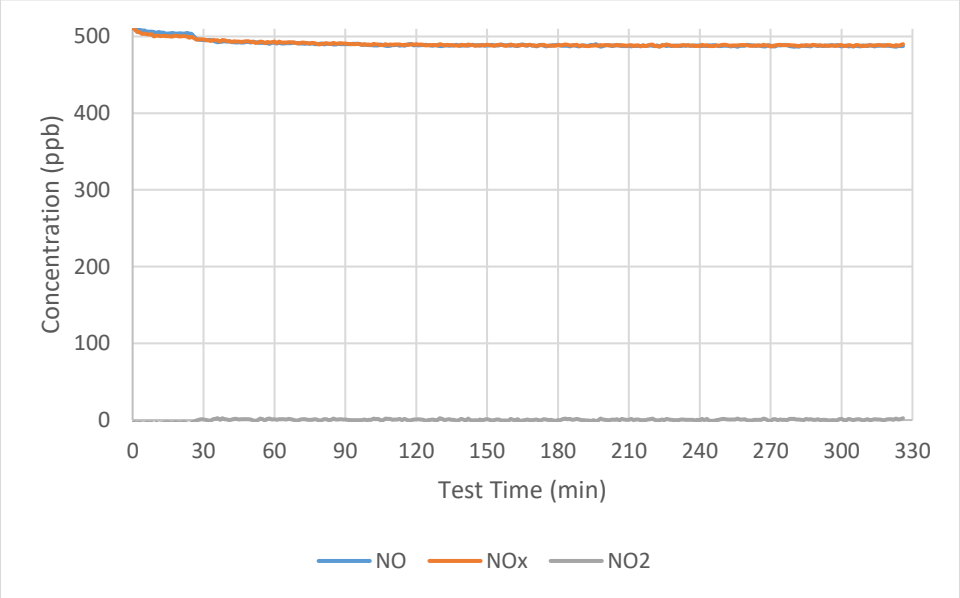

Figure A-34 Carbonated Gray TiO_2, 5% Silica Fume (2/2)

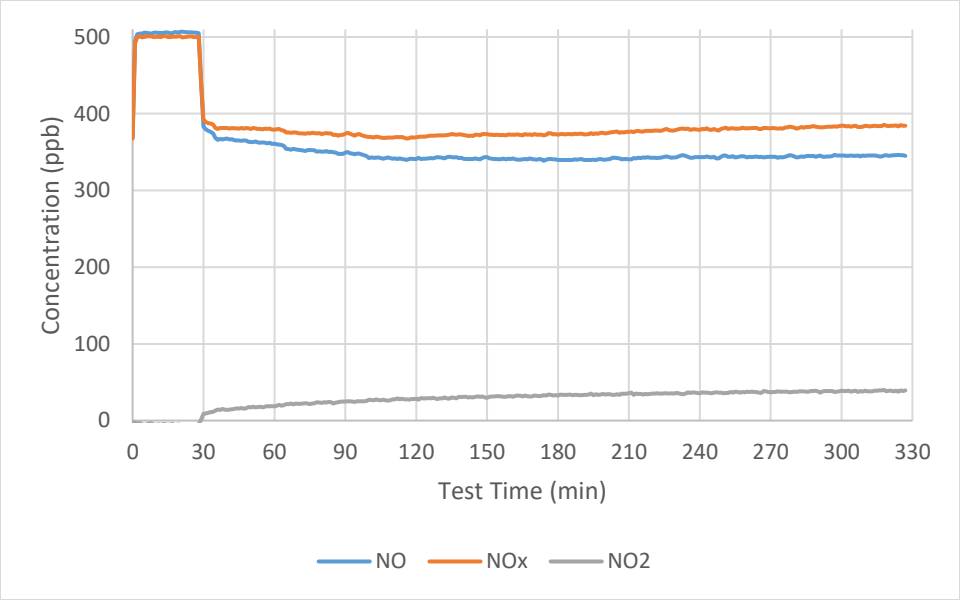

Figure A-35 Non-carbonated 2.5% Anatase, 0% SCMs (1/2)

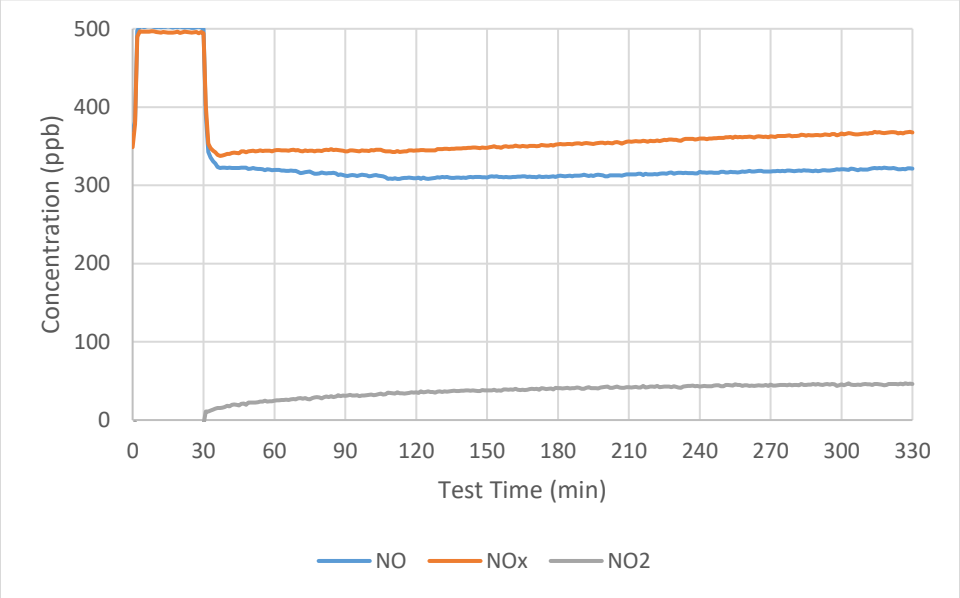

Figure A-36 Non-carbonated 2.5% Anatase, 0% SCMs (2/2)

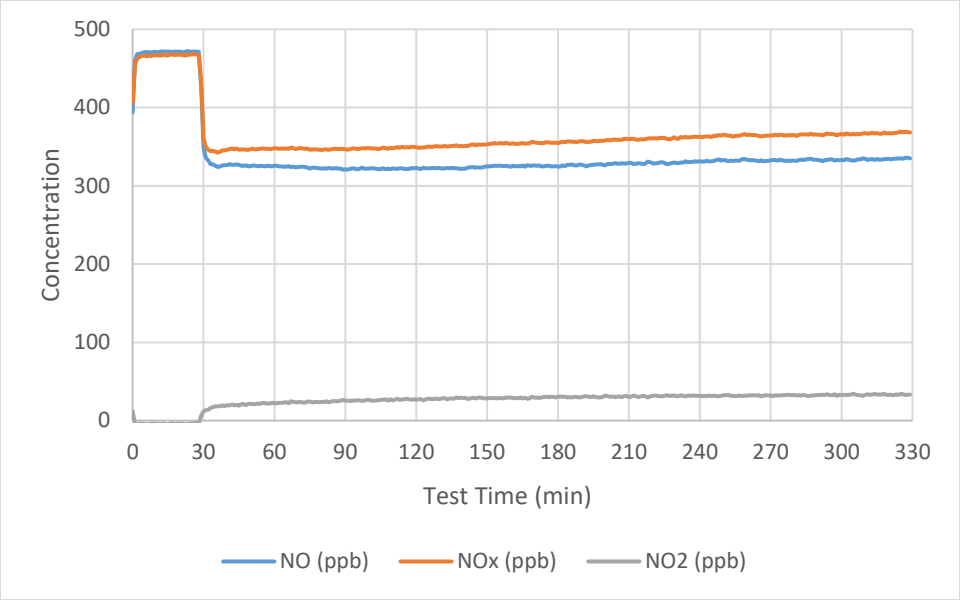

Figure A-37 Non-carbonated 5% Anatase, 0% SCMs (1/2)

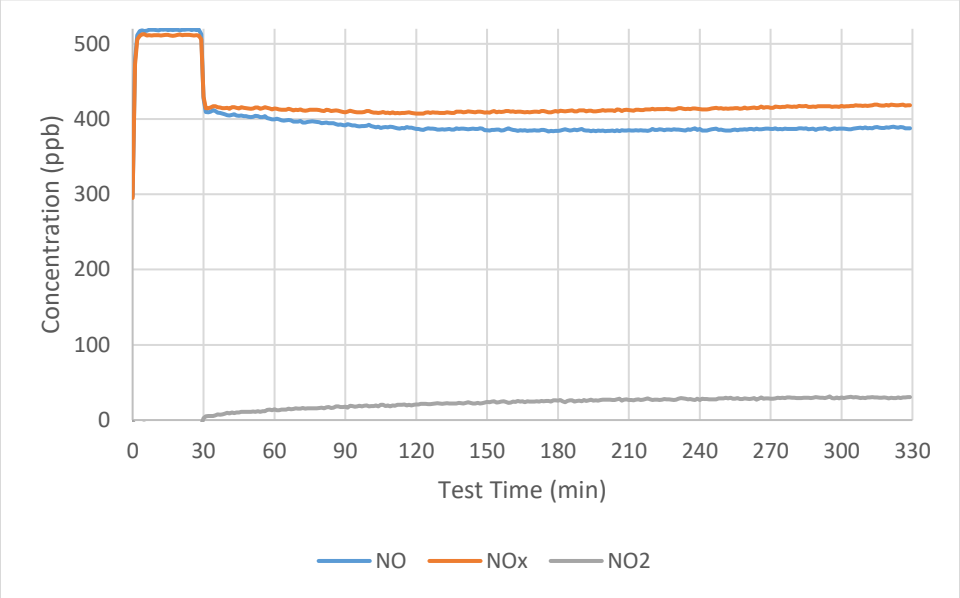

Figure A-38 Non-carbonated 5% Anatase, 0% SCMs (2/2)

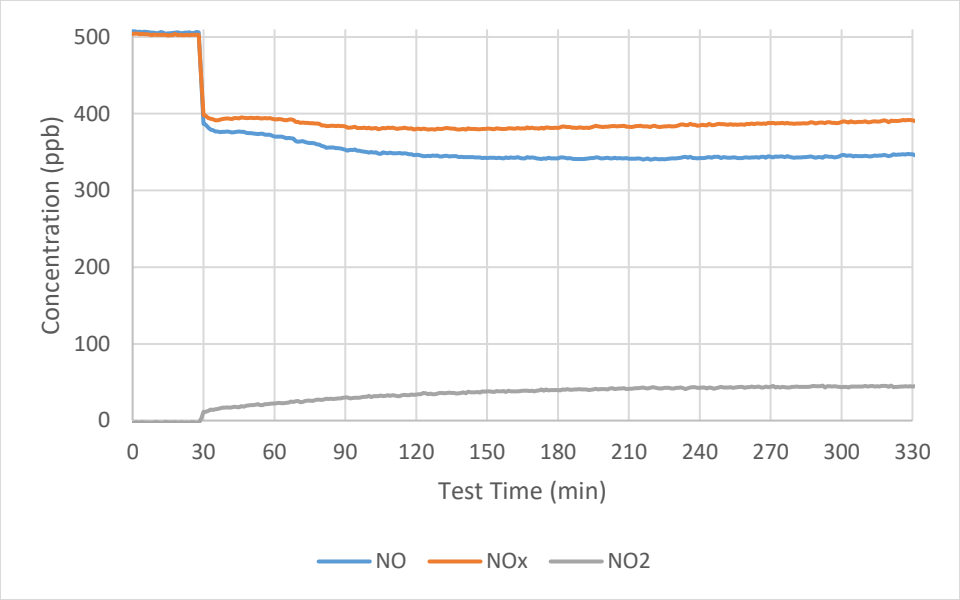

Figure A-39 Non-carbonated 10% Anatase, 0% SCMs (1/2)

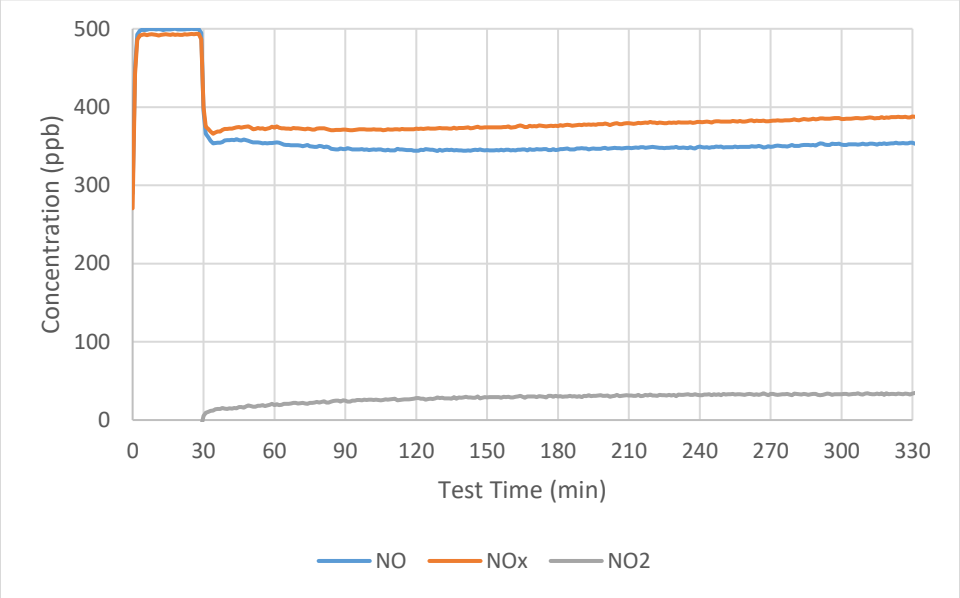

Figure A-40 Non-carbonated 10% Anatase, 0% SCMs (2/2)

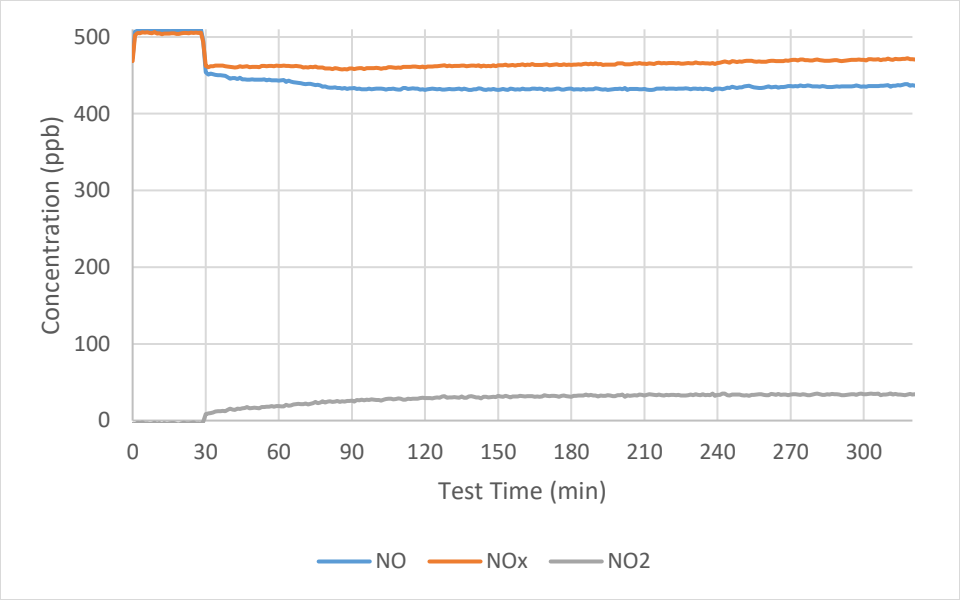

Figure A-41 Carbonated 2.5% Anatase, 0% SCMs (1/1)

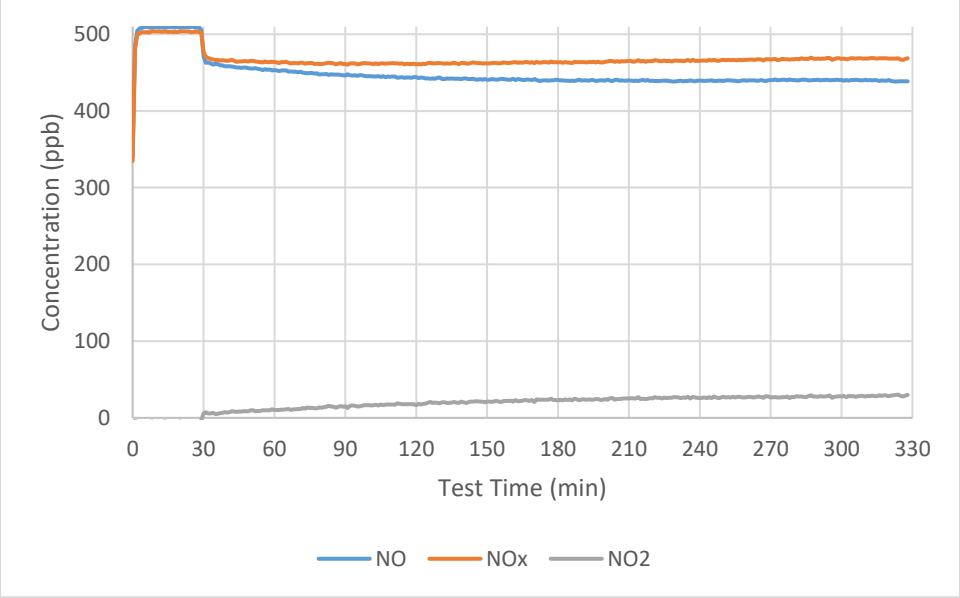

Figure A-42 Carbonated 2.5% Anatase, 0% SCMs (2/2)

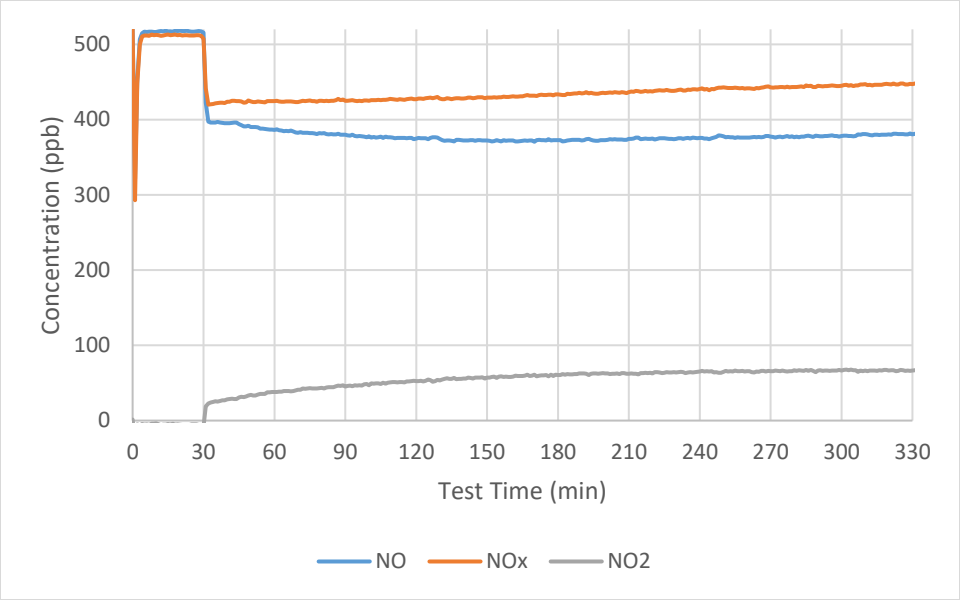

Figure A-43 Carbonated 5% Anatase, 0% SCMs (1/2)

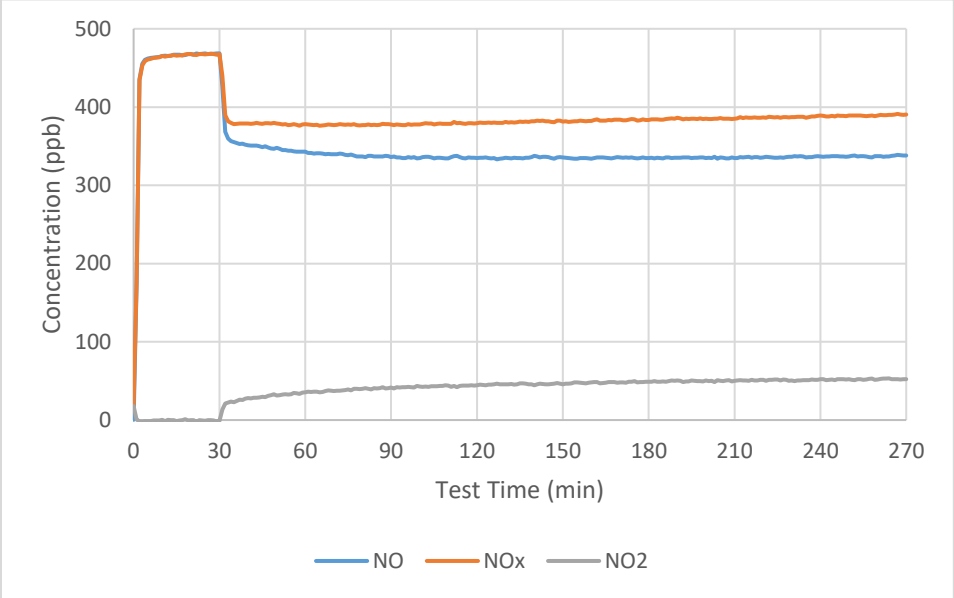

Figure A-44 Carbonated 5% Anatase, 0% SCMs (2/2)

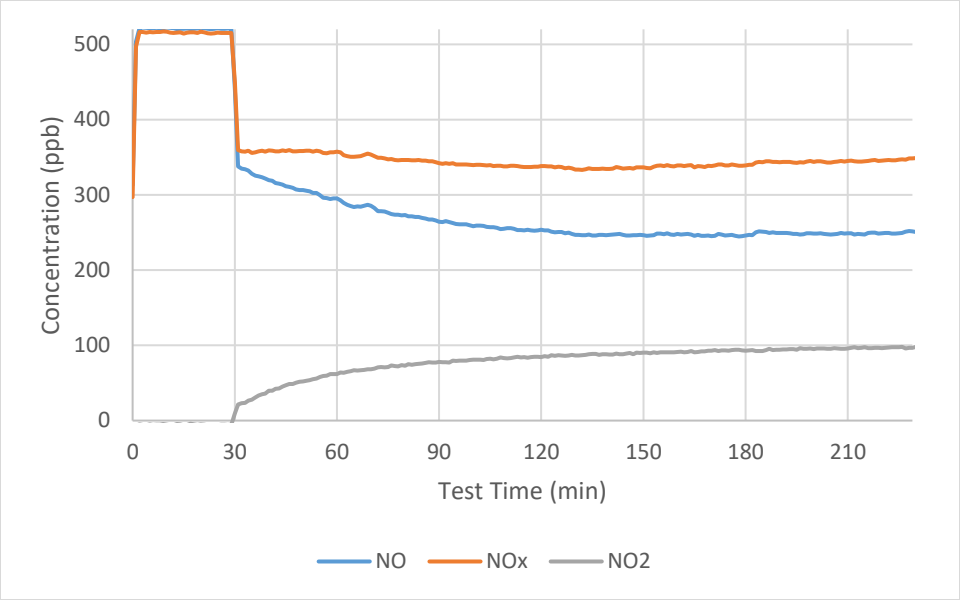

Figure A-45 Carbonated 10% Anatase, 0% SCMs (1/2)

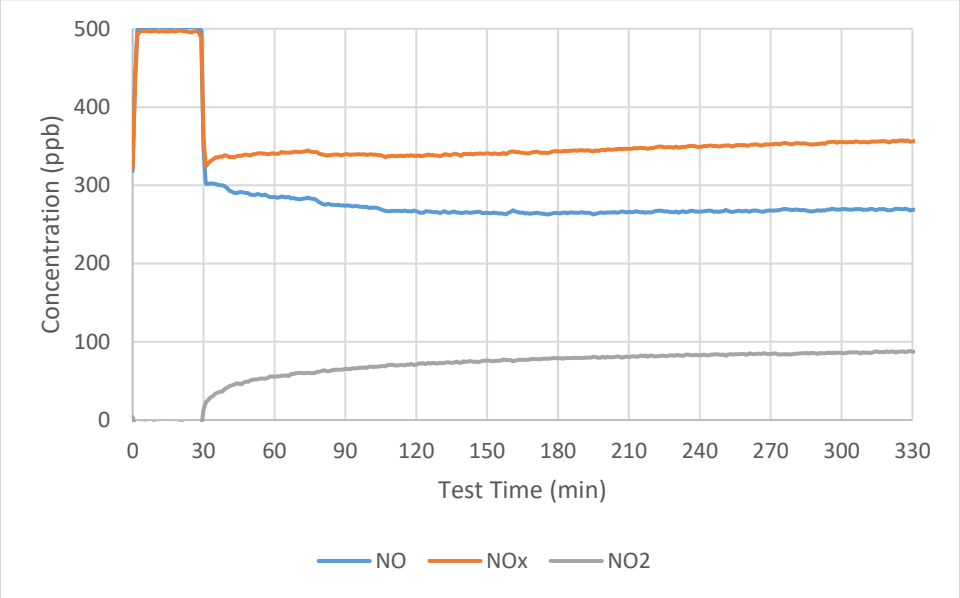

Figure A-46 Carbonated 10% Anatase, 0% SCMs (2/2)

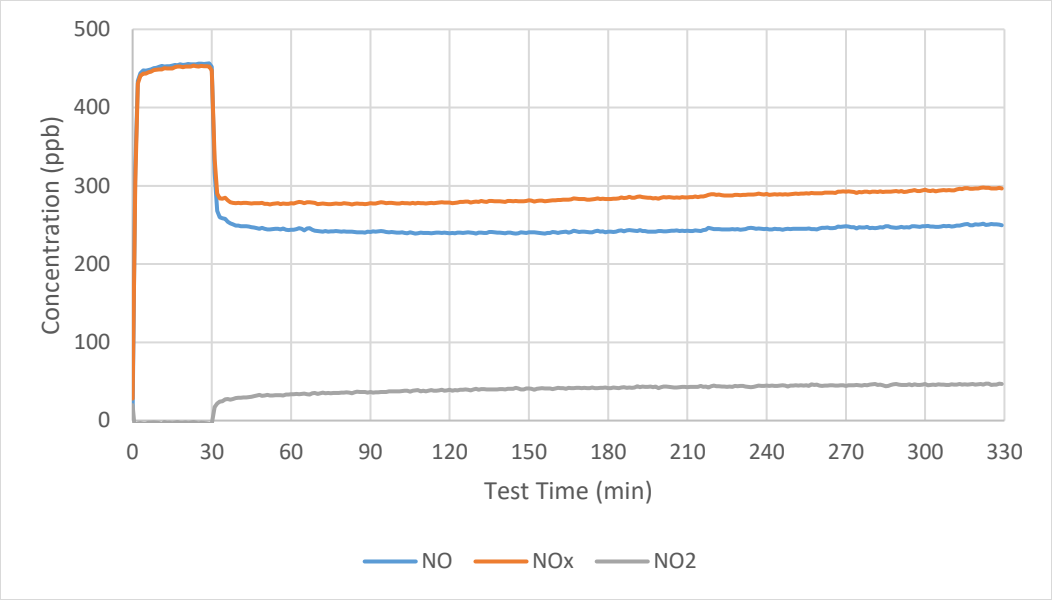

Figure A-47 Non-carbonated 5% Anatase, 15% Fly Ash (1/2)

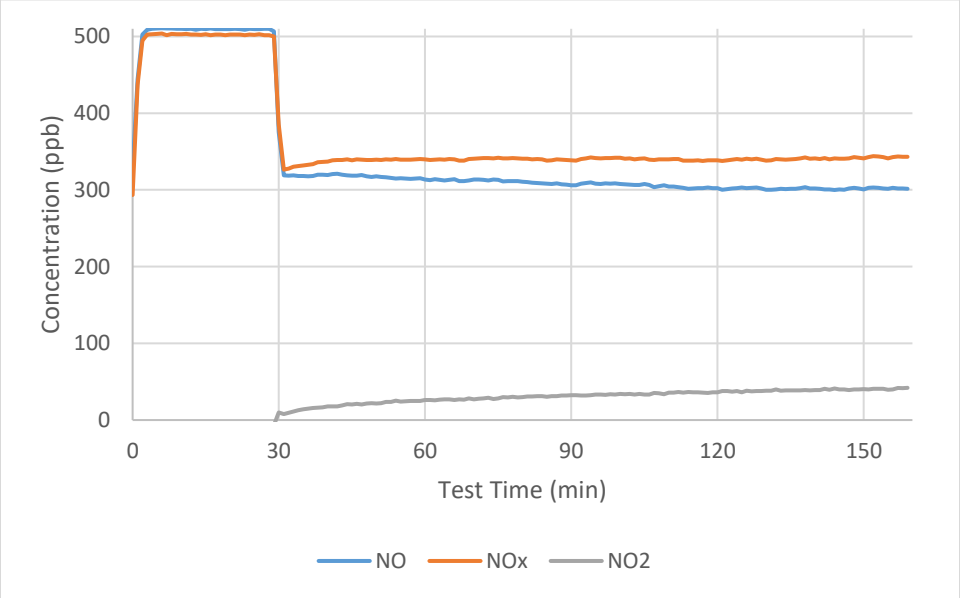

Figure A-48 Non-carbonated 5% Anatase, 15% Fly Ash (2/2)

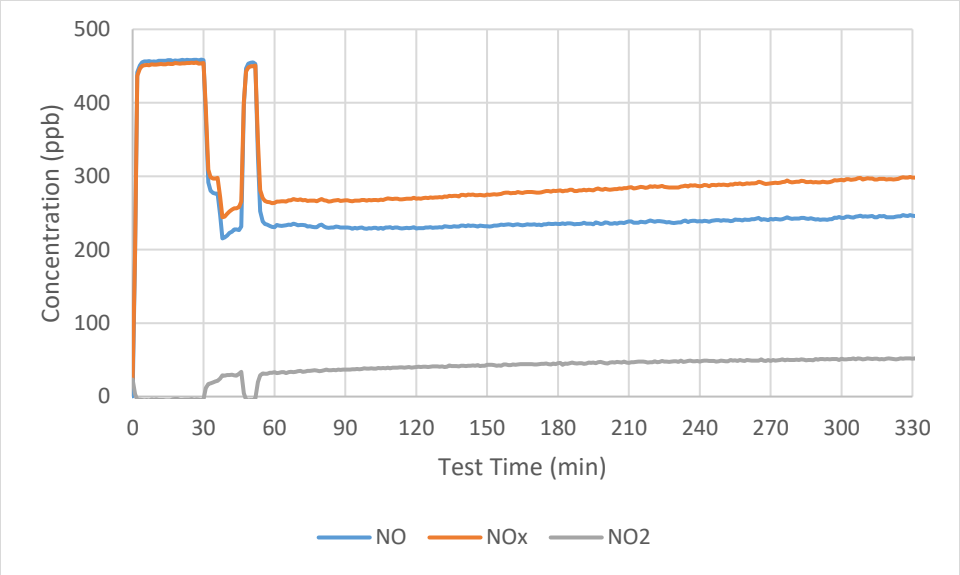

Figure A-49 Non-carbonated 5% Anatase, 30% Fly Ash (1/3)

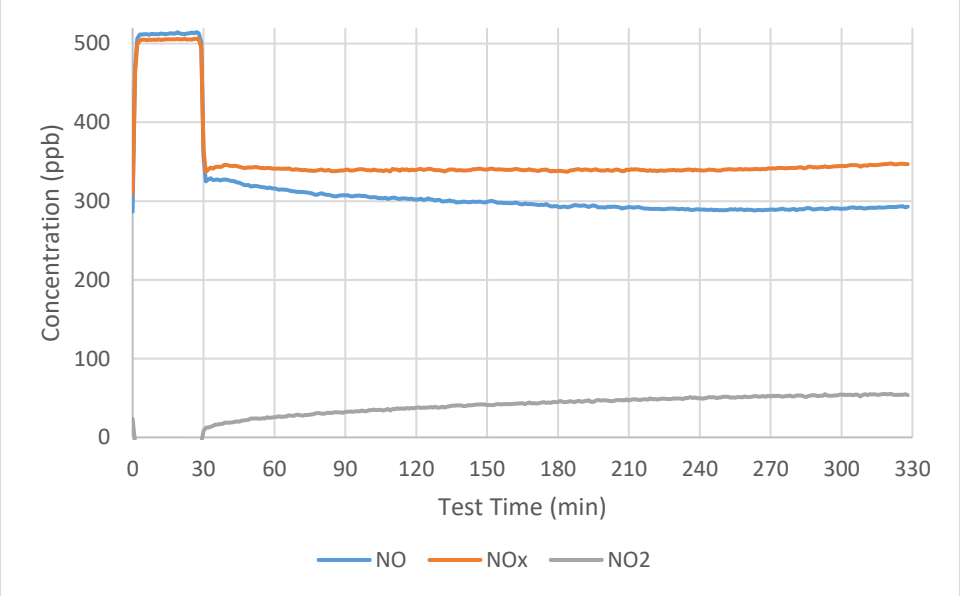

Figure A-50 Non-carbonated 5% Anatase, 30% Fly Ash (2/3)

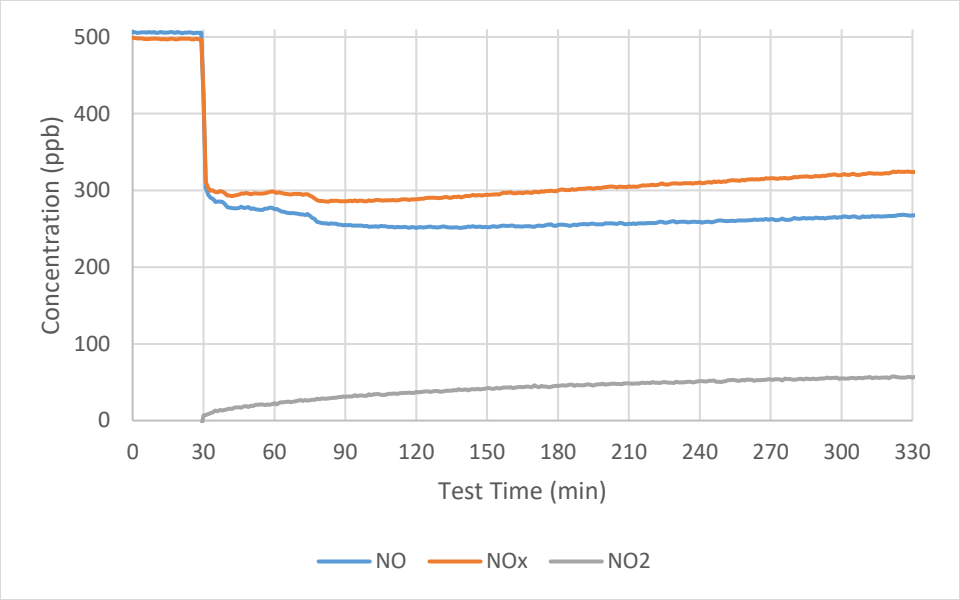

Figure A-51 Non-carbonated 5% Anatase, 30% Fly Ash (3/3)

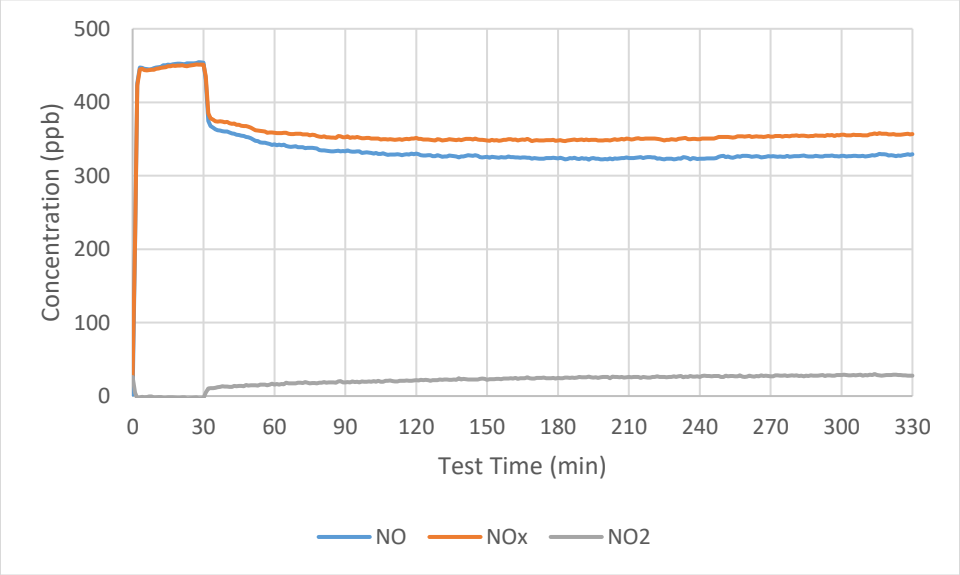

Figure A-52 Non-carbonated 5% Anatase, 5% Silica Fume (1/2)

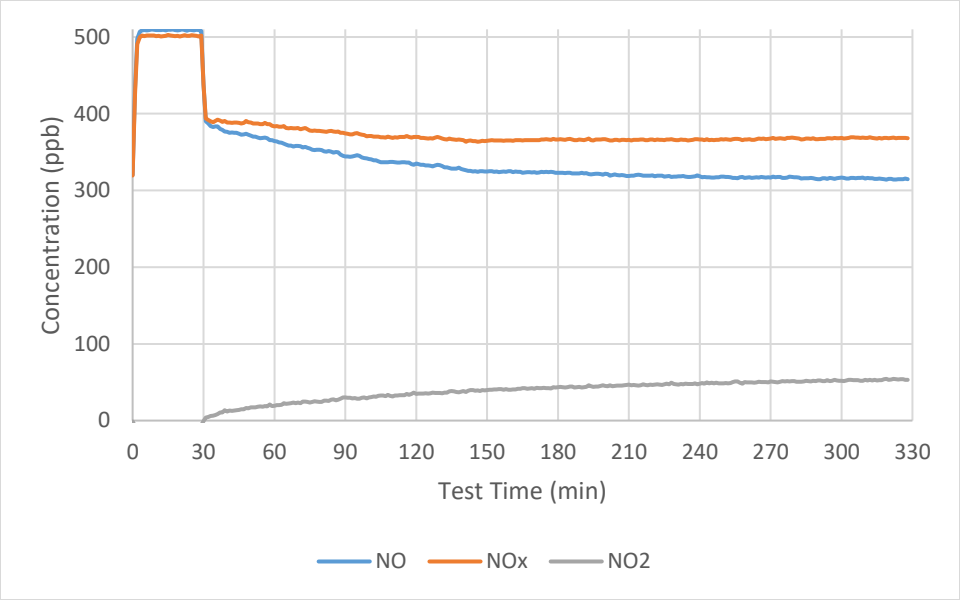

Figure A-53 Non-carbonated 5% Anatase, 5% Silica Fume (2/2)

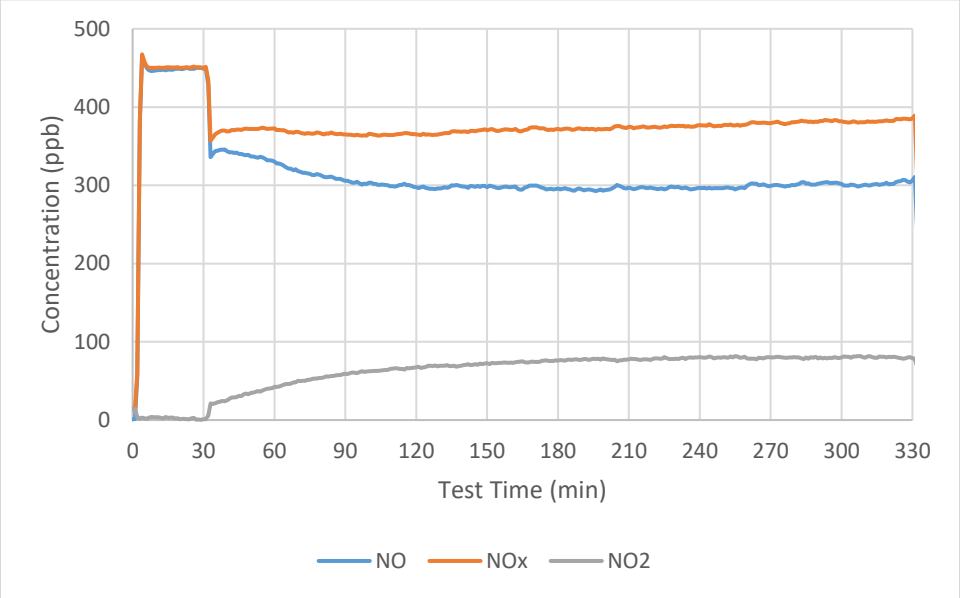

Figure A-54 Carbonated 5% Anatase, 15% Fly Ash (1/2)

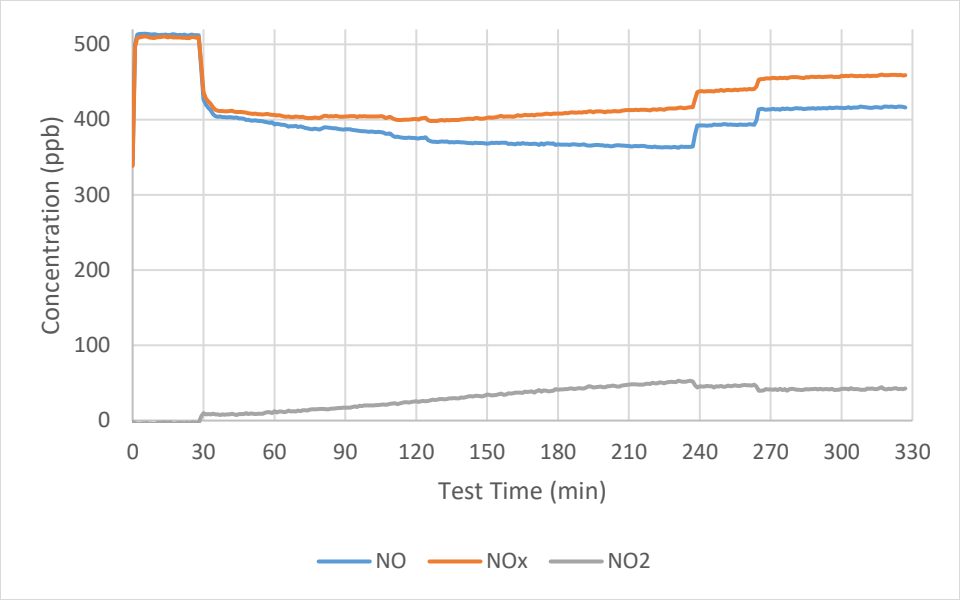

Figure A-55 Carbonated 5% Anatase, 15% Fly Ash (2/2)

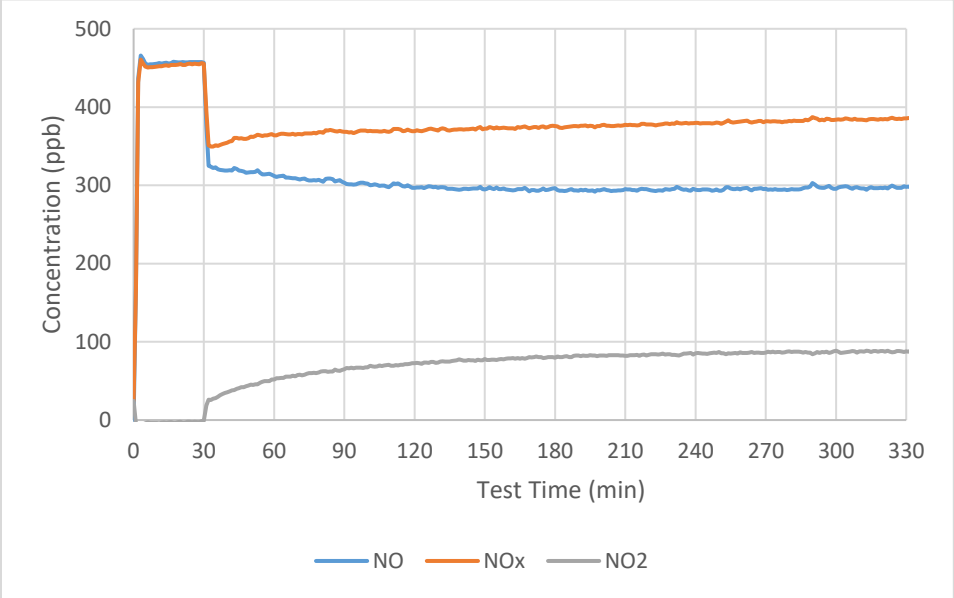

Figure A-56 Carbonated 5% Anatase, 30% Fly Ash (1/2)

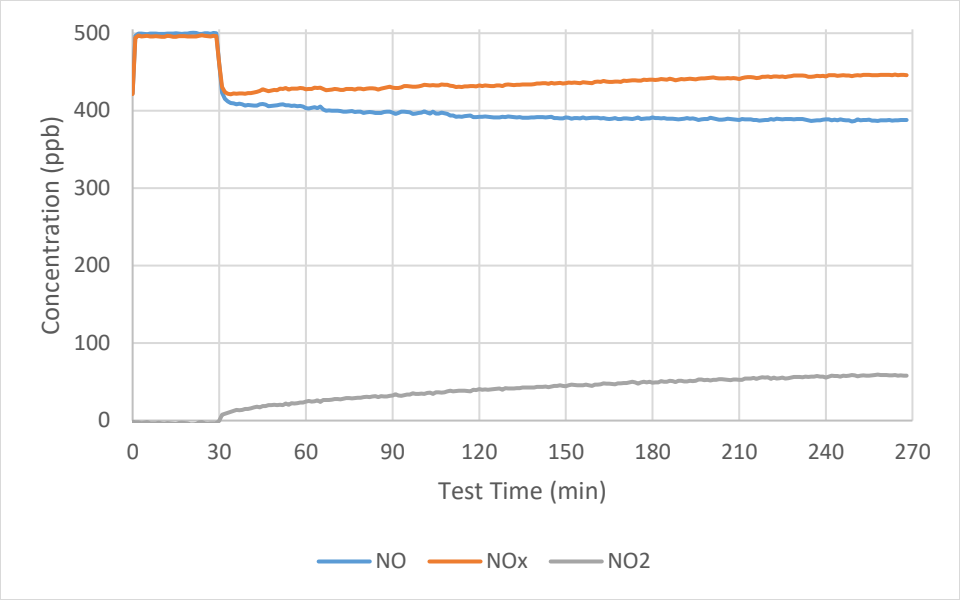

Figure A-57 Carbonated 5% Anatase, 30% Fly Ash (2/2)

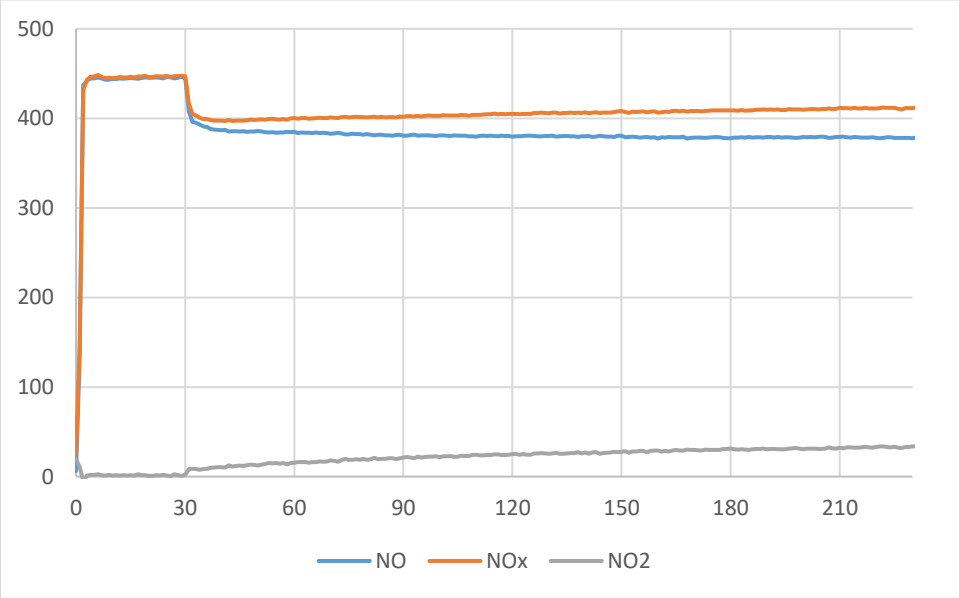

Figure A-58 Carbonated 5% Anatase, 5% Silica Fume (1/2)

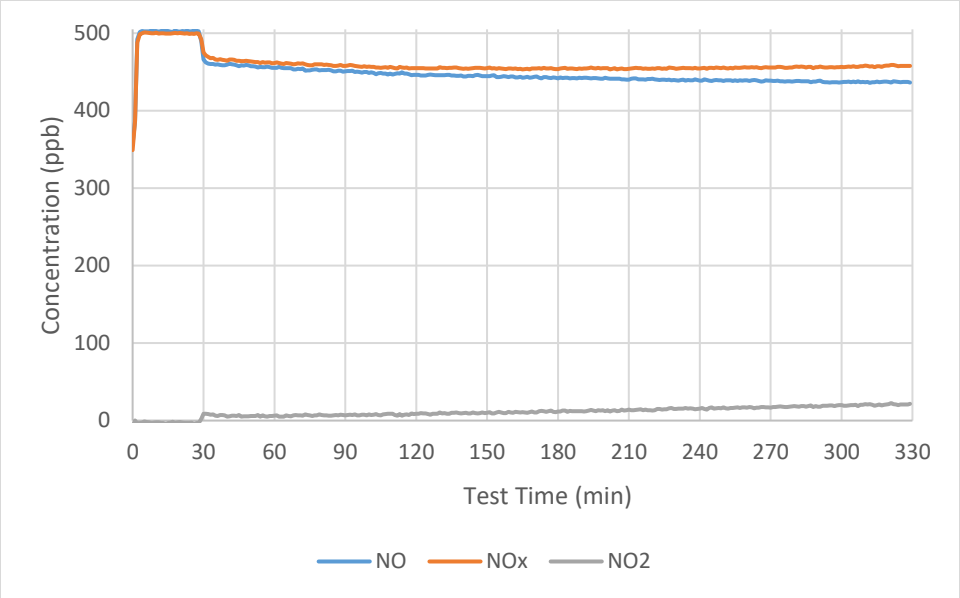

Figure A-59 Carbonated 5% Anatase, 5% Silica Fume (2/2)